Eur Phys J C **44**, s03, 1–60 (2005)
Digital Object Identifier (DOI) 10.1140/epjcd/s2005-03-006-8

EPJ C direct
electronic only

Young Scientist

Measurement of deeply virtual Compton scattering using the ZEUS detector at HERA[⋆]

I. Grabowska-Bold[1,2,a,b,c]

[1] University of Science and Technology, Kraków, Poland
[2] Deutsches Elektronen-Synchrotron, Hamburg, Germany

Received: 3 October 2005 /

For my husband, Tomasz

Abstract. The cross sections for deeply virtual Compton scattering in the reaction $ep \to e'\gamma p'$ has been measured with the ZEUS detector at HERA using integrated luminosities of $95\,\mathrm{pb}^{-1}$ of e^+p and $17\,\mathrm{pb}^{-1}$ of e^-p collisions. Cross sections are presented as a function of the exchanged photon virtality, Q^2, and the centre-of-mass energy, W, of the γ^*p system in the region $5 < Q^2 < 100\,\mathrm{GeV}^2$ and $40 < W < 140\,\mathrm{GeV}$. The obtained results are compared to QCD-based calculations.

1 Introduction

In 1923, in a study of X-ray scattering from thin targets, Arthur Compton noted that the wavelengths of the scattered X-rays were longer than that of the incident beam and the wavelength increased with scattering angle. This observation gave decisive support to the quantum theory and could be simply understood if the X-rays were considered to be particles (photons) as well as waves. This wave-particle duality is now one of the corner stones of our thinking about elementary particle physics.

At high energies photons are usually thought of as particles whose size is governed by their energies. At the HERA *ep* collider at DESY in Hamburg, the structure of the proton is probed by scattering high energy electrons (or positrons) off protons. The electrons are a source of high energy and thus short wavelength photons.

At the high centre-of-mass energies of HERA the resolution approaches 10^{-18} m or about 0.001 of the proton radius. Measurements of deep inelastic scattering have revealed a rich internal structure of the proton. In addition to the three valence quarks, the proton also contains many virtual quark-antiquark pairs. The quarks are bounded by a large number of gluons. The observed rapid increase of the gluon density as the fractional energy carried by the gluons decreases was one of the new and unexpected early results from HERA. In order to better understand the proton structure one would like to measure the correlations between pairs of gluons within the proton. This is possible by measuring the process $ep \to e'\gamma p'$, called the deeply virtual Compton scattering (DVCS) [1–6], which is a subject of this thesis.

The DVCS reaction can be regarded as the elastic scattering of the virtual photon off the proton via a colourless exchange. The perturbative QCD calculations, valid when the virtuality Q^2 of the exchanged photon is large, assume that this exchange involves two partons, having different longitudinal and transverse momenta, in a colourless configuration. These unequal momenta are a consequence of the mass difference between the incoming virtual photon and the outgoing real photon. Therefore, the DVCS cross section depends on the generalised parton distributions (GPD) [6–9], which carry information about the correlation of partons and their dynamics in the proton. The DVCS cross section at sufficiently large Q^2 is expected to rise steeply with increasing W, the centre-of-mass energy of the virtual photon-proton system, due to the fast rise of the parton densities in the proton towards smaller values of the Bjorken scaling variable x.

The DVCS final state is similar to that for diffractive processes, where a hadronic system is a vector meson. From the theoretical point of view, DVCS has a very important advantage comparing to its hadronic counterpart, because it has the photon in a final state, whose wave function is well known. DVCS is the best understood of all exclusive diffractive processes and thus can be used to test QCD predictions. Furthermore, DVCS constitutes a good probe of the transition between perturbative and non-perturbative regimes of QCD.

---

[a] *Present address*: Cern, Geneve, Switzerland,
e-mail: `Iwona.Grabowska@cern.ch`

[b] e-mail: `grabowska@fatcat.ftj.agh.edu.pl`

[c] e-mail: `Iwona.Grabowska-Bold@desy.de`

[⋆] PhD thesis awarded by the Association of the Friends and Sponsors of DESY

The final state of the DVCS process is identical to those of the purely electromagnetic Bethe-Heitler process. The interference between these two processes can provide information about the real and imaginary parts of the QCD scattering amplitude [10–12]. However, the interference term is expected to be small in the kinematic region studied in this thesis [10, 11].

The simplicity of the final state and the absence of complications due to hadronisation cause that the QCD predictions for DVCS are more reliable than for many other exclusive final states. This reaction is one of the theoretically best-understood exclusive QCD processes in *ep* collisions. The first measurements of the DVCS process at high W [13–15] and its beam-spin asymmetry in polarised *ep* scattering at low W [16–18] have recently become available.

In the thesis presented here, the analysed data were collected by the ZEUS detector at HERA during the 96–00 running periods. In 96–97, HERA collided 27.5 GeV positrons with 820 GeV protons. In 98–00, the proton energy was increased to 920 GeV and both positrons and electrons were collided.

The dependence of the DVCS cross section on W and Q^2 is studied in the kinematic range $5 < Q^2 < 100\,\text{GeV}^2$ and $40 < W < 140\,\text{GeV}$. The results are integrated over t, the square of the four-momentum transfer at the proton vertex. The e^+p cross sections are based on a ten-fold increase of statistics over the previous HERA result [14,15], permitting a better study of the W dependence of the cross section as well as a significant extension of the Q^2 range probed. This thesis also reports the first measurement of the e^-p cross sections.

More than 50 institutes from 12 countries are participating in the ZEUS Collaboration. Altogether about 500 physicists are involved in this large scale experiment. Throughout my PhD studies I took part in taking data with the ZEUS detector in the running period 2001–2002 and in monitoring of the ZEUS data quality. I was also responsible for the development of the ORANGE [19] code, which is software commonly used in present ZEUS analyses. Furthermore, throughout my PhD studies I was a member of the ZEUS Luminosity Monitor (LUMI) group. Within this group I contributed to the ZEUS experiment by performing tests of the prototype of the aerogel detector as well as implementation of the reconstruction software for the LUMI position detector.

This thesis is organised as follows. An introduction to the theory of *ep* reactions at HERA, especially concentrated on the theory of DVCS, is given in Sect. 2. Section 3 contains description of the HERA collider and the components of the ZEUS detector important for this analysis. The general reconstruction methods for various components of ZEUS, relevant for this analysis, are presented in Sect. 4. Section 5 contains the description of the online and offline selection of the DVCS process as well as the methods of reconstruction of relevant kinematic variables. Section 6 contains a description and application of the Monte Carlo programs used in this analysis. In Sect. 7 the detailed study of the background processes for DVCS is presented. Section 8 contains the description of method of extraction of the DVCS cross section as well as the study of systematics is presented. Then the DVCS results are discussed in Sect. 9 and, finally, the brief summary and conclusions are given in Sect. 10.

2 Theoretical approaches to DVCS

Deeply virtual Compton scattering (DVCS) is a diffractive *ep* interaction observed in the deep inelastic scattering regime. This process gives a possibility to extract information on the internal structure of the proton via generalised parton distributions. In the following, the theoretical basis for DVCS is described.

2.1 Lepton-proton scattering

In lepton-proton scattering, a point-like particle, the lepton[1], interacts via the electromagnetic or weak force with the proton, which has a complex substructure. Two types of processes in *ep* scattering can be distinguished: neutral current (NC) and charge current (CC) processes. In NC processes a virtual photon γ^* or a Z^0 boson is exchanged and the flavour of the incoming lepton is conserved. In CC processes the outgoing lepton is a neutrino or antineutrino as a consequence of the $W^\pm$ boson exchange.

The NC interaction can be described by the exchange of a photon transferring a four-momentum q from the lepton to the proton as shown in Fig. 1. The contribution from Z^0 and $W^\pm$ exchange is neglected in the kinematic range of this analysis. The relevant variables are the four-momenta of the incoming lepton k, of the scattered lepton k', of the initial proton P and of the hadron final state P'.

The following variables provide a relativistically invariant formulation of the inelastic *ep* event kinematics[2]:

- the centre-of-mass energy squared

$$s = (P + k)^2 \approx 4E_eE_p,$$

  where E_e and E_p are the energies of the incoming lepton and proton beam, respectively,

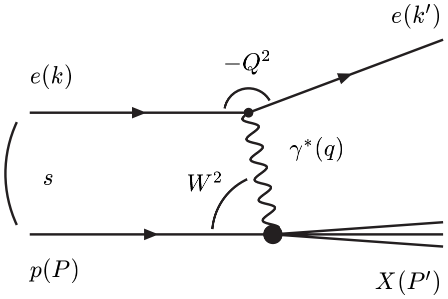

Fig. 1. Diagram of the *ep* scattering. Four-momenta of the interacting particles are given in parentheses

---

[1] In the next sections both electrons and positrons are referred to as leptons, unless explicitly stated otherwise.

[2] In this thesis the natural system of units is used, where $\hbar = c = 1$.

- the negative square of the exchanged photon four-momentum

$$Q^2 = -q^2 = -(k-k')^2,$$

which is also called *virtuality*,
- the fraction of the incoming lepton energy carried by the virtual photon in the rest frame of the initial state proton

$$y = \frac{P\cdot q}{P\cdot\ k} 0 \leq y \leq\ 1,$$

which is also known as *inelasticity*,
- the fraction of the proton momentum carried by the struck quark

$$x = \frac{Q^2}{2P\cdot q} \approx \frac{Q^2}{sy} 0 \leq x \leq\ 1,$$

- the photon-proton centre-of-mass energy squared

$$W^2 = (q+P)^2 \approx \frac{Q^2}{x}(1-x).$$

Quantities x and y are also called *Bjorken scaling variables.*

2.2 Deep inelastic scattering

When scattering leptons off protons at large transverse momenta, a substantial number of particles can be produced with high total invariant mass. This process resulting in high Q^2 is called deep inelastic scattering (DIS).

DIS is the inclusive scattering in which only a scattered lepton is detected and all other particles are recognised as the hadronic final state which is summed over. Another type of scattering is an exclusive process, in which usually all final-state particles are determined.

The kinematics of inclusive DIS events for a given centre-of-mass energy $\sqrt{s}$ is described by any two independent relativistic invariant variables defined in Sect. 2.1.

2.2.1 Cross section and structure functions

The *ep* cross section in a general formalism can be expressed as a function of the leptonic $L^{\mu\nu}$ and hadronic tensor $W_{\mu\nu}$ describing the lepton and proton vertices of the diagram in Fig. 1

$$d\sigma \propto L^{\mu\nu} W_{\mu\nu}.$$

The leptonic tensor is calculable in Quantum Electrodynamics (QED), while the hadronic one can not be calculated from first principles due to extended hadronic structure but must be parametrised in terms of functions. Symmetry properties, gauge invariance and conservation laws of QED allow to reduce the hadronic tensor for unpolarised *ep* scattering to two real functions W_1 and W_2, which are x- and Q^2-dependent. Thus, the hadronic tensor can be expressed as

$$W_{\mu\nu} = \left(-g_{\mu\nu} + \frac{q_\mu q_\nu}{q^2}\right) W_1(x,Q^2)$$

$$+ \left(P_\mu - \frac{P\cdot q}{q^2} q_\mu\right)\left(P_\nu - \frac{P\cdot q}{q^2} q_\nu\right)\frac{W_2(x,Q^2)}{m_p^2},$$

where m_p denotes the proton mass, $g_{\mu\nu}$ is the metric tensor, q and P represent the virtual photon and proton four-momenta, respectively.

The proton structure functions are related to W_1 and W_2 via

$$F_1(x,Q^2) = m_p W_1(x,Q^2) \text{and} F_2(x,Q^2) = \nu W_2(x,Q^2),$$

where $\nu = q\cdot P/m_p$ is the energy transferred from the lepton to the proton in the proton rest frame.

The cross section for unpolarised NC events can now be written as

$$\frac{d^2\sigma^{\text{NC}}}{dxdQ^2} = \frac{2\pi\alpha^2}{xQ^4}[(1+(1-y)^2)F_2(x,Q^2) - y^2 F_L(x,Q^2)],$$

where $F_L = F_2 - 2xF_1$ and α is the fine structure constant. The structure function F_3, which measures parity violating contributions resulting from Z^0 exchange, contributes only at $Q^2 \gg 10^3\,\text{GeV}^2$ and has been omitted.

The *ep* cross section can be interpreted as the product of the virtual photon flux [20]

$$\mathit{\Gamma} = \nu - \frac{Q^2}{2m_p},$$

and the total cross section $\sigma_{\text{tot}}^{\gamma^* p}$ for scattering of virtual photons on the proton

$$\sigma^{ep} = \mathit{\Gamma}\cdot\sigma_{\text{tot}}^{\gamma^* p},$$

where $\sigma_{\text{tot}}^{\gamma^* p}$ is split to the cross sections for scattering of transverse $\sigma_T^{\gamma^* p}$ and longitudinally $\sigma_L^{\gamma^* p}$ polarised photons

$$\sigma_{\text{tot}}^{\gamma^* p} = \sigma_T^{\gamma^* p} + \sigma_L^{\gamma^* p}.$$

The relations between the structure functions and the virtual photon-proton cross sections can be expressed as

$$F_2(x,Q^2) \approx \frac{Q^2}{4\pi^2\alpha}(\sigma_T^{\gamma^* p} + \sigma_L^{\gamma^* p}),$$

$$F_L(x,Q^2) \approx \frac{Q^2}{4\pi^2\alpha}\sigma_L^{\gamma^* p},$$

where the approximations are valid for small values of x. In the kinematic region of not too large y the contribution of F_L can be neglected and the cross section mainly depends on F_2.

In Fig. 2 measurements of the structure function F_2 is depicted as a function of Q^2 for different values of x. One can see that F_2 is independent on Q^2 at large range of x. This was first observed at SLAC [21, 22] for $Q^2 < 7\,\text{GeV}^2$ and $0.02 < x < 0.2$ and is known as *scaling* or *scale invariance*. In fact, at low x, a rapid increase of F_2 with Q^2 has been observed [23, 24], while F_2 decreases at large values of x. This Q^2 dependence of F_2 for fixed x is known as *scaling violation*.

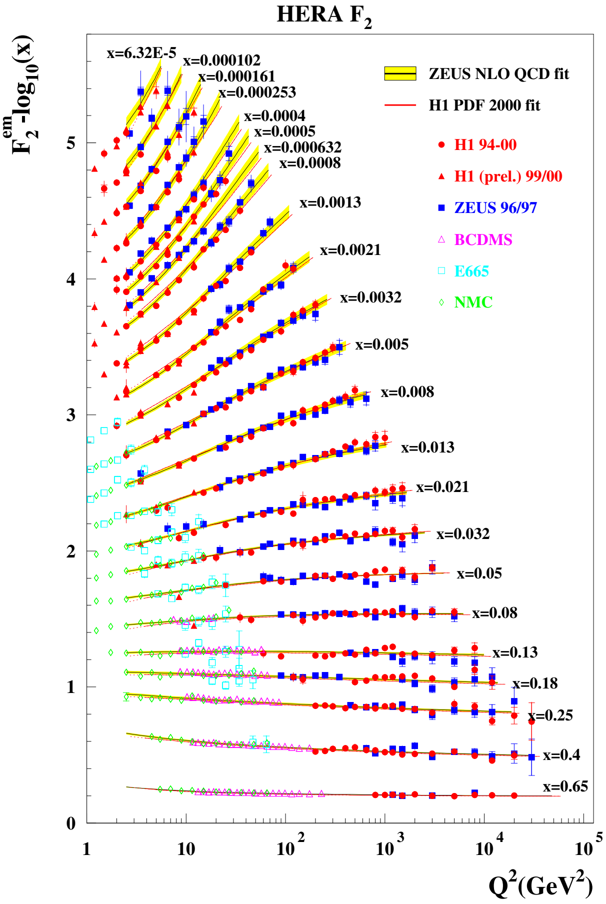

Fig. 2. The structure function F_2 as a function of Q^2 for fixed values of x. The HERA results are shown together with fixed target results and NLO QCD fit. Plot taken from [25]

The interpretation of the onset of scaling, where F_1 and F_2 can be written as functions of only one variable, $F_i(x, Q^2) = F_i(x)$, is that the virtual photon no longer scatters off the whole target proton but only off a part of the proton being a consequence of its partonic structure [26,27]. The discovery of a substructure of the proton led to the formulation of the Quark Parton Model (QPM), in which the proton consists of three point-like partons which can be identified with the quarks introduced by Gell-Mann and Zweig [28, 29] to explain the spectroscopic hadron data.

The Q^2-independent structure functions F_1 and F_2 can be related to the parton density functions f_i inside the proton via

$$F_1(x) = \frac{1}{2}\sum_i e_i^2 f_i(x),$$

$$F_2(x) = x\sum_i e_i^2 f_i(x),$$

where the sums are over the parton flavour i weighted by the corresponding parton charge squared e_i^2. The parton density functions are interpreted in the QPM as the probability to find a parton of type i with the momentum fraction x in the proton.

Experimentally it was found that only half of the proton momentum is carried by charged quarks [30]. The other half is carried by neutral partons which are identified with gluons, the mediators of the strong interactions. This effect was understood in the framework of Quantum Chromodynamics (QCD).

2.2.2 Quantum Chromodynamics

QCD is the quantum field theory developed in the 1970's to describe the strong interactions between quarks. It assumes that the proton is built up from quarks which are spin 1/2 fermions. They are bounded together by gluons which are the spin 1 gauge bosons mediating the strong forces. QCD is a non-abelian gauge theory based on the SU(3) symmetry group. Quarks carry one of three possible colour charges (red, green or blue). Gluons also carry colour charge and thus couple to each other.

In contrast to QED, the QCD coupling constant α_s increases at large distances (low Q^2) and decreases at small distances (large Q^2). This is known as *asymptotic freedom*. In leading logarithm approximation, α_s is expressed as

$$\alpha_s(Q^2) = \frac{12\pi}{(33 - 2n_f)\ln(Q^2/\Lambda^2_{\mathrm{QCD}})},$$

where n_f is the number of active quark flavours for which $m_q^2 < Q^2$. The Λ^2_{QCD} quantity is the QCD scale parameter which has to be determined by experiment. It determines the energy at which α_s decreases logarithmically and where $\Lambda^2_{\mathrm{QCD}} \ll Q^2$ perturbative QCD (pQCD) can be applied.

2.2.3 Parton distribution functions

The factorisation theorem states that short range effects in the scattering amplitude, calculable in pQCD, can be separated from the non-perturbative long range effects which are expressed by the parton distribution functions (PDF). The factorisation theorem was proven for hard scattering [31]. It defines the inclusive structure function as

$$F_2(x, Q^2) = \sum_{i=q,\bar{q},g} \int_x^1 dx' C_i\left(\frac{x}{x'}, \alpha_s(\mu_F^2), \frac{Q^2}{\mu_F^2}\right) f_i(x', \mu_F^2),$$

where C_i denotes the coefficient functions responsible for short range interactions and f_i are PDF which have to be determined experimentally. They are specific to the type of hadron. Quantity μ_F^2 is the factorisation scale which determines the separation line between what is considered as the long range inner dynamics of the proton (f_i) and the dynamics of the hard lepton-parton interaction (C_i). The idea of factorisation for the $ep \to e'X$ process is schematically shown in Fig. 3.

2.3 Diffractive processes

Diffractive interactions [32, 33] were first observed in hadron-hadron elastic scattering, $A + B \to A + B$. Later

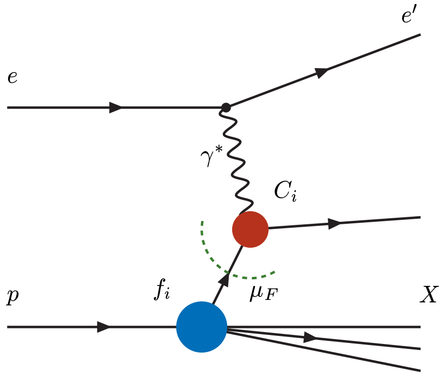

Fig. 3. Schematic representation of the factorisation theorem. Symbols are explained in the text

they were generalised to processes where one ($A + B \rightarrow X + B$ single dissociation) or both ($A + B \rightarrow X + N$ double dissociation) colliding hadrons were transformed to multi-particle final states without exchange of quantum numbers between the scattered hadrons. It implies that no colour charge is exchanged, thus there is no colour field operating between the two outgoing systems X and N.

Diffractive events are recognised by the final-state hadron detected at large values of rapidity[3] and a gap in rapidity between the final states A and B was observed [34], where in more general case the states A and B correspond to X and N. The rapidity gap is the consequence of a small exchange of transverse momentum, so the final-state particles move with momenta close to those of the initial ones. It was also observed that the basic features of diffractive processes seem to be independent of the type of the incoming hadron.

So far there is a lack of one model describing correctly all aspects of the diffractive process. This type of reactions belongs mostly to the soft physics, mainly described by the phenomenological models only. Soft processes take place at low energies and are meant as interactions characterised by low transverse momenta, while at high energies hard interactions are observed. One of the soft models, widely used to compare its predictions with measurements in diffractive physics, is the Regge phenomenology [35].

In the Regge theory, the elastic hadron-hadron scattering is described by exchange of one or more Reggeons. The Reggeon is equivalent to a superposition of particles (mesons or baryons) with the same quantum numbers except for spin. For the particle spin plotted as a function of the mass squared, the particles corresponding to a specific Reggeon lie on a Regge trajectory which can be approximated by the straight line [36]. This theory succeeded in predictions for the elastic cross section, which was found to fall initially with increasing centre-of-mass energy, but then levels off and show a slight rise. The initial fall can be described by the Reggeon trajectory, while the rise can be fitted to a new Pomeron trajectory ($\mathbb{P}$) [37]. The growth of the cross section was first predicted by Pomeranchuk [38] and the trajectory was named after him. The $\mathbb{P}$ has the quantum numbers of the vacuum and is generally thought as the mediator in the diffractive scattering.

In the QCD based models for the $\mathbb{P}$ exchange, diffractive process is described by a quark-antiquark or two-gluon exchange.

2.3.1 Diffraction in DIS

At HERA, diffractive events have been observed in photoproduction [39] as well as in electroproduction [34, 40] regimes. Photoproduction refers to processes where the lepton is scattered at a small angle, emitting a quasi-real photon with $Q^2 \approx 0$, which then interacts with the proton, while electroproduction denotes processes with a virtual-photon exchange with $Q^2 \gg 0$.

Diffractive processes in DIS at HERA are generally of the form

$$e(k) + p(P) \rightarrow e'(k') + N(P_N) + X(P_X),$$

where X denotes the final state originating from the dissociated photon and N is the final state of the proton. The general diagram of a diffractive ep process is shown in Fig. 4.

For a complete description of diffractive events further kinematic variables, in addition to the usual DIS variables defined in Sect. 2.1, are introduced:

- the square of the four-momentum transfer at the proton vertex
$$t = (P - P_N)^2,$$
- mass of the hadronic system X produced by the photon dissociation M_X,
- the fraction of the proton momentum carried by the $\mathbb{P}$
$$x_{\mathrm{IP}} = \frac{(P - P') \cdot q}{P \cdot q} \approx \frac{M_X^2 + Q^2}{W^2 + Q^2},$$
- the fraction of the struck quark momentum carried by the $\mathbb{P}$
$$\beta = \frac{Q^2}{2(P - P') \cdot q} = \frac{x}{x_{\mathrm{IP}}} \approx \frac{Q^2}{M_X^2 + Q^2}.$$

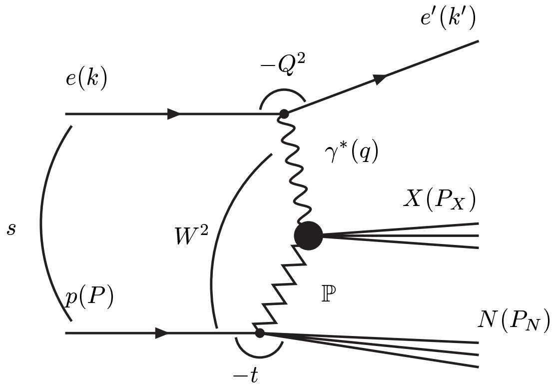

Fig. 4. Diagram of the diffractive ep process. Four-momenta are given in parentheses

---

[3] The rapidity of a particle with energy E and longitudinal momentum $p_{||}$ is defined as $y = \frac{1}{2}\ln\frac{E+p_{||}}{E-p_{||}}$, which can be approximated by the pseudorapidity $\eta = -\ln(\tan\frac{\theta}{2})$ in the limit where the particle mass is small and $\cos\theta = p_{||}/E$.

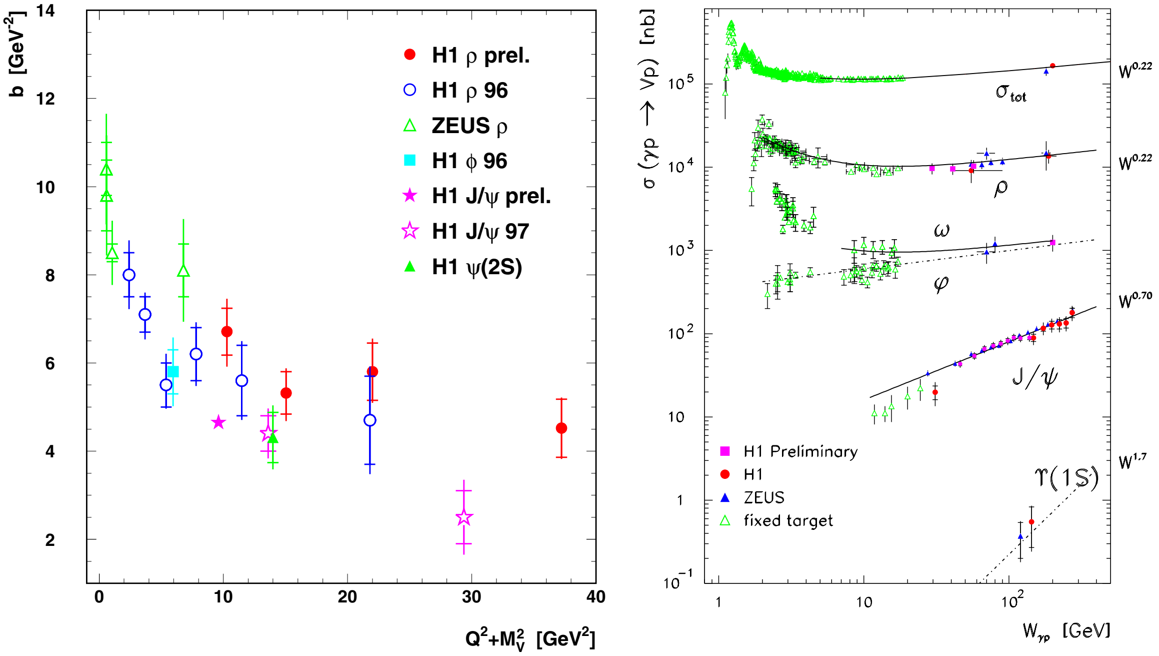

Fig. 5. (Left) The b slope dependence on Q^2 for the $\gamma^*p \to Vp$ process, where $V = \rho, \phi, J/\psi, \psi(2S)$. (Right) The elastic vector-meson cross sections as a function of W measured in photoproduction at HERA compared to the measurements at low energy and to the total cross section. The lines illustrate a comparison of various power-law energy dependence at high energy. Plots taken from [25]

2.3.2 Properties of diffractive processes

The basic features of diffractive processes can be summarised as follows:

- The differential cross section, $d\sigma/dt$, displays a sharp exponential fall
$$\frac{d\sigma}{dt} \propto e^{-b|t|},$$
with the slope parameter, $b = R^2/4$, where R is the transverse radius of the interaction. It typically increases slowly with energy $\sqrt{s}$ which is known as *shrinkage of the forward diffractive peak*. The b slope for $\gamma^*p \to Vp$ is observed to fall with Q^2 for light vector mesons and it is constant for heavier ones (see Fig. 5).
- The diffractive cross section is characterised by a weak dependence on the energy $\sqrt{s}$ given by
$$\sigma^{\text{tot}} \propto s^{\epsilon},$$
where $\epsilon = 0.08$ was found experimentally [41].
- For single dissociation $AB \to XB$, the small masses M_X of the system X are preferred and the cross section behaves like
$$\frac{d\sigma^{\text{AB}\to\text{XB}}}{dM_X^2} \propto \frac{1}{(M_X)^n},$$
where $n \approx 2$ [33].
- The W dependence of the $\gamma^*p \to Vp$ cross section is expected to have a form
$$\sigma \propto W^{\delta},$$
where the exponent δ grows from 0.2 for soft interactions towards higher values for hard processes.

Figure 5 shows the vector-meson elastic cross sections $\gamma p \to Vp$ with $V = \rho, \omega, \phi, J/\psi, \Upsilon(1S)$ as functions of W for the photoproduction regime. The $\sigma \propto W^{\delta}$ fit is imposed on the data. The rise of the cross section for the production of light vector mesons (ρ, ω, ϕ) can be described in the framework of the Regge theory by the exchange of the $\mathbb{P}$ trajectory known for soft diffractive interactions. In the case of J/ψ and Υ photoproduction the rise of the cross section is steeper than predicted by the Regge formalism. For light vector mesons this steeper rise can be achieved at higher Q^2 values. This can be seen in Fig. 6, where the $\gamma^*p \to \rho p$ cross section as a function of W is shown for several Q^2 values together with the W^{δ} fits. For large Q^2 values, δ is significantly larger than for the lower ones. This region denotes hard diffractive interactions for which pQCD is applicable.

2.4 Generalised parton distributions

Generalised parton distributions (GPD) [3, 9, 43–47], also called skewed parton distributions or off(non)-diagonal parton distributions, parametrise the complex structure of the proton (or more generally nucleon) independently on the reaction which probes the target.

The GPD contain information on the correlations between quarks, which is contained in the non-diagonal matrix elements, and on their momentum dependence. Moreover, they enable access to the quark spin and the quark orbital momentum of the proton spin unreachable elsewhere [7]. The traditional inclusive PDF extracted from DIS allow to access only parton densities, i.e. the diagonal matrix elements.

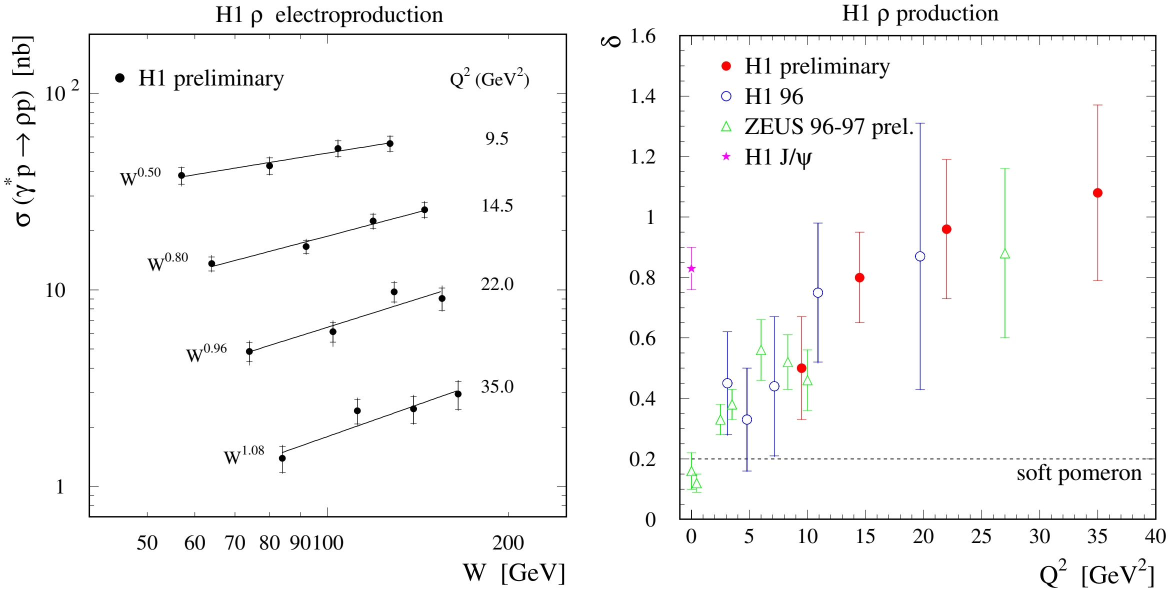

Fig. 6. (Left) The $\gamma^* p \to \rho p$ cross section as a function of W for several Q^2 values. The imposed lines represent parameterisations of the form $\sigma \propto W^\delta$. (Right) Results of fits of the form $\sigma \propto W^\delta$ to the W dependence of the $\gamma^* p$ cross section, presented as a function of Q^2 for ρ and J/ψ vector mesons. Plots taken from [42]

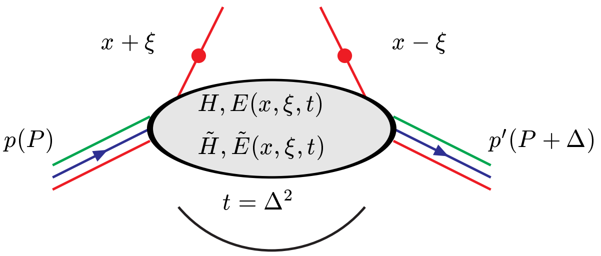

Fig. 7. Schematic diagram for the GPD

If the leading order pQCD amplitude for the certain process in the forward direction ($t = 0$ and equal helicities of the initial and final proton) can be factorised in a hard scattering part exactly calculable in pQCD and a non-perturbative proton structure part, the structure of the proton can be parametrised in terms of four GPD (see Fig. 7). They are traditionally denoted $H, \tilde{H}, E$ and $\tilde{E}$, and depend on three variables x, ξ and t, where ξ is called *skewedness*. The quantity $x + \xi$ denotes the longitudinal momentum fraction carried by the initial quark struck by the virtual photon and similarly $x - \xi$ relates to the final quark going back to the proton. Therefore, -2ξ is the longitudinal momentum difference between the final and initial quarks.

The standard PDF are defined on the cross-section level whereas the GPD are defined on the amplitude level, i.e. when calculating cross sections, the GPD enter calculations of the scattering amplitude which further is squared to obtain the cross-section expression.

The GPD for quarks[4] of flavour q can be defined by Fourier transforms of the hadronic matrix elements as

$$\int \frac{d\lambda}{2\pi} e^{i\lambda x} \langle p' | \bar{\psi}_q(-\lambda/2) \gamma^\mu \psi_q(\lambda/2) | p \rangle$$

$$= H_q \bar{u}(P') \gamma^\mu u(P) + E_q \bar{u}(P') \frac{i\sigma^{\mu\nu} \Delta_\nu}{2m_p} u(P)$$

and

$$\int \frac{d\lambda}{2\pi} e^{i\lambda x} \langle p' | \bar{\psi}_q(-\lambda/2) \gamma^\mu \gamma_5 \psi_q(\lambda/2) | p \rangle$$

$$= \tilde{H}_q \bar{u}(P') \gamma^\mu \gamma_5 u(P) + \tilde{E}_q \bar{u}(P') \frac{\Delta^\mu \gamma_5}{2m_p} u(P),$$

where $|p\rangle$ and $\langle p'|$ represent the quantum numbers of the incoming and outgoing proton, respectively, including differences for the spin state. Quantities $\bar{\psi}_q(-\lambda/2)\gamma^\mu\psi_q(\lambda/2)$ and $\bar{\psi}_q(-\lambda/2)\gamma^\mu\gamma_5\psi_q(\lambda/2)$ are operators which select the quark with certain properties from the hadronic wave functions. $\bar{u}$ and u represent the Dirac spinors of the proton and $\Delta^\mu = P'^\mu - P^\mu$.

H and E are spin-independent and are also called the unpolarised GPD, whereas $\tilde{H}$ and $\tilde{E}$ are spin-dependent and are usually called the polarised GPD. Actually H and $\tilde{H}$ are a generalisation of the PDF measured in DIS, which in the forward direction reduce to the quark distributions (H) and to the quark helicity distributions ($\tilde{H}$). Furthermore, there are formulae which relate the first moment of the GPD to the elastic proton form factors.

2.5 Deeply virtual Compton scattering

The deeply virtual Compton scattering (DVCS) is a diffractive electroproduction of a real photon in DIS. For the *ep* collisions this process can be written as

$$e(k) + p(P) \to e'(k') + \gamma + p'(P'), \tag{1}$$

with diagram depicted in Fig. 8a. In this process the proton

---

[4] Analogous definition can be given for gluons.

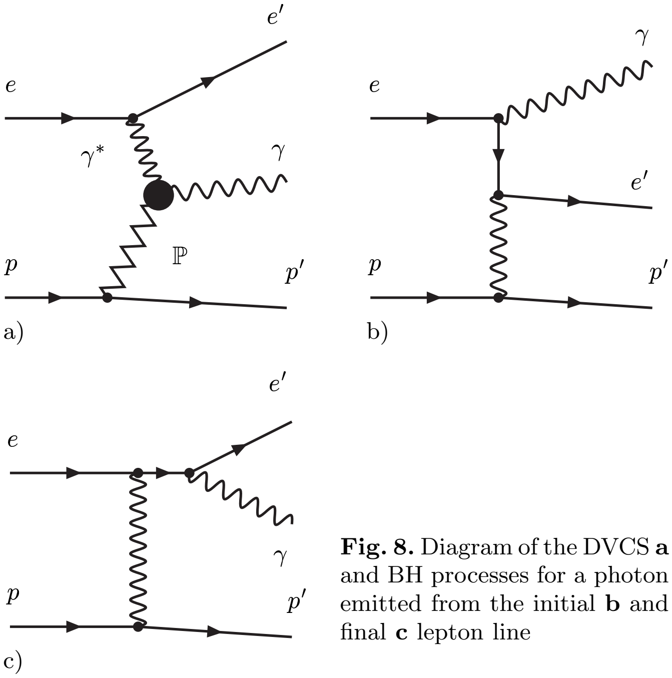

Fig. 8. Diagram of the DVCS **a** and BH processes for a photon emitted from the initial **b** and final **c** lepton line

can either remain intact (elastic case), be excited into a resonant state (quasi-elastic) or be broken up (inelastic).

The DVCS diagram is similar to that for diffractive processes (see Fig. 4), where a hadronic system is a vector meson. In the theory point of view, DVCS has a very important feature comparing to its hadronic counterpart, because of the photon in a final state, whose wave function is known. In the vector-meson case, assumptions about vector-meson wave functions are necessary, increasing the theoretical uncertainty. A further advantage of studying the DVCS process comes from the fact that the cross section goes as $1/Q^6$ compared to $1/Q^8$ in the vector-meson case [47]. The DVCS process appears to be the least suppressed in Q^2 of all known exclusive hard diffractive processes.

It has been shown [3,5,43,44] that for high Q^2 the DVCS amplitude factorises to a hard scattering coefficient, which is calculable in pQCD, and a soft part which is involved in the GPD. The leading (LO) and next-to-leading (NLO) order diagrams of the DVCS process in QCD are shown in Figs. 9a and b, respectively. In the LO process, γ^* scatters off the quark originating from the proton, while in the NLO diagram γ^* interacts via a quark loop with two gluons from the proton. In both cases the real photon is emitted from the quark loop.

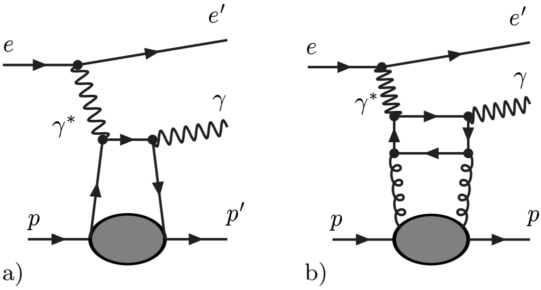

Fig. 9. The QCD diagrams of the DVCS process in LO **a** and NLO **b** in QCD

The LO diagram also helps to understand the concept of GPD. In order to bring the outgoing photon onto its mass shell, the fraction of the proton momentum carried by the quark initially and finally can not be the same. By studying DVCS, one investigates what happens when one removes a quark from the proton of one given momentum, and replaces it with a quark of another momentum. Thus one probes two-particle correlations in the proton.

The DVCS final state is identical to those of the Bethe-Heitler (BH) process (see Figs. 8b and c), so the two processes interfere.

The final-state amplitude $\mathcal{A}$ is the sum of amplitudes for DVCS ($\mathcal{A}_{\mathrm{DVCS}}$) and BH ($\mathcal{A}_{\mathrm{BH}}$), so

$$|\mathcal{A}|^2 = |\mathcal{A}_{\mathrm{DVCS}}|^2 + |\mathcal{A}_{\mathrm{BH}}|^2 + \mathcal{I}, \tag{2}$$

with the interference term

$$\mathcal{I} = \mathcal{A}_{\mathrm{DVCS}}\mathcal{A}^*_{\mathrm{BH}} + \mathcal{A}^*_{\mathrm{DVCS}}\mathcal{A}_{\mathrm{BH}}, \tag{3}$$

where the latter can also be written as

$$\mathcal{I} = 2(\Re\mathrm{e}\,\mathcal{A}_{\mathrm{DVCS}}\,\Re\mathrm{e}\,\mathcal{A}_{\mathrm{BH}} + \Im\mathrm{m}\,\mathcal{A}_{\mathrm{DVCS}}\,\Im\mathrm{m}\,\mathcal{A}_{\mathrm{BH}}).$$

If one defines an azimuthal angle ϕ as the angle between the lepton and hadron scattering planes in the centre-of-mass of the virtual photon-proton system shown in Fig. 10, the azimuthal angular dependences of the terms in (2) and in (3) arise from the contraction of the leptonic and hadronic tensors [11]. The DVCS amplitude for a given helicity λ of the intermediate photon γ^* depends on ϕ as

$$\mathcal{A}_{\mathrm{DVCS}} \propto \exp\,(-i\lambda\phi),$$

while the BH amplitude has generally a complicated ϕ dependence, which in LO of $1/Q^2$ simplifies to

$$\mathcal{A}_{\mathrm{BH}} \propto \exp\,(-2i\lambda'\phi) + \mathcal{O}(\frac{1}{Q^2})$$

for a scattered photon of helicity λ'.

It was shown [48] that these different spin dependences of $\mathcal{A}_{\mathrm{DVCS}}$ and $\mathcal{A}_{\mathrm{BH}}$ lead to a non-vanishing ϕ dependence of $\mathcal{I}$, which in LO for unpolarised *ep* scattering yields a contribution to the cross section proportional to $\cos\phi$. This has a consequence in non-zero azimuthal-angle asymmetry [6,10,47] and beam-charge asymmetry [11], which can be investigated looking for a proton and electron or positron in the same and opposite hemispheres of a detector. Both the asymmetries are defined in a way to be directly related to the interference term. Thus, measuring them, one

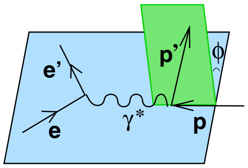

Fig. 10. The lepton and hadron scattering planes

gets access to $\Re e(\mathcal{A}_{\mathrm{DVCS}})$. Moreover, for polarised ep scattering different ϕ dependence appears for different beam polarisations, so the beam-spin asymmetry [11], which is proportional to $\Im m(\mathcal{A}_{\mathrm{DVCS}})$, can be investigated. The measurements of different contributions to the cross section yield a possibility to extract the GPD.

In the kinematic region investigated here, the azimuthal-angle asymmetry, thus also the interference term, is predicted to be fairly sizeable [10,47] already for small t. Moreover, this asymmetry strongly depends on the energy. Nevertheless, in this analysis the interference term is assumed to be zero due to integration over all ϕ angles. Therefore, the BH contribution to the cross section for the process (1) can be subtracted and the DVCS cross section can be measured.

The apparent simplicity of the DVCS process makes it a new and powerful tool to study the following aspects of QCD in the field of diffraction:

- the $\gamma^* p \to \gamma p$ cross section can be measured,
- the interference of DVCS with BH allows the measurement of the real part of the QCD amplitude,
- the DVCS process can provide an indirect measurement of GPD,
- the DVCS cross section is proportional to the square of the inclusive proton structure function F_2, and therefore provides additional information on F_2 at low x.

2.5.1 GPD-based models

The first calculation of the DVCS cross section for the HERA kinematic region was given by Frankfurt, Freund and Strikman [6] (FFS model). In this model, the DVCS ep and $\gamma^* p$ cross sections and the interference term are related to the inclusive structure function F_2 as

$$\begin{aligned}
\frac{d^3\sigma^{ep}_{\mathrm{DVCS}}}{dx dQ^2 dt} &= \frac{\pi^2\alpha^3}{2xR^2Q^6}\left[1+(1-y)^2\right] e^{-b|t|} F_2^2(x,Q^2) \\
&\quad \times (1+\rho^2), \\
\sigma^{\gamma^* p}_{\mathrm{DVCS}}(W,Q^2) &= \frac{\pi^3\alpha^2}{bR^2Q^4} F_2^2(x,Q^2)(1+\rho^2), \qquad (4) \\
\frac{d^4\sigma^{ep}_{\mathrm{INT}}}{dx dQ^2 dt d\phi} &= \frac{\pm\rho\alpha^3 y[1+(1-y)^2]}{2RxQ^5\sqrt{|t|(1-y)}} e^{-b|t|/2} \\
&\quad \times F_2(x,Q^2)\frac{G_E(t)+\frac{|t|}{4m_p^2}G_M(t)}{1+\frac{|t|}{4m_p^2}}\cos\phi,
\end{aligned}$$

where $x \simeq Q^2/(Q^2+W^2)$ is the Bjorken scaling variable, ϕ is the angle between the lepton and proton scattering planes (see Fig. 10) calculated in the virtual photon-proton centre-of-mass system, b is the exponential slope of the t dependence, y is the inelasticity and $G_E(t)$ and $G_M(t)$ are the electric and magnetic proton form factors, respectively. The "+" sign in the interference term corresponds to an electron and the "−" sign corresponds to the positron. The ratio $R = \Im m\, \mathcal{A}_{\mathrm{DIS}}(\gamma^* p \to \gamma^* p)|_{t=0} q / \Im m\, \mathcal{A}_{\mathrm{DVCS}}(\gamma^* p \to \gamma p)|_{t=0}$ accounts for the non-forward character of the DVCS process and is directly related to a ratio of the GPD to PDF [49] and $\rho = \Re e\, \mathcal{A}_{\mathrm{DVCS}}(\gamma^* p \to \gamma p)|_{t=0} / \Im m\, \mathcal{A}_{\mathrm{DVCS}}(\gamma^* p \to \gamma p)|_{t=0}$. The value of R, calculated in the leading order QCD evolution of the GPD, is about 0.55, with a little dependence on x or Q^2 [6]. The value of b is expected to depend on both W and Q^2. At high Q^2 and very small x, b is expected to increase with W [6].

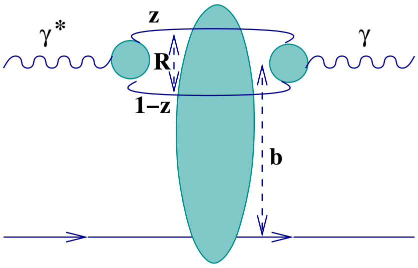

Fig. 11. The schematic representation of the colour-dipole model of DVCS

In a more formal approach [5], it has been proven that in the limit $Q^2 \to \infty$, the DVCS amplitude factorises into a hard scattering coefficient, calculable in pQCD and a soft part which can be included to the GPD. The kernels of the evolution equations for the GPD are known to next-to-leading order [50,51] and thus the GPD can be evaluated at all Q^2, given an input at some starting scale Q_0^2. At present, measurements of the DVCS cross section are essential in modelling the input GPD [49–51].

2.5.2 Colour-dipole models

The DVCS cross section can also be calculated within the colour-dipole models (CDM) [52–55], which have been successful in describing both the inclusive and the diffractive DIS cross sections at high energy [56–61].

In the proton rest frame, the DVCS process can be seen as a succession in time of three factorisable subprocesses. First, the incoming virtual photon fluctuates into a quark-antiquark pair (colour dipole) long before the interaction with the proton, then this colour dipole interacts with the proton target and finally the quark pair annihilates to a real photon in time much longer than the interaction time with the target, as schematically shown in Fig. 11.

In this approach the amplitude of the DVCS process can be written as

$$\mathcal{A}_{\mathrm{DVCS}} = \int_{R,z} \psi^{\mathrm{in}}_{\gamma^*} \sigma_d \psi^{\mathrm{out}}_{\gamma},$$

where $\psi^{\mathrm{in}}_{\gamma^*}$ and $\psi^{\mathrm{out}}_{\gamma}$ are the incoming virtual photon and the outgoing real photon wave functions, respectively, which are well known from QED. The cross section σ_d describes interaction of the dipole with the proton and is substantially affected by a non-perturbative content. The integral goes over all transverse dipole sizes R and all longitudinal momentum fractions z of the quark in the dipole. σ_d is usually assumed to be flavour- and z-independent. The parameters of a model are obtained from an adjustment to data.

A lot of realisations of the dipole approach to DVCS exist, which differ in the formulation of the dipole cross section. In particular, the model developed by Donnachie and Dosch [61] is based on the concept of soft and hard Pomeron exchange. In this approach small dipoles interact predominantly by the exchange of the hard $\mathbb{P}$ component while large dipoles interact via the soft $\mathbb{P}$ component. The model by Forshaw, Kerley and Shaw [58, 62, 63] uses the Regge phenomenology. It assumes that σ_d depends only on the properties of the dipole-proton system described by W and R, and does not depend on Q^2. The model by McDermott, Frankfurt, Guzey and Strikman [60, 63] incorporates the QCD colour transparency phenomena and assumes that σ_d depends on W, R and Q^2. The recent approach by Favart and Machado [64, 65] implements the dipole cross section from the saturation model [56, 57], which interpolates successfully between soft and hard regimes.

3 The ZEUS detector at HERA

In this section an overview of the HERA collider and the ZEUS experiment is presented. The components of the ZEUS detector significant for this analysis are then briefly described.

3.1 The HERA collider

The HERA (Hadron Elektron Ring Anlage) [66], the first lepton-proton storage ring in the world, is located at the Deutsches Elektronen Synchrotron (DESY) laboratory in Hamburg in Germany (see Fig. 12). The proposal for the *ep* collider was approved in April 1984. The first *ep* collisions were achieved in October 1991, and the ZEUS experiment took first physics runs in spring 1992. Since then physics data have been continuously collected at HERA. In 2000 the HERA upgrade to increase the luminosity was started.

Fig. 12. Aerial view of DESY and the surrounding area in Hamburg. The location of the accelerators PETRA and HERA are indicated by dashed lines

HERA was designed to collide electrons or positrons, accelerated up to the energy of 30 GeV but operates at 27.5 GeV, with protons with energies 820 (920) GeV, depending on the running year, yielding a centre-of-mass energy an order of magnitude higher than fixed target experiments. This opens a new kinematic region for measurements. In the overlapping region comparisons between HERA and fixed target experiments can be done.

The HERA tunnel is 6.3 km long and it is placed 15–25 m under ground level. It consists of four straight segments, each 360 m long, joined by four arcs with a radius of 779 m. Leptons and protons are accelerated in two different pipes, equipped with conventional and superconducting magnets, respectively. The two beams consist of bunches of particles circulating in the rings in the opposite directions.

Four experiments are located in the experimental halls at HERA. In the two of them, H1 (north hall) and ZEUS (south hall), the beams are collided at zero crossing angle. Two fixed-target experiments, HERMES (east hall) and HERA-B (west hall), make only use of the lepton and proton beams, respectively. H1 and ZEUS are devoted to measurements of the $e^{\pm}p$ interactions. HERMES studies the spin structure of the nucleon by scattering longitudinally polarised leptons off polarised gas targets such as hydrogen, deuterium or helium, while the HERA-B experiment is devoted to explore $\mathcal{CP}$-violation.

Figure 13 depicts a schematic layout of the HERA collider and its pre-accelerator system.
The proton acceleration chain starts with negative hydrogen ions (H^-), which are accelerated to 50 MeV in LINAC. Before injection into the DESY III synchrotron ring, electrons are stripped of the H^--ions, yielding protons. After subsequent acceleration to 7.5 GeV and 40 GeV in DESY III and PETRA II, respectively, protons are injected into the HERA storage ring, where they are accelerated up to their final energy of 820 (920) GeV depending on the running year. The procedure is repeated until HERA is filled with 210 proton bunches. The proton-beam life time is of the order of several days.

The lepton pre-acceleration chain starts in LINAC II, where the lepton beam is accelerated up to 450 MeV. The lepton intensity accumulator is then filled with a single bunch of leptons of about 60 mA. This bunch is transferred to DESY II achieving energies of 7.5 GeV and further into PETRA II until 70 bunches are accumulated, reaching energy of 14 GeV. They are transferred into the HERA lepton pipe until 210 bunches are filled and further accelerated to their final energies of 27.5 GeV. The positron-beam life time for its final energy is about eight hours. In case of electrons, the life time for currents of about 20 mA is reduced to about four hours. The life-time problem is attributed to capturing by positively charged dust, which originates from ion getter pumps of the HERA lepton vacuum system.

Leptons and protons are grouped in bunches of about 10^{10} particles each. In total 210 bunches of each leptons and protons spaced by 96 ns can be filled into HERA. The main bunches are followed by so called "*satellite bunches*" which are distanced by about 8 ns and 4.5 ns for the lepton and proton beams, respectively, with respect to primary

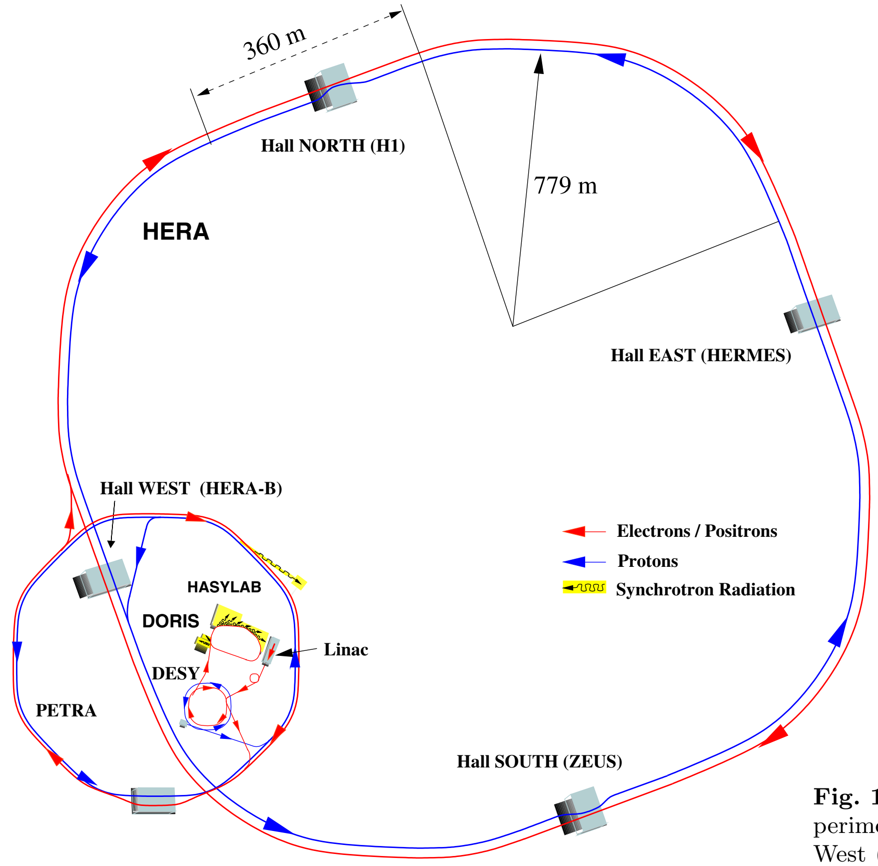

Fig. 13. The HERA accelerator complex. Four experiments are located in the halls South (ZEUS), West (HERA-B), North (H1) and East (HERMES)

bunch crossing time. During normal running, some of the 210 bunches are left empty (so called "*pilot bunches*") in order to study the background conditions. Non-colliding bunches (when either the lepton or proton bunch is empty) enable the measurement of beam-gas related background, while empty "pilot bunches" (when neither of the two is filled) allow the study of cosmic-ray background rates.

Between the years 1992 and 2000 several changes at HERA have been performed, i.e. increase of the proton-beam energy and exchange of particle in the lepton beam. In the first case the centre-of-mass energy has been increased yielding a rise of the kinematic region. In the second case, one can profit from the different physics results only present in e^-p or e^+p collisions, yielding a possibility of comparing the two data sets. In 1993 the electron energy was increased from 26.7 GeV to 27.5 GeV. In 1994 due to the shorter life time of the electron beam, electrons were substituted by positrons. In the 1997–1998 winter shutdown the proton energy was increased from 820 GeV to 920 GeV with the consequent change of the centre-of-mass energy from $\sqrt{s} = 300$ GeV to $\sqrt{s} = 318$ GeV. In the same period new ion getter pumps were installed, what gave a possibility to run with electrons again.

Figure 14 shows the luminosity delivered by HERA during the 1992–2000 running periods versus days of running. For purposes of this thesis the 1996–2000 data were used. This covers most of the HERA luminosity. A summary for the data taking periods used in this study can be found in Table 1.

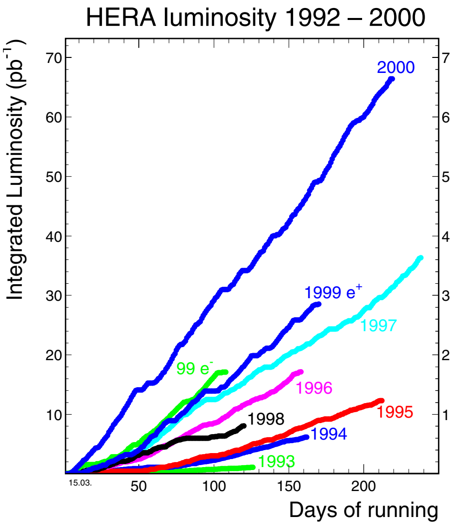

Fig. 14. Integrated luminosity delivered by HERA during the 1992–2000 data periods

3.2 The ZEUS detector

3.2.1 Overview

ZEUS is a nearly hermetic multipurpose detector designed to explore photoproduction and deep inelastic NC and CC processes which occur in the *ep* scattering. The design takes

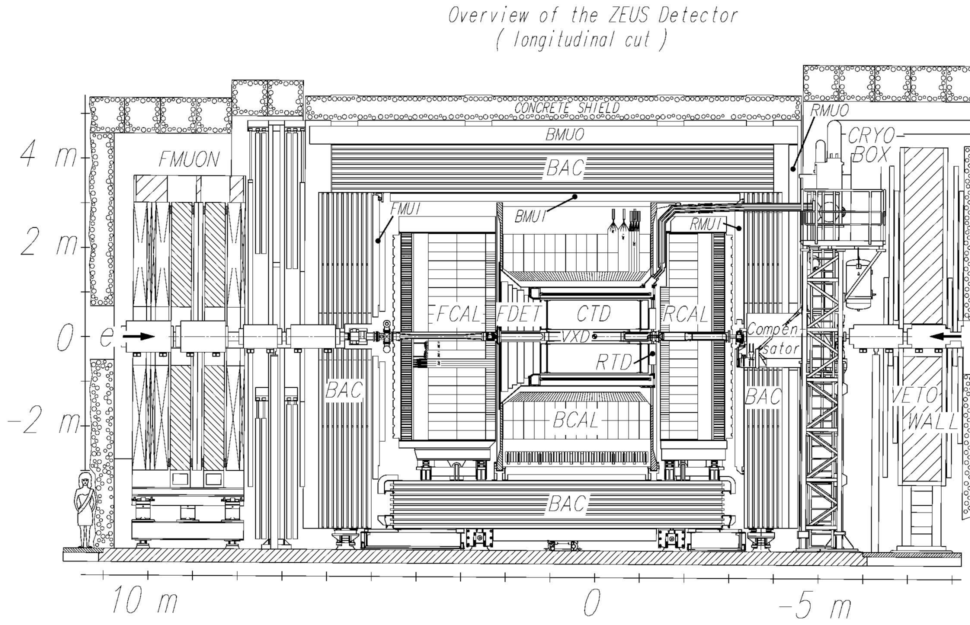

Fig. 15. Longitudinal cut of the ZEUS detector

Table 1. Overview of the luminosity delivered by HERA from 1996 to 2000

Lepton beam	Year	HERA luminosity (pb^{-1})	Proton beam (GeV)
e^+	96–97	53.5	820
e^-	98–99	25.2	920
e^+	99–00	94.95	920

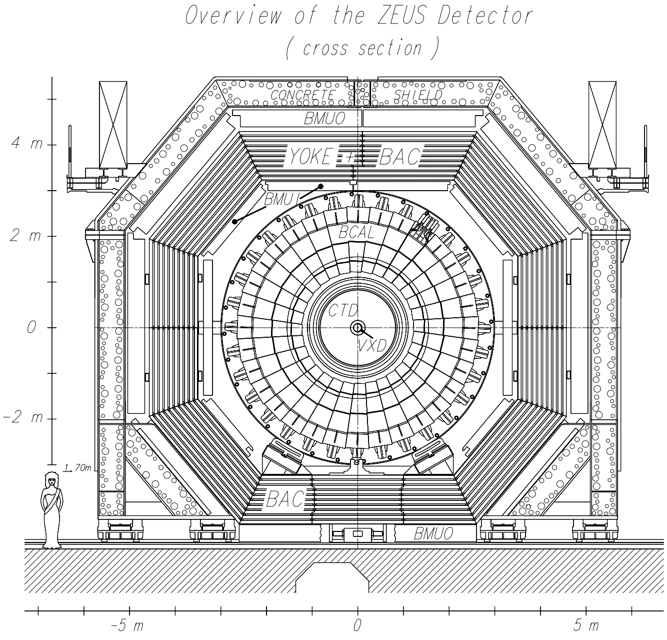

Fig. 16. Cross section of the ZEUS detector

into account the significant difference in the energies of the lepton and proton beams which results in a boost of the centre-of-mass energy in the proton direction. ZEUS was built in 1992 and is operated by a collaboration of about 500 physicists from 51 institutes in 12 different countries.

The ZEUS coordinate system is a right-handed Cartesian system, with the Z axis pointing in the proton-beam direction, referred to as the "forward direction", the Y axis pointing upwards and the X axis pointing left towards the centre of HERA. The coordinate origin ($X = Y = Z = 0$) is at the nominal interaction point (IP).

Figures 15 and 16 depict cross sections of the ZEUS detector along and perpendicularly to the beam direction, respectively. A brief overview of the main components is given below followed by the more detailed description of the essential parts involved in this analysis. A more complete description of the components can be found in [67].

In the centre of ZEUS, the Central Tracking Detector (CTD) [68–70] surrounds the IP. In the forward and rear directions additional tracking information is provided by the Forward Tracking Detector (FTD), the Transition Radiation Detectors (TRD) and the Rear Tracking Detector (RTD). The FTD and TRD together are referred to as the Forward Detector (FDET). Also, in the backward direction, the Small-angle Rear Tracking Detector (SRTD) [71] is mounted, which is a scintillator hodoscope and belongs to the tracking system. The Vertex Detector (VXD) was used around the beam pipe until 1995. The whole tracking system is surrounded by a superconducting solenoid magnet, which provides a 1.43 T magnetic field. This part of ZEUS is called the *inner detector.*

The inner detector is surrounded by the uranium - scintillator calorimeter (CAL) [72–75], which is the main part of the ZEUS detector. It consists of three parts: the forward (FCAL), barrel (BCAL) and rear (RCAL) sections. In 1998 the Forward Plug Calorimeter (FPC) [76] was added into the beam-pipe hole of the FCAL, extending the polar-angle coverage (by one unit in pseudorapidity) in the forward direction. The presampler detectors [77,78] are attached to front face of all the calorimeter sections (FPRES /BPRES/RPRES). Each consists of a 5 mm thick scintillator layer and is used to estimate the amount of energy loss in the inactive material in front of the CAL. In the RCAL and FCAL the Hadron-Electron Separator (HES) [79] consisting of a plane of $3 \times 3\,\mathrm{cm}^2$ silicon diodes is installed after three radiation lengths. The CAL is surrounded by an iron yoke which provides a return path for the magnetic field and serves as an absorber for the Backing Calorimeter (BAC) [80, 81], which measures energy leakage from the main calorimeter. Limited streamer tube chambers are located inside (FMUI/BMUI/RMUI) and outside (FMUO/BMUO/RMUO) of the yoke. Both muon chambers, inner and outer, and the yoke, which magnetic field is enhanced by additional copper coils to 1.6 T, provide a system for muon detection. In the backward direction, behind the RMUO, a veto wall detector is used to reject beam-related background. This set of subcomponents, together with the inner detector, is called the *central detector.*

Outside the central detector, in the forward direction, a lead-scintillator counter at $Z = 5.1$ m, the Proton Remnant Tagger (PRT) [82], allows to obtain information on the hadronic final state. The Leading Proton Spectrometer (LPS) [83] is installed very close to the beam pipe at distances $Z =$ 24–90 m from the IP. It consists of six silicon strip stations which detect protons scattered at small angles (transverse momentum < 1 GeV). The Forward Neutron Calorimeter (FNC) [84] is installed at $Z = 105.6$ m to detect very forward neutrons. It is a lead-scintillator sandwich calorimeter.

In order to detect leptons scattered at very low angles, the Beam Pipe Calorimeter (BPC) [85] and the Beam Pipe Tracker (BPT) have been installed on two sides of the beam pipe in the rear direction. They measure the energy and position of leptons in the angular region $3.10 < \theta < 3.12$ rad. Down the beam pipe, in the rear direction, two small lead-scintillator calorimeters (LUMIe, LUMIγ) [86–88], installed at $Z = -34$ m and $Z = -107$ m, measure an outgoing lepton and photon, respectively, for determination of the luminosity and for tagging of low-Q^2 events with $0.2 < y < 0.6$ as well as radiative events. Moreover, the additional taggers have been installed at $Z = -8$ m and $Z = -44$ m to identify photoproduction events by detecting the scattered leptons.

3.2.2 The Central Tracking Detector (CTD)

The Central Tracking Detector (CTD) [68–70] is a cylindrical wire drift chamber. It is placed inside a superconducting solenoid, which produces a 1.43 T magnetic field in the positive Z direction. The CTD measures a momentum of charged particles and estimates the energy loss dE/dx used for particle identification. The chamber has an overall length of 241 cm and an outer radius of 85 cm, covering the polar-angle region $15° < \theta < 164°$ equivalent to pseudorapidity range $2.02 > \eta > -1.96$. The CTD active volume is filled with a gas mixture consisting of 83% of argon (Ar), 5% of carbon dioxide (CO_2) and 12% of ethane (C_2H_6). Signals are collected on 4608 sense wires, located at regular intervals, with additional 19584 wires providing gain and drift fields. The CTD consists of 72 radial layers of sense wires, which are arranged into nine superlayers. A group of eight wires in the $r - \phi$ plane of each superlayer defines a cell. Altogether, the CTD contains 576 cells. One octant of the CTD is shown in Fig. 17. The special setup of the wires allows very precise measurements of the X and Y coordinates. In order to measure the Z coordinate the odd superlayers, which are axial layers, have wires parallel to the beam axis; while the even layers, which are stereo layers, are inclined about $\pm 5^0$ with respect to the beam axis. The Z-position resolution of single tracks obtained from the stereo layers is 1.0–1.4 mm, yielding an improved vertex resolution of about 2 mm. The three inner axial layers incorporate a Z-by-timing system. This system allows the reconstruction of the Z position by means of the time difference measured on both sides of the wire. Due to the poor resolution of this method, of about 4 cm, it is only used for trigger purposes. In the $r - \phi$ plane, the position resolution of the CTD is 120–130 µm for a single track and about 1 mm for the event vertex. The CTD transverse-momentum resolution for full-length tracks is $\sigma(p_T)/p_T = 0.0058 p_T \oplus 0.0065 \oplus 0.0014/p_T$ [89], with p_T in GeV and $\oplus$ denoting the addition in quadrature. The first term represents the intrinsic resolution of the CTD, while the second and third terms account for multiple scattering of charged particles inside and in front of the CTD, respectively.

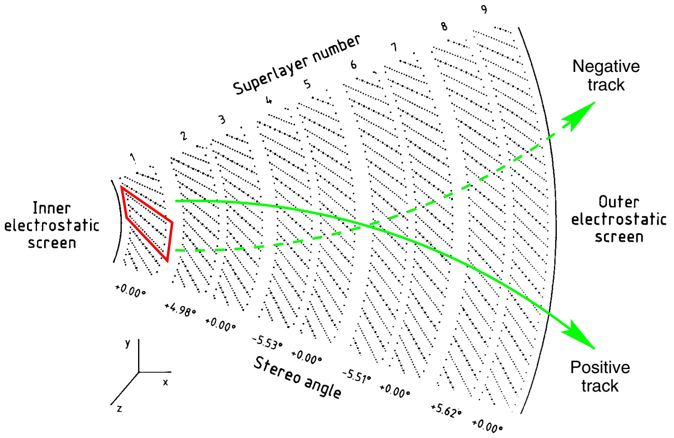

Fig. 17. $X - Y$ cross section through one octant of the CTD. The large dots indicate the sense wires. Examples of paths traversed by negative and positive tracks are shown, as well as the contour of a cell

In this analysis the CTD was used for reconstruction of an event vertex and the measurement of a track associated to the particle, i.e. its position reconstructed with the polar coordinates determined by the track. It was also used for measuring the momentum of the particle associated with the track, its charge, as well as the energy loss dE/dx used for particle identification.

3.2.3 The Uranium Calorimeter (CAL)

The Uranium Calorimeter (CAL) [72–75] is the main ZEUS calorimeter. It is the most essential detector for reconstruct-

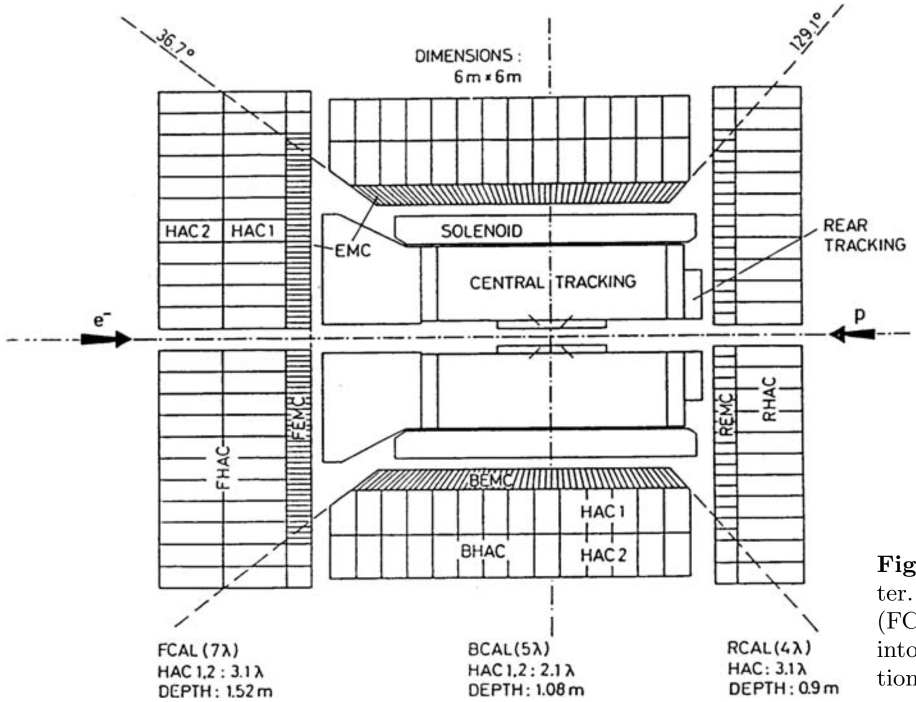

Fig. 18. Schematic view of the ZEUS calorimeter. The three parts of the CAL are shown (FCAL/BCAL/RCAL) and their subdivision into EMC and HAC sections. λ is the interaction length

ing of the *ep*-scattering final state and plays a crucial rôle in the analysis.

The CAL is a sampling calorimeter consisting of alternating layers of 3.3 mm, what is about $1X_0$ (X_0 is the radiation length) of the depleted uranium (^{238}U) as an absorber and of 2.6 mm of the organic scintillator as an active material serving for sampling the energy deposits. The background coming from natural radioactivity of uranium is used for calibration of each CAL channel, what is performed once a day. The thicknesses of both materials have been optimised to achieve a compensating calorimeter, which has the same response to electromagnetic and hadronic particles of equal energy. The energy resolution measured under test-beam conditions for leptons is

$$\frac{\sigma(E)}{E} = \frac{18\%}{\sqrt{E(\mathrm{GeV})}} \oplus 1\%,$$

and for hadrons

$$\frac{\sigma(E)}{E} = \frac{35\%}{\sqrt{E(\mathrm{GeV})}} \oplus 2\%.$$

The CAL consists of three parts: forward (FCAL), with an polar-angle coverage of $2.5^0 < \theta < 39.9^0$ ($3.8 > \eta > 1.0$), barrel (BCAL) with $36.7^0 < \theta < 129.1^0$ ($1.1 > \eta > -0.7$) and rear (RCAL) which covers the range $128.1^0 < \theta < 176.5^0$ ($-0.7 > \eta > -3.5$), as shown in Fig. 18. The overall solid angle coverage of the CAL is 99.8% in the forward direction and 99.5% in the backward direction. Each part of the CAL is subdivided into electromagnetic (EMC) and hadronic (HAC) sections. The RCAL consists of one HAC part, while the BCAL and FCAL contain two HAC modules.

The CAL also provides information on the position of incident particles. The position resolution depends on the

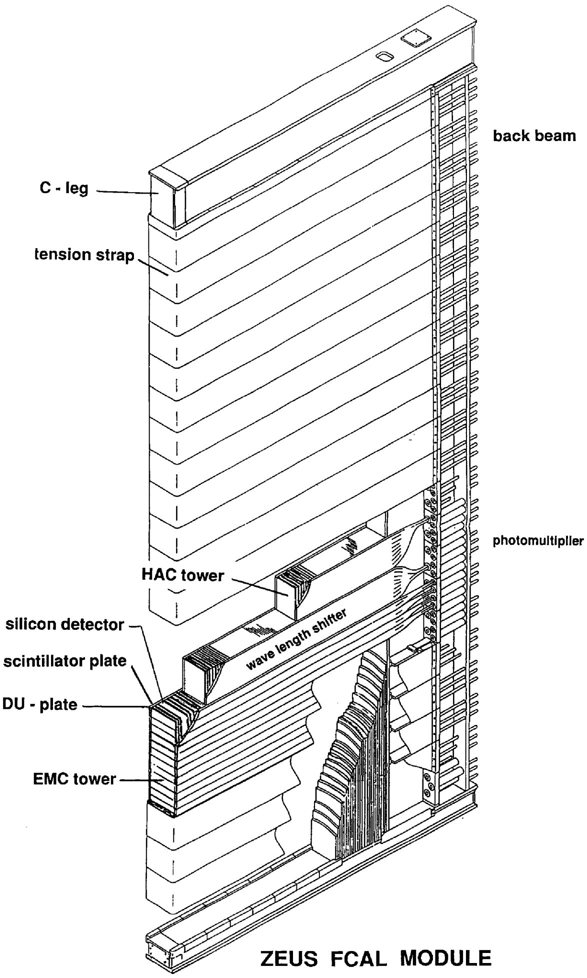

Fig. 19. Module of the FCAL

detector granularity. The EMC and HAC sections constitute cells arranged into towers. Each tower is segmented longitudinally into one inner EMC and two (or one in the RCAL) outer hadronic sections (HAC1 and HAC2). Towers are grouped in modules. An example of the FCAL module is depicted in Fig. 19. The size of cells varies depending on their position and destination in the CAL. EMC cells have the typical size of $5 \times 20\,\mathrm{cm}^2$ in the FCAL and BCAL, and $5 \times 10\,\mathrm{cm}^2$ in the RCAL, while HAC cells have typically $20 \times 20\,\mathrm{cm}^2$ size.

Signals from each cell are read out on two opposite sides by a pair of photomultipliers (PMTs) coupled to the scintillator via wavelength shifters and optical fibres. The energy measurement is independent on the position of the particle within the cell since the signals from both PMTs are summed up. A comparison of the two signals provides information on the horizontal impact position of a particle.

Moreover, the CAL can give information on the time of incidence. Timing is measured at a level less than 1 ns for energies above 4.5 GeV. It is mainly used by the trigger system to reduce background due to beam-gas events.

The CAL is the important component used in this analysis. It was used to detect the scattered lepton and a photon, to measure their energy and position outside the region in which the CTD could not be used. It played an important rôle in the reconstruction of the kinematic variables for low-Q^2 events.

3.2.4 The Small-angle Rear Tracking Detector (SRTD)

The Small-angle Rear Tracking Detector (SRTD) [71] is attached to the front face of the RCAL at $Z = -148\,\mathrm{cm}$ (see Fig. 20). It was installed to improve the measurement of the energy and angle of the scattered electron for low-Q^2 events.

The SRTD consists of a horizontal and a vertical layer of 1 cm wide and 0.5 cm thick scintillator strips. Scintillator strips are read out via optical fibres and PMTs. It covers the region $68 \times 68\,\mathrm{cm}^2$ in X and Y with the exclusion of a $8 \times 20\,\mathrm{cm}^2$ hole at the centre for the beam pipe. The SRTD provides a transverse-position resolution of 3 mm.

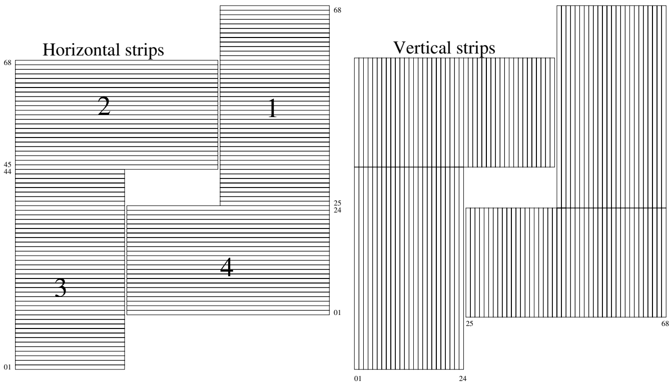

Fig. 20. Orientation and numbering scheme of the strips of the two SRTD planes. The strip size is 0.98×24 (44) cm^2. The asymmetric shape is due to the movement of the RCAL modules in 1995 in order to reduce the beam-hole size

Leptons, which lose energy through showering in the inactive material in front of the CAL, deposit more energy in the SRTD than non-showering leptons. Thus, the measured energy deposit in the SRTD can be used to correct for this energy loss. Moreover, the SRTD also provides a fast time measurement (resolution $\sim 2\,\mathrm{ns}$), what is used to reject background events at the trigger level.

In this analysis, the SRTD was used to measure the position of photons and leptons scattered at small angles relative to the lepton-beam direction. Moreover, signals from this detector allowed for energy corrections due to particle showering in the inactive material in front of the CAL.

3.2.5 The Hadron-Electron Separator (HES)

The Hadron-Electron Separator (HES) [79] is placed in the RCAL (RHES) and FCAL (FHES). It consists of $3 \times 3\,\mathrm{cm}^2$ silicon diodes placed at a longitudinal depth of three radiation lengths, which corresponds to the approximate position of the maximum of the electromagnetic shower in the CAL. The separation between leptons and hadrons is based on the fact that the hadronic interaction length is 20 times larger than the electromagnetic radiation length. Therefore, hadrons produce smaller HES signals.

In this analysis, the fine segmentation of the RHES was used to improve the position resolution for both scattered leptons and photons.

3.2.6 The presampler

Presampler detectors (FPRES/RPRES) [77, 78] are mounted in front of the FCAL and RCAL[5]. They consist of a layer of scintillator tiles: wavelength-shifting fibres, embedded in the scintillator, guide the scintillation light to PMTs. Particles, which shower in the inactive material in front of the presampler, lead to an increased particle multiplicity which is measured by the presampler. The combined information from the presampler and the CAL allows an event-by-event measurement of the energy loss in front of the CAL and, thus, allows to recover the calibration and energy resolution of the ZEUS calorimeter.

The segmentation of the presampler matches that of the HAC sections of the CAL, $20 \times 20\,\mathrm{cm}^2$. Figure 21 shows the coverage of the CAL by the presampler. The segmentation of the EMC sections is shown, which is finer in the region not shielded from the nominal IP by the BCAL. The $20 \times 20\,\mathrm{cm}^2$ towers covered by the presampler tiles are shaded.

In this analysis, only the information from the RPRES was used to correct the energy of the final-state particles.

3.2.7 The Proton Remnant Tagger (PRT)

The Proton Remnant Tagger (PRT) [82] consists of seven pairs of scintillator counters surrounding the beam pipe

---

[5] The barrel presampler (BPRES) information is also available but only for data starting in January 1999.

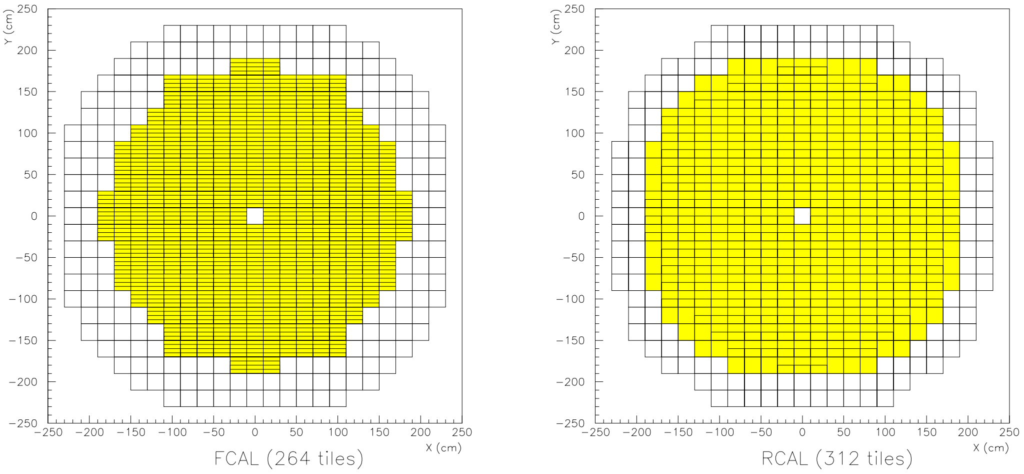

Fig. 21. Front view of the FCAL and RCAL. The $20 \times 20\,\mathrm{cm}^2$ white square in the centre corresponds to the hole of the beam pipe. The coverage of the presampler is indicated by the shaded region

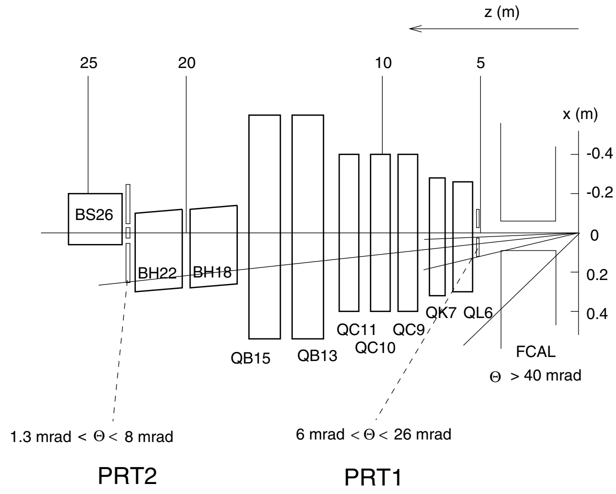

Fig. 22. Position of the PRT1 and PRT2 counters with respect to the HERA magnets and their angular coverage

at three positions in the forward proton direction. The scintillators of each counter are of rectangular shape with a small hole to accommodate the beam pipe. The counters in a pair are of equal shape covering the same area. Coinciding signals observed in a pair allows high energy particles to be detected, while suppressing backgrounds due to soft particles, including synchrotron radiation photons.

Two pairs of detectors (PRT1) are located at $Z = 5.15\,\mathrm{m}$ and five pairs (PRT2) are installed at $Z = 24.4\,\mathrm{m}$, shown in Fig. 22. The PRT1 and PRT2 tag particles in the θ-angle range 6 to 26 mrad and 1.3 to 8 mrad, respectively. The PRT detects high energy charged particles which leave the ZEUS interaction region at very small angles and escape the central detector through the beam pipe.

In this analysis, only the PRT1 was used, because at sufficiently high $|t|$ ($|t| > 0.5\,\mathrm{GeV}^2$) some fraction of elastic events, where the scattered proton stays intact, yields a signal from the outgoing proton in the PRT2 counters. The PRT1 is built out of two 2.6 mm thick layers of scintillator separated by a 1 mm thick layer of lead and shielded by the lead (2 mm) and stainless steel (0.5 mm) foils. Each of the scintillator layers is split into two halves independently read out by two PMTs. The PRT1 has an active area of $30 \times 26\,\mathrm{cm}^2$ with a hole of $6.0 \times 4.5\,\mathrm{cm}^2$ at the centre. It covers the pseudorapidity range $4.3 < \eta < 5.8$. It was used up to the end of the 1997 running period for tagging events in which the proton diffractively dissociated.

3.2.8 The Forward Plug Calorimeter (FPC)

The Forward Plug Calorimeter (FPC) [76] is a lead - scintillator sandwich calorimeter with readout via wavelength -shifter fibres. It was installed in 1998 in the $20 \times 20\,\mathrm{cm}^2$ beam hole of the FCAL and has a small hole of radius 3.15 cm in the centre to accommodate the beam pipe as illustrated in Fig. 23. It extends the pseudorapidity coverage of the FCAL from $\eta < 4.0$ to $\eta < 5.0$. The FPC is devoted to detect particles coming from the dissociation of the proton in ep collisions.

The active part of the FPC has outer dimensions of $192 \times 192 \times 1080\,\mathrm{mm}^3$. It is built up of 15 mm thick lead plates alternated with scintillator layers of 2.6 mm thick. The FPC is longitudinally subdivided into electromagnetic (EMC) and hadronic (HAC) sections which are read out separately. The EMC section consists of 10 layers of lead and scintillator while the HAC part consists of 50 layers. The scintillator layers consist of tiles and form cells. The cell cross sections are $24 \times 24\,\mathrm{mm}^2$ in the EMC and $48 \times 48\,\mathrm{mm}^2$ in the HAC sections. There are 60 cells of the EMC and 16 of HAC part.

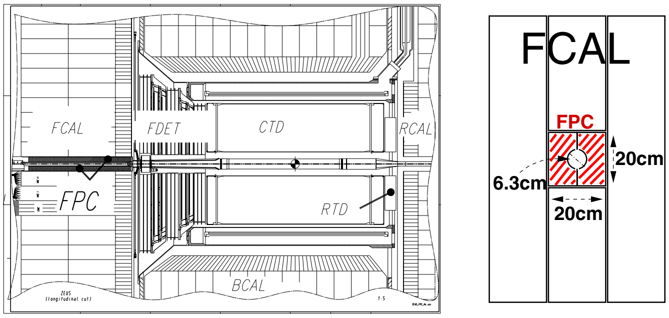

Fig. 23. Longitudinal cut of the inner part of the ZEUS detector and front view of the FCAL with the FPC dashed

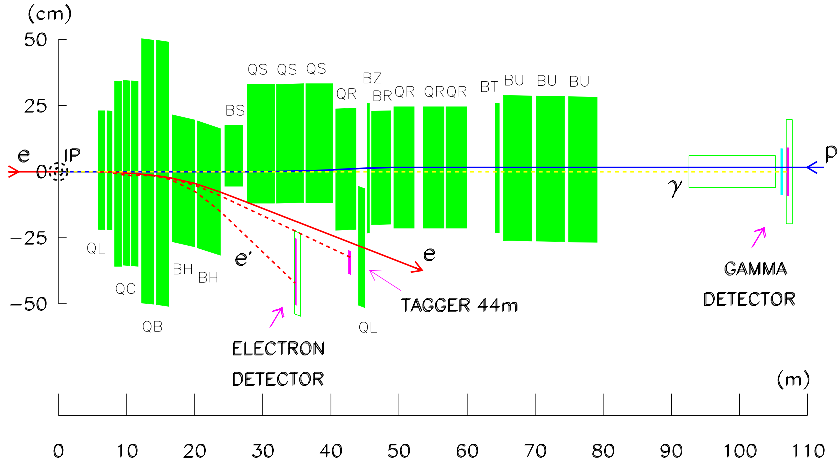

Fig. 24. General layout of the ZEUS luminosity monitor

Results obtained with a lead-scintillator calorimeter of similar composition show that the FPC is expected to be compensating ($e/h = 1$) [90]. The energy resolution for electrons was found to be $\sigma_E/E = 34\%/\sqrt{E} \oplus 7\%$ and for pions the energy resolution of combined signals from the FPC and the surrounding FCAL was determined to be $\sigma_E/E = 53\%/\sqrt{E} \oplus 11\% \oplus 3\% \ln E$ [91]. The last term in the expression of the energy resolution for hadrons is due to the longitudinal leakage of energy.

The FPC was used to remove low-mass proton- dissociative events from this analysis for the data belonging to the 1998–2000 running periods.

3.2.9 The Luminosity Monitor (LUMI)

The event rate R in a collider is proportional to the interaction cross section σ and the factor of proportionality is called the luminosity $\mathcal{L}$

$$R = \mathcal{L} \cdot \sigma. \qquad (5)$$

The value of the luminosity depends on the parameters of the beam of the collider and can be determined either from those or directly from the definition. The measurement of the time-integrated luminosity is essential in any extraction of cross sections in high energy physics experiments.

In the ZEUS experiment, the luminosity is determined from (5) measuring the rate of bremsstrahlung events produced by the Bethe-Heitler process, $ep \rightarrow e'\gamma p'$ [92, 93]. The cross section for this particular process is large and precisely known from QED with an accuracy of 0.5%. Moreover, it has a clean experimental signature, namely the coincidence of a photon and a lepton at small angles with respect to the lepton beam, with energies which add up to the initial-lepton energy. Although originally a coincidence measurement of the scattered lepton and the photon was planned, the rate of the photons alone was found to provide a precise measurement of the luminosity [94].

Since the bremsstrahlung photon and lepton emerge at very small angles, both particles propagate inside the proton beam pipe. At about 80 m from the IP photons can leave the pipe because it is bent upwards. The exit window for the photons is installed at $Z = -92.5$ m, while the position for the photon detector is at $Z = -107$ m, as shown in Fig. 24.

The ZEUS luminosity is measured detecting energy of bremsstrahlung photons. The photons cross a copper-beryllium window with $0.095X_0$ thickness, then a 12.7 m long vacuum pipe, which ends at an absorber that shields against the large flux of direct synchrotron radiation. It is made out of a $3.5X_0$ carbon block. The photons are registered by a lead-scintillator sampling calorimeter (LUMIγ) which also measures the shower position. The transverse dimensions of the LUMIγ calorimeter are $18 \times 18\,\mathrm{cm}^2$ and its depth is $22X_0$. The energy resolution of the LUMIγ detector was found to be $18\%/\sqrt{E(\mathrm{GeV})}$ in test beam measurements, but under the ZEUS experimental conditions it has degraded to only $23\%/\sqrt{E(\mathrm{GeV})}$. The measurement of the photon rate is corrected for a background coming from bremsstrahlung of leptons with residual gas. This is carried out by means of empty proton bunches as a reference. A detailed description of the luminosity monitor system (LUMI) can be found elsewhere [86–88].

In the ZEUS experiment the luminosity can be measured with a systematic uncertainty of about 1% dominated by the acceptance uncertainty.

3.2.10 The ZEUS trigger and data acquisition system

The high bunch-crossing frequency and large background rate pose difficulties for the readout and triggering.

The ZEUS trigger system has three levels. Its task is to select interesting ep physics events among many background events. The total event rate at HERA is dominated by interactions of the proton beam with residual gas in the beam pipe. This background is of the order of 10–100 kHz, whereas the rate of ep physics events, after excluding a very low-Q^2 region, is only of the order of a few Hz. A schematic diagram of the ZEUS trigger and data acquisition chain is shown in Fig. 25.

The first level trigger (FLT) has to reach a decision in 3 µs and reduce the rate to less than 1 kHz. The FLT is a hardware trigger. It uses information from many detectors and requires a global decision based on trigger information

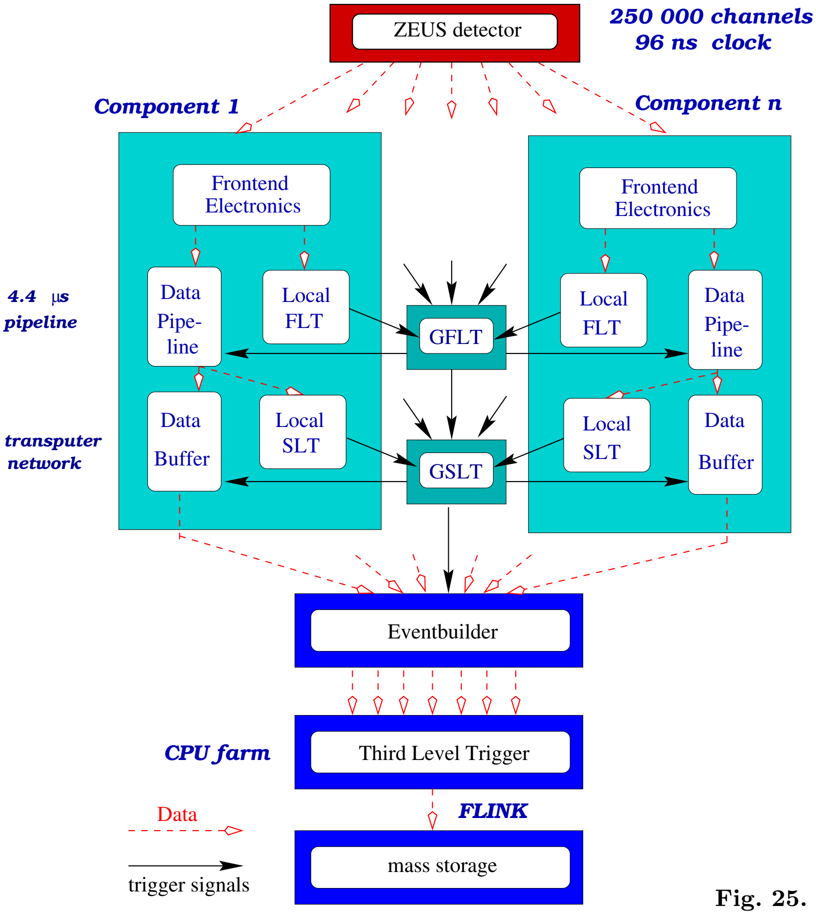

Fig. 25. The ZEUS trigger and data acquisition system

derived from the separate detectors. The signal collection and transfer to the decision making system depends on the detector device. The data from every bunch crossing are stored in pipelines which are 46 bunch-crossing deep and allow for a 4.4 μs latency per event. Central for the ZEUS data acquisition system is the pipelining of the ZEUS calorimeter. If the trigger decision is positive the data must be recovered from the pipeline, because the data are overwritten as the pipeline is continuously recording new data. The trigger information from the components of the ZEUS detector are sent to the global first level trigger (GFLT) between 1.0 and 2.5 μs after the crossing occurred. The GFLT is issued exactly after 46 bunch crossings. If the GFLT decides to keep the event the data are passed on to the next trigger level.

The second level trigger (SLT) is designed to reduce the trigger rate below 100 Hz. Typically, the SLT decision takes 30 μs introducing about 2% dead time. The SLT is software-based. At this level a transputer network calculates objects like track momenta, the event vertex or calorimeter clusters which allow a more restrictive trigger decision. As in the case of the FLT, each component has its own local SLT process, passing information to the global second level trigger (GSLT) which then takes the decision to accept or reject the event. If the GSLT decision is positive, all components send the data to the Event Builder, which combines the information for the event, writes it into the final data format (ADAMO) and makes it accessible to the next trigger level.

The third trigger level (TLT) performs part of the offline analysis on a farm of Silicon Graphics (SGI) CPUs. At this level, detailed tracking as well as jet and electron finding are performed. The TLT accepts events at a rate below 10 Hz. The events have a typical data size of about 100 kB in the ADAMO format. They are written to disks at the DESY computing centre via a fibre-link (FLINK) connection. Here they are available for offline reconstruction and analysis.

4 Event reconstruction

After the selection of data by the trigger system corresponding to the physics analysis (see Sect. 3.2.10), events are reconstructed offline by means of the ZEUS Physics Reconstruction program (ZEPHYR) [95]. Information from all the components is merged together by ZEPHYR to build up a reconstructed event. At the beginning the signals coming from all the components of the ZEUS detector are scaled using calibration constants. Then the reconstruction of physics events in ZEPHYR runs through three phases:

1. reconstruction of the signal coming from the individual components of ZEUS,
2. global track matching, global cluster finding in all the components and subsequent matching of tracks and clusters,

3. particle identification by combining measurements from all the detectors.

The most significant information, needed for the proper calculation of cross sections in the present analysis comes from track and vertex data from the CTD, the energy and position reconstruction in the CAL and the reconstruction of the energy and position by means of the SRTD, the HES and the presampler.

In the following, the general methods for passing from the electronic signal in the detector to physics information like energy deposit and impact position for various ZEUS components used in this analysis are described. Moreover, correction methods for position and energy of the final-state particles are explained.

4.1 Track and vertex reconstruction

The interaction point in which the *ep* scattering takes place is called the *primary vertex*, or simply the *vertex*. Subsequent decays of particles in the final state and interactions may produce secondary vertices. A precise determination of the vertex is desired in order to get an unbiased measurement of kinematic variables.

The track reconstruction is based on the package VCTRACK [96]. This package reconstructs tracks and finds the primary and secondary vertices. For the purposes of this analysis it was working in the *CTD only* mode what means that tracks were reconstructed basing only on the information from nine superlayers of the CTD. For the determination of the vertex, only tracks that cross the first superlayer of the CTD are considered. The fitted trajectories are extrapolated to the beam line. The result of extrapolation of all the tracks is averaged to obtain the primary vertex. Then a next fit is performed to determine the trajectories with the constraint of being originated from the primary vertex. A χ^2 value from the fit of each trajectory is evaluated and tracks with too large χ^2 are discarded. Tracks which originate from the primary vertex are called *vertex tracks.*

An accuracy of 2 mm is achieved for the reconstruction of the vertex coordinate Z_{vtx}. The distribution of Z_{vtx}, shown in Fig. 26, has a central peak at $Z_{\mathrm{vtx}} \approx 0$ cm. The length of the proton bunch is bigger than the length of the electron[6] one, so electrons can collide with protons over an extended longitudinal Z range. The spread of the central peak of the Z_{vtx} coordinate reflects this fact. The clear shoulder visible at $Z_{\mathrm{vtx}} = +70$ cm comes from events where electrons collide with protons in forward "satellite bunches". Since the detector acceptance depends on the vertex position, the Monte Carlo (MC) vertex distribution has to follow the data, what is seen in Fig. 26.

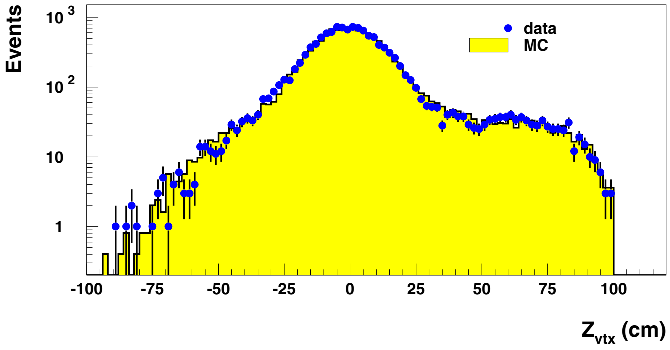

Fig. 26. Distribution of the Z_{vtx} coordinate of the vertex for the data (points) and the MC simulation (histogram)

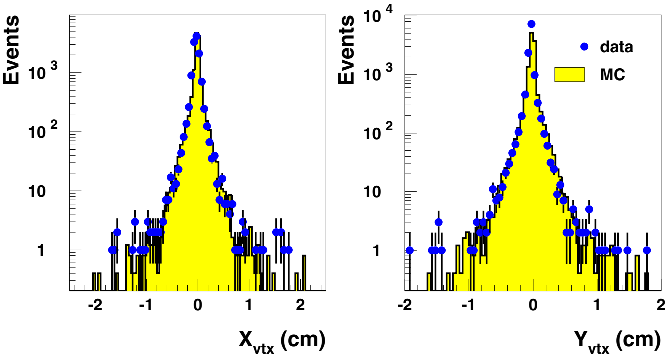

Fig. 27. Distribution of the X_{vtx} and Y_{vtx} coordinates of the vertex for the data (points) and the MC simulation (histogram)

The distributions of the X_{vtx} and Y_{vtx} coordinates are shown in Fig. 27. Since the beam in these directions is more collimated than in the Z direction, the X_{vtx} and Y_{vtx} distributions are much narrower. The accuracy of the X_{vtx} (Y_{vtx}) vertex position reconstruction is about 1 mm while the beam width is only 200 (50) µm. Therefore, in the analysis, the X_{vtx} and Y_{vtx} coordinates are set to the average values of the corresponding run.

After the final selection cuts described in Sect. 5.6 were applied, an average of 35% of all selected events have no track and, therefore, no vertex. For those events the nominal position of the vertex $X_{\mathrm{vtx}} = Y_{\mathrm{vtx}} = Z_{\mathrm{vtx}} = 0$ was assumed.

4.2 CAL reconstruction

The reconstruction of signals coming from the CAL is performed by the CCRECON [97,98] package. The first phase of the event reconstruction is the correct determination of the energy deposited in cells, next is the reconstruction of position, energy and direction of particle showers, the search for jets by clustering the cells and finally the tentative identification of the reconstructed objects.

The raw data are calibrated using calibration of the CAL by means of uranium noise. Then the cell energies are corrected cell-by-cell removing noisy cells and sparks[7]. After the noise corrections were applied, the energy-scale[8] correction is implemented according to the results in [99]. Then from these cell energies the local clustering starts. In this geometrical clustering cells are grouped according to their physical adjacency. Output objects are called

---

[6] Hereafter, both e^+ and e^- are referred to as electrons, unless explicitly stated otherwise.

[7] Definition of sparks is given in Sect. 5.4.2.

[8] Energy scale is defined as a function which transforms energy deposit in a detector to the particle energy.

condensates. They serve as the starting point for the reconstruction of single particle showers. Found condensates are tentatively identified using the different showering properties of various particles and the segmentation of the CAL.

From this stage on, the SINISTRA95 package, described in Sect. 5.2, is used to find the energy and position of particles in the CAL. It also uses information from other detectors and on this basis performs particle identification.

4.3 Reconstruction of energy and position using the SRTD

For particles which hit the RCAL in the vicinity of the beam hole the position measurement is improved using the SRTD. This detector allows to obtain the electron impact position with a resolution of $\sigma_{X,Y}^{\mathrm{SRTD}} \sim 3.5\,\mathrm{mm}$ [100] due to fine granularity of 1 cm wide strips of this device.

The clustering procedure in the SRTD is based on the assumption that all strips with less than two empty strips in between belong to one cluster. Empty strips are defined as strips with deposits below the noise threshold. Following this assumption one has to notice that dead channels in the SRTD have rather severe impact on the clustering algorithm - a gap of 2 cm wide can be created in the distribution of the reconstructed position. To reduce this effect, the energy of strips from the dead channel list is taken as the average energy of the two neighbouring strips.

If at most one particle hits a SRTD quadrant, the reconstruction of the X and Y position is unique. If more than one particle hits a quadrant the clustering algorithm yields several X and Y coordinates. Matching two or more SRTD hits gives long tails in the resolution. Therefore, to solve this problem, the SRTD cluster is considered, if it is within 4 cm of either the CAL or the RHES cluster position.

The SRTD signals are calibrated relative to the signal of a minimum-ionising particle (MIP) which is defined as the average response of the detector to a single particle traversing the SRTD perpendicularly. The reconstructed energy is the sum of deposits in all strips belonging to the cluster in both SRTD planes. Thus, the energy deposit E_{SRTD} corresponding to the hit (used in the energy correction formula quoted in Sect. 4.6) is half of this energy.

The calculation of the shower position is performed in the same way for X and Y coordinates. First of all, the shower maximum has to be found. It is defined as the strip of x coordinate for which $\alpha E(x-1) + E(x) + \alpha E(x+1)$ is maximal, where α is a parameter chosen to be $\alpha = 0.5$ for the 1994 data [100]. This weighted 3-strips sum is used instead of the simple energy of one strip since it is less sensitive to shower development and fluctuations of the number of photoelectrons in a PMT. Then the centre of gravity is calculated using only three central strips of the shower maximum. Further a correction to this position is applied to compensate for the bias of this algorithm towards the central strip ([100] and references therein).

The SRTD can also be used to correct the calorimeter energy deposits for the loss of particle energy in the inactive material in the RCAL beam-pipe region. For electrons traversing through a large amount of dead material before reaching the SRTD, the energy deposits in the SRTD due to the developed showers are large. The procedure of correcting the energy measurement for this effect is described in Sect. 4.6.

4.4 Reconstruction of position using the HES

The HES can be used to reconstruct the position of a particle hitting the RCAL. Due to the small size of a diode of $3 \times 3\,\mathrm{cm}^2$ this can be done with the position resolution for electrons of $\sigma_{X,Y}^{\mathrm{HES}} \sim 5\,\mathrm{mm}$ [101], which for X is almost a factor of two better than of the CAL, while for Y it is only slightly better in the HES. There is a significant difference between hadron and electron deposits in the HES. Hadrons usually produce an energy deposit in one diode only, so the position resolution for them is rather poor. For electrons a much better position resolution can be achieved, as the HES is situated near the shower maximum, where more than one diode shows a signal.

For the position reconstruction the cluster of 3×3 diodes is considered. It is searched for around the coordinates of the impact position in the RCAL in the search area being either a circle or a box. In this analysis the cluster was built up using the circle with $r = 10\,\mathrm{cm}$. Starting with the diode with the highest energy deposit, a 3×3 cluster in the HES is formed with the starting diode in its centre. In case when the starting diode is at the edge or a corner of the HES area, the cluster is reduced to only six or four diodes, respectively.

The reconstructed HES position is given as

$$X = \frac{\sum_{i=1}^{N} E_i \cdot X_i}{\sum_{i=1}^{N} E_i},$$

where X_i and E_i are the position of the centre and energy deposit of the $i-$th diode. The analogous expression is used also for the Y coordinate. This linear weighting has an disadvantage that most positions are biased to the centre of the diode with the highest energy deposit. In [101] the logarithmic-weighting method was developed, which was applied in this analysis.

4.5 Reconstruction of energy using the presampler

The dead material situated between the *ep* interaction point and the front face of the CAL leads to a degradation of the energy measurement of particles.

Particles which initiate showers in the dead material in front of the RCAL lead to an increased particle multiplicity which is measured by the RPRES. The combined information from the RPRES and the RCAL allows an event-by-event measurement of the energy loss in front of the RCAL and thus allows to recover energy resolution of the ZEUS calorimeter [102,103].

In the clustering algorithm, the CAL position of the particle hit is projected onto the RPRES surface. The $20 \times 20\,\mathrm{cm}^2$ tile which is a result of this projection is called the *central tile*. Then the cluster is built up. It consists of the central tile and either 8 or 24 surrounding tiles. The RPRES signal E_{RPRES} is the sum of energies of all tiles belonging to the cluster. In this analysis clusters consisting of 3×3 tiles were used.

4.6 Corrections for energy and position

The energy loss due to showering in the dead material in front of the RCAL was estimated using the energy deposited in the SRTD and the RPRES. The idea of the energy correction method is that the energy loss is related to the number of interactions in that material, thus, to the multiplicity of the resulting shower particles. The energy measured in the RCAL, E_{CAL}, was corrected using the relation proposed in [102, 103]

$$E_{\mathrm{corr}} = E_{\mathrm{CAL}} + C \cdot x, \qquad (6)$$

where $x = E_{\mathrm{RPRES}}$ or $x = E_{\mathrm{SRTD}}$. The coefficient C was evaluated using the kinematic peak events i.e. the events for which the distribution of the electron energy is sharply peaked near the electron-beam energy, i.e. 27.5 GeV. It depends on the position in the RCAL and was determined for the data and MC sample separately. In this analysis, (6) was applied for all particles depositing an energy above the noise suppression threshold either in the SRTD or in the RPRES before reaching the RCAL.

The energy of charged particle reaching the BCAL was corrected using the measurement of a track from the CTD [104]. When the charged particle hits the BCAL, two independent measurements of energy i.e. the momentum of the track and the calorimeter energy are available. The advantage is that when the momentum of the track is measured, the charged particle has not travelled through as much inactive material as when it reaches the BCAL. So the CTD measurement is closer to the true energy of the particle. In the BCAL the total momentum of the track was taken as the "true" energy of the charged particle. For photons hitting the BCAL the energy deposit from the BCAL was used.

Cracks between towers and cells of the CAL cause non-uniformities in the detector response. After the above energy corrections were implemented, an event-by-event correction factor due to non-uniformities for the measured particle energy was applied. In the region close to the cracks the event-by-event correction factor varied between 1.0 and 1.15, otherwise it was 1.0.

In Fig. 28 one can see the average correction factor $E_{\mathrm{corr}}/E_{\mathrm{CAL}}$ due to inactive material and non-uniformities as a function of $r = \sqrt{X^2 + Y^2}$ for events in the RCAL. For dead material the average correction factor is an increasing function of r. At high r values it reaches 1.1 for the data while the MC points are always below. The average correction factor due to non-uniformities is at most 1.01 for $r < 40$ cm values and it vanishes at $r > 40$ cm.

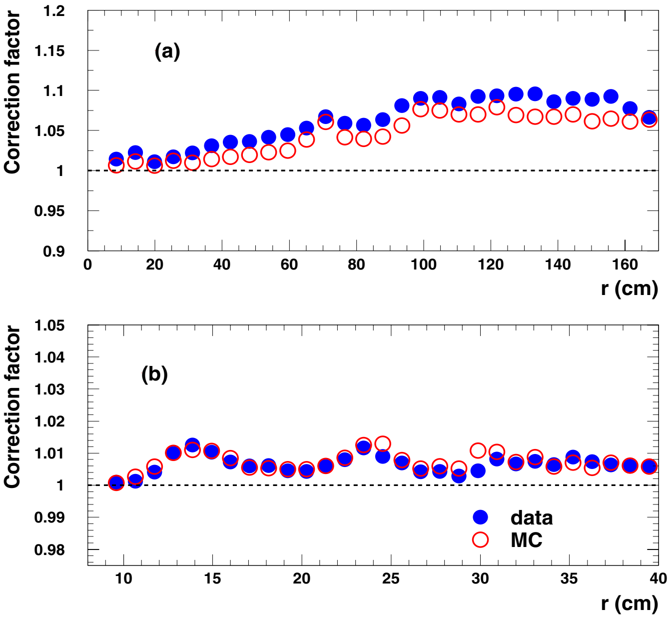

Fig. 28. Correction factor for energy due to presence of **a** dead material and **b** non-uniformities in the RCAL. The data points (solid) are compared with the MC simulation (open)

Figure 29 shows the fraction of events for which energy deposited in the CAL was corrected for energy loss in inactive material using either the SRTD or the RPRES detectors. For those events for which no correction was made, the RCAL or the BCAL deposits were used in the analysis depending on the impact position of the final-state particles. For electrons more than 80% events were corrected by means of the SRTD, while only about 10% events by means of the RPRES. For photons the fractions of events corrected using the SRTD and the RPRES are about 55% and 25%, respectively. For about 20% photons hitting the RCAL, the calorimeter deposits were not corrected because their deposits were too small in the SRTD and in the RPRES. For the electrons the data and the MC simulation agree, while for the photons the MC histogram has different shape than the data one. It is due to tuning this correction method to the electrons only from DIS.

The measurement of the impact position obtained from the CAL (see Sect. 5.2) was improved using the position reconstructions in the CTD, the SRTD and the RHES whenever the particle trajectory was within the respective acceptance regions.

The rear impact position was measured by means of the SRTD if the particle hit the RCAL face up to 1 cm from the beam hole. The RHES information was used to improve the RCAL measurement of the particle impact position outside the SRTD looking for the RHES cluster closest to the calorimeter cluster. If the distance between the clusters was less than 6 cm and the total signal of the RHES cluster was greater than 40 MIPs the calorimeter position was replaced by the RHES position.

The positions of charged particles which finally reached the BCAL were determined with high accuracy using the track information from the CTD, since it provides the best polar angle resolution of 2.5 mrad.

In Fig. 29 the fraction of events with position corrected using either the RHES, the SRTD or the CTD is depicted. For non-corrected events the CAL impact position was used in the final analysis. About 90% of electrons hit the RCAL

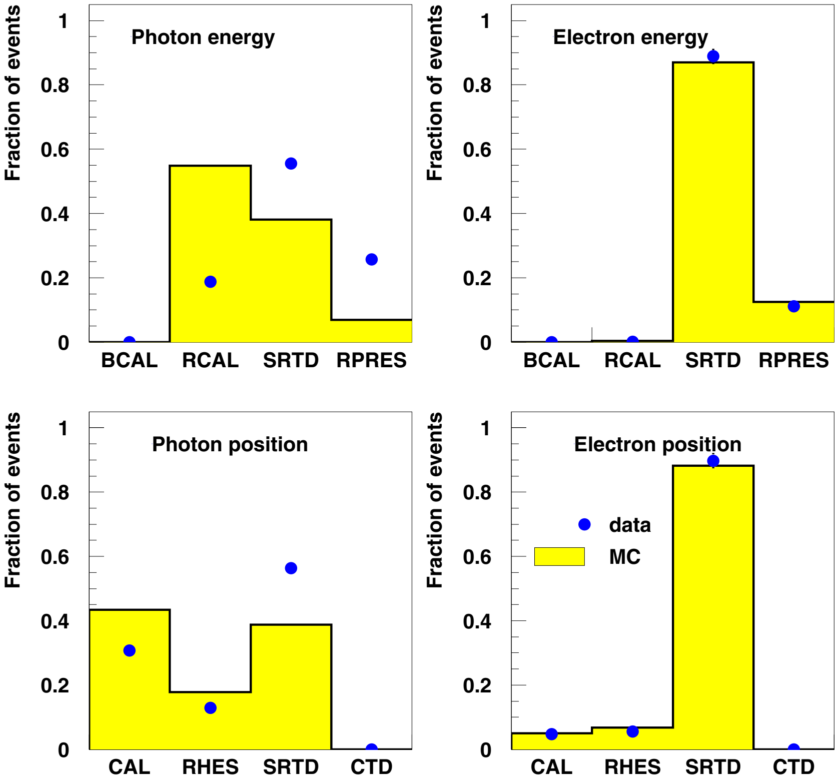

Fig. 29. (Upper) Fraction of events for which the BCAL, the RCAL, the SRTD or the RPRES energy corrections were applied for photons (left) or electrons (right). The data (points) are compared with the MC simulation (histogram). (Lower) For the position reconstruction the fraction of events which were corrected using the CAL, the RHES, the SRTD or the CTD

within the SRTD acceptance and the SRTD cluster was used to correct the position. Only about 5% events were reconstructed using the RHES information. The remaining 5% events did not deposit significant signals neither in the SRTD nor in the RHES and since they were not within the CTD acceptance, the CAL deposits were used for the position reconstruction. The data for electrons agree well with the MC simulation.

For photons only 60% events were corrected using the SRTD, about 15% with the RHES and for about 30% events the position from the CAL was used. The fraction of events with the photon deposits in the RCAL in the MC sample differs from the data. The overall number of events corrected using the SRTD is significantly lower ($\sim 40\%$) in the MC simulation. This may suggest that the MC simulation does not reproduce properly a photon showering in a dead material before the RCAL and then traversing the SRTD. Again this disagreement between the data and the MC simulation is due to tuning this correction method to the electrons only from DIS.

5 Reconstruction and selection of DVCS events

In the following, the kinematics of the DVCS process is defined. Moreover, a method to identify and reconstruct of particle energy and position in DVCS is depicted. Further several methods for the reconstruction of kinematic variables are presented. Then the online and offline DVCS events selection is shown. Finally, the analysis strategy is described.

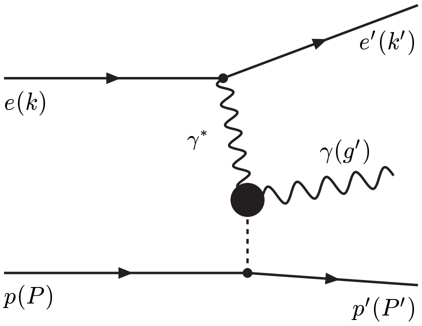

Fig. 30. Schematic representation of a DVCS event

5.1 Kinematics of DVCS

In a DVCS event the incoming electron with four-momentum k is scattered off a proton with four-momentum P. After the scattering the four-momentum of the electron is k', the four-momentum of the photon is g' and the four-momentum of the proton is P'. This is illustrated in Fig. 30.

In the ZEUS coordinate system, the four-momenta for the process $ep \to e'\gamma p'$ can be written (neglecting the particles' rest mass)

- for the initial-state particles:

$$k = \begin{pmatrix} E_e \\ 0 \\ 0 \\ -E_e \end{pmatrix}, \quad P = \begin{pmatrix} E_p \\ 0 \\ 0 \\ E_p \end{pmatrix},$$

– for the final-state particles:

$$k' = \begin{pmatrix} E'_e \\ E'_e \sin\theta'_e \cos\phi'_e \\ E'_e \sin\theta'_e \sin\phi'_e \\ E'_e \cos\theta'_e \end{pmatrix}, \quad P' = \begin{pmatrix} E'_p \\ P'_{X,p} \\ P'_{Y,p} \\ P'_{Z,p} \end{pmatrix},$$

$$g' = \begin{pmatrix} E'_\gamma \\ E'_\gamma \sin\theta'_\gamma \cos\phi'_\gamma \\ E'_\gamma \sin\theta'_\gamma \sin\phi'_\gamma \\ E'_\gamma \cos\theta'_\gamma \end{pmatrix},$$

where E_e and E_p are the initial energies of the incoming electron and the proton, respectively. E'_e, θ'_e and ϕ'_e are the energy, polar and azimuthal angle of the scattered electron. $E'_p, p'_{X,p}, p'_{Y,p}, p'_{Z,p}$ stand for the energy and the momentum of the final-state proton. $E'_\gamma, \theta'_\gamma$ and ϕ'_γ denote the energy, polar and azimuthal angle of the photon. In the kinematic region explored in this thesis the scattered proton is not observed in the detector because it goes downstream the beam pipe. Thus, the detection of the scattered electron and the photon only is taken into account.

5.2 Particle identification and reconstruction in DVCS

For the Q^2 range of this analysis, $Q^2 > 5\,\mathrm{GeV}^2$, and small t, the signature of the DVCS event in the CAL is observation of the electron and a photon. An efficient identification and a correct reconstruction of both is, therefore, crucial. At $t \approx 0$ the momentum conservation forces the transverse momenta of the electron and of the photon to be balanced. Due to the back-to-back topology in the azimuthal angle, both particles are isolated and can easily be identified. The reconstruction of both particles is performed by means of the computer programs called *electron finders*. They analyse energy deposits in the electromagnetic and hadronic CAL cells and identify origin of the electromagnetic and hadronic clusters. Electrons and photons deposit their energy mainly in the EMC section of the CAL and little or no energy is registered in the HAC section. This is a base for the electromagnetic particles[9] identification. Other particle which can yield the similar signal in the CAL is π^0. The difference between pions and electromagnetic particles lies in the shower profile which can be used to distinguish both types of deposits. Electron finders provide not only information about types of particles but also their energies and positions in the detector.

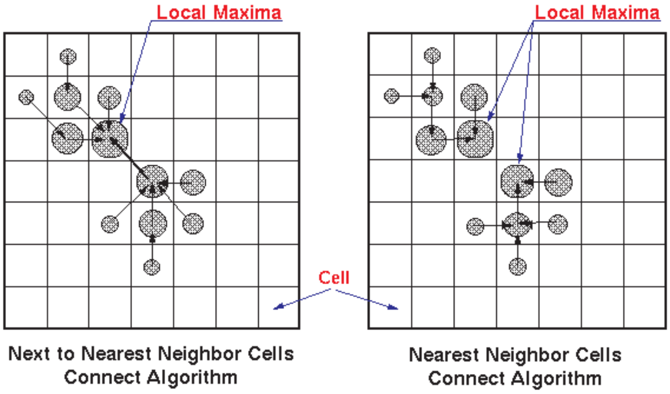

Fig. 31. Schematic representation of the cell island algorithm

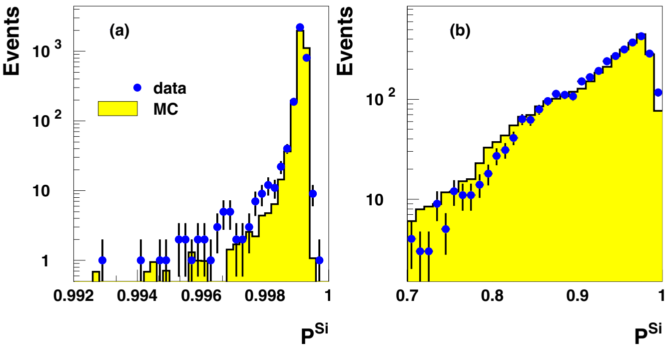

Fig. 32. SINISTRA95 probability for the DVCS final-state particles to be an electron, for **a** electrons and **b** photons

The electron finder used in this analysis is SINISTRA95 [105–107]. It consists of two programs: (i) SIRA95, which searches for electromagnetic deposits in the CAL, and (ii) FINDIS00, which selects the scattered DIS electron among all candidates found by SIRA95 according to assigned selection criteria. In this analysis only the SIRA95 program was used. Due to simplicity of the DVCS final state, DVCS candidates could be selected according to requirements described in Sect. 5.6.

The energy deposits in the CAL are clustered to *islands* according to the cell clustering algorithm. The basic rule of forming an island is that a cell with the highest energy becomes the cluster seed and other neighbouring cells are associated with it. The connections are made to the highest energy neighbour or to the highest energy next to nearest neighbour. This procedure, shown in Fig. 31, is repeated for each cell and produces an unique assignment of a cell to an island.

For each island, the probability P^{Si} that it was produced by an electromagnetic particle is calculated using a neural network algorithm trained with the MC sample [107] of 4000 events. It was found that if the island originates from the scattered electron the probability $P^{\mathrm{Si}} \approx 1$, while for hadrons $P^{\mathrm{Si}} \approx 0$. For a candidate particle to be accepted as an electron, a probability cut of $P^{\mathrm{Si}} > 0.9$ was required, while for a photon the cut $P^{\mathrm{Si}} > 0.7$ was imposed. The first cut is the standard DIS selection for an electron. The latter requirement was tuned with the MC program. Figure 32 shows the P^{Si} distribution for the DVCS final-state particles. For electrons it is clearly peaked at $P^{\mathrm{Si}} \approx 1$ and the MC simulation agrees well with the data. For photons the probability distribution has a peak at high P^{Si} values and a long tail towards lower probabilities. Moreover, at low P^{Si} values the worse agreement between the data and the MC events is observed.

---

[9] Electron and photon are referred to as electromagnetic particles.

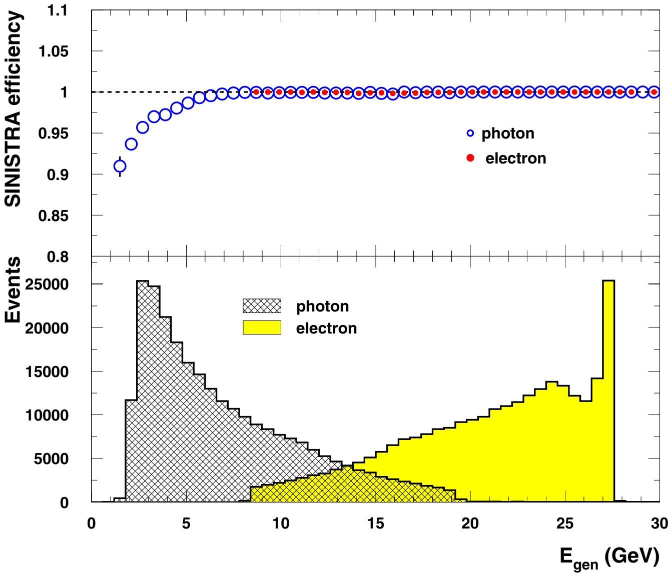

Fig. 33. (Upper) The efficiency of the SINISTRA95 electron finder to find an electron (points) and photon (open circles) candidates as a function of the true particle energy based on the MC simulation. (Lower) Distributions of the true particle energy

In Fig. 33 the efficiency to find an electron or a photon candidate as a function of the true energy is shown. The efficiency was determined with the MC sample of DVCS events generated for $Q^2 > 2.5\,\text{GeV}^2$. For electrons the efficiency is always close to 1, as their energy does not drop below 9 GeV and they always hit the RCAL for which the electron finder was tuned to yield the highest efficiency. The photon efficiency is about 90% at 2 GeV reaching 100% at 7 GeV. At low energies the photon efficiency drops significantly. The final-state particles produce showers in the inactive material in front of the CAL, giving rise to energy deposits similar to hadronic ones, what makes their identification more difficult. In addition, a low energy electromagnetic particles may be faked by electromagnetic showers from $\pi^0 \to \gamma\gamma$ decays or by low energy hadrons from photoproduction events, where the scattered electron escapes down the beam pipe. The particle energy is calculated from the sum of energies over all cells belonging to an island.

The position is calculated by the ELECPO [108–111] package. This algorithm studies the shower profile to properly determine the impact position of the particle. The reconstructed Y coordinate of a cluster is calculated as the weighted average of the cell centre Y_i using weights proportional to the logarithm of the energy deposited in that cell

$$Y = \frac{\sum_{i=1}^{N} w_i \cdot Y_i}{\sum_{i=1}^{N} w_i}, \tag{7}$$

where the weights w_i are given by

$$w_i = \max\left(0, \ln \frac{E_i}{\sum_{j=1}^{N} E_j} + w_0\right), \tag{8}$$

and E_i denotes the energy reconstructed in the i−th cell of the cluster consisting of N fired cells. w_0 is a parameter found to be $w_0 = 2.8$ for both the data and the MC simulation.

For the X coordinate the geometric centres of cells are substituted by a corrected position based on the energy sharing between two sides of each cell and read out by two PMTs. The imbalance between the readout from both PMTs is strongly correlated with the impact position since the light absorption in the scintillator is related to the distance of the lightguide on either side of the cell. The corrected cell position is then combined using the logarithmic weighting of the PMT signals.

For X and Y coordinates resolution of $\sigma_X^{\text{CAL}} = 9\,\text{mm}$ and $\sigma_Y^{\text{CAL}} = 7\,\text{mm}$ was found [91].

5.3 Reconstruction of kinematic variables

Measurement of DVCS cross sections requires a precise determination of the kinematic variables Q^2 and W introduced in Sect. 2.1. Since the four-momenta of the electron and the proton in the initial state are known, the kinematics of DVCS process can be determined from the energy and the polar angle of either the scattered electron or the photon or from any combination of two of these four variables. The uncertainties of the kinematic variables depend on the detector resolution and on the chosen reconstruction method and vary strongly over the phase space.

In the following, the most important reconstruction methods are introduced. They are quoted in terms of y, Q^2 and x.

5.3.1 The electron method

The electron method [112,113] was used first in fixed target experiments. The formulae for kinematic variables are as follows

$$\begin{aligned} y_{\text{el}} &= 1 - \frac{E'_e}{2E_e}(1 - \cos\theta'_e), \\ Q^2_{\text{el}} &= 2E_e E'_e (1 + \cos\theta'_e), \\ x_{\text{el}} &= \frac{E_e}{E_p} \cdot \frac{E'_e(1 + \cos\theta'_e)}{2E_e - E'_e(1 - \cos\theta'_e)}. \end{aligned}$$

It seems to be the simplest method, since it requires only the measurement of the energy E'_e and the polar angle θ'_e of the scattered electron.

The Q^2 resolution in this method is quite good as long as the electromagnetic shower associated with the scattered electron is fully contained in the CAL. In general, the resolution of this variable depends on the resolution of the measurement of the electron polar angle and its energy. Its disadvantages are: a bad x resolution at small y and a large sensitivity to radiative effects. However, the x resolution is very good at large y. As can be seen in Fig. 34 the Q^2_{el} reconstruction is rather precise for large Q^2 values. The reconstruction of W_{el} and x_{el} is poor, mainly at low values of W and x because events tend to migrate from the low W and x range to the higher values of W and x.

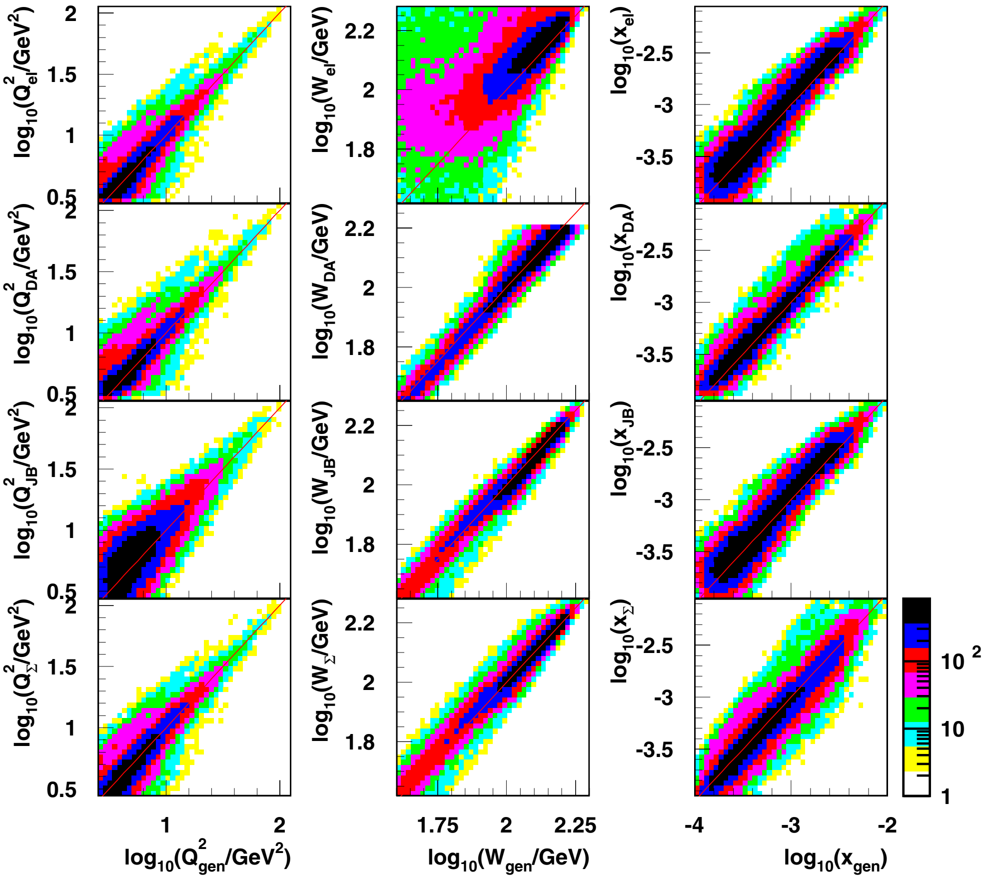

Fig. 34. Reconstructed values of Q^2, W and x compared to the generated values. (From top to bottom) The electron, the double-angle, the Jacquet-Blondel and the $\Sigma-$methods are shown

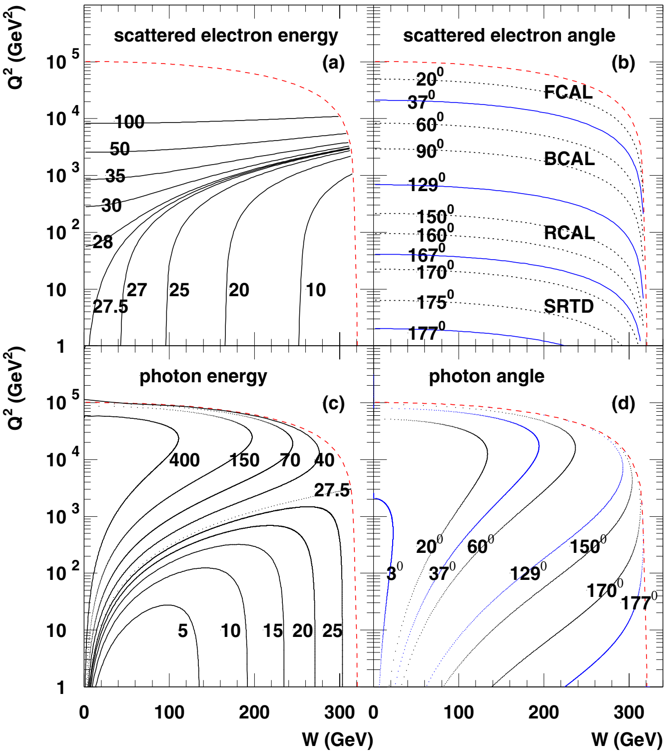

Fig. 35. Isolines of constant scattered electron energy **a**, electron polar angle **b**, photon energy **c** and photon polar angle **d** in the (Q^2, W) plane

Figure 35 shows the dependence of Q^2 and W on the energy and angle of the scattered electron and the photon. In Figs. 35a and b the contours of constant energy E'_e and polar angle θ'_e over the phase space are shown. There is a range of scattered electron energies 27–28 GeV that covers a big region of the kinematic space. A small mismeasurement of E'_e causes a big uncertainty in this area. With respect to the polar angle measurement the big range of the phase space is covered in the vicinity of the RCAL beam pipe. In order to improve the kinematic variable reconstruction the SRTD was installed in this region.

5.3.2 The double-angle method

The double-angle method (DA) [112, 113] relies on the measurement of the electron polar angle θ'_e and the polar angle of the hadronic final state θ'_h. In case of the DVCS process the latter angle is synonymous with the photon angle θ'_γ. This method is motivated by the fact that usually angles are measured with better accuracy than energies. Moreover, this method is almost independent on the energy scale of the CAL[10]. The kinematic variables are given by

$$y_{\mathrm{DA}} = \frac{\sin\theta'_e(1-\cos\theta'_\gamma)}{\sin\theta'_e + \sin\theta'_\gamma - \sin(\theta'_e+\theta'_\gamma)},$$

---

[10] Equations (7) and (8) show that the reconstructed impact position of a particle, which is further used for the polar angle reconstruction, can depend on the particle energy.

$$Q^2_{\rm DA} = 4E_e^2 \frac{\sin\theta'_\gamma(1+\cos\theta'_e)}{\sin\theta'_e + \sin\theta'_\gamma - \sin(\theta'_e+\theta'_\gamma)},$$

$$x_{\rm DA} = \frac{E_e}{E_p}\cdot\frac{\sin\theta'_e + \sin\theta'_\gamma + \sin(\theta'_e+\theta'_\gamma)}{\sin\theta'_e + \sin\theta'_\gamma - \sin(\theta'_e+\theta'_\gamma)}.$$

The DA method has a very good resolution (see Fig. 34), although not perfect because events in the high $W_{\rm DA}$ region and in the whole range of $x_{\rm DA}$ tend to migrate to higher reconstructed values.

5.3.3 The Jacquet-Blondel method

The Jacquet-Blondel method (JB) [114] relies entirely on the detection of the hadronic system. In case of the DVCS process when the proton goes downstream the beam pipe the measurement of hadronic final state is synonymous with the measurement of the photon. This method is based on the assumption that the total transverse momentum carried by hadrons which are undetected in the proton beam pipe as well as the energy carried by particles escaping in the electron direction are negligible. The JB method yields

$$y_{\rm JB} = \frac{E'_\gamma(1-\cos\theta'_\gamma)}{2E_e},$$

$$Q^2_{\rm JB} = \frac{2E_e(E'_\gamma\sin\theta'_\gamma)^2}{2E_e - E'_\gamma(1-\cos\theta'_\gamma)},$$

$$x_{\rm JB} = \frac{Q^2_{JB}}{sy_{JB}}.$$

The resolution of $W_{\rm JB}$ at low values of W is superior to the electron method while the $Q^2_{\rm JB}$ and $x_{\rm JB}$ reconstruction is poor mainly for low Q^2 and x values as shown in Fig. 34.

5.3.4 The $\Sigma-$method

The $\Sigma-$method [115] makes use of the longitudinal momentum conservation $E - p_Z = 2E_e$, where E and p_Z are the total energy and momentum in the Z direction summed up over the whole CAL, respectively. So far it was assumed that momenta of the beam particles in the interaction are known. This is not valid whenever the QED radiation takes place which is possible either from the initial state of the electron (ISR) or from the scattered-electron line (FSR). FSR events are not a problem since the granularity of the detector is not fine enough to separate the electron and the FSR photon, which is emitted almost collinearly off the electron. In the ISR process the photon of energy $E_\gamma^{\rm ISR}$ is emitted almost collinearly with the incoming electron and escapes detection through the rear beam pipe. As a consequence, the electron energy at the IP is reduced to $\overline{E}_e = E_e - E_\gamma^{\rm ISR}$. For DVCS events which are fully contained in the detector $\Sigma = E'_\gamma(1-\cos\theta'_\gamma) + E'_e(1-\cos\theta'_e)$ is equal to $2E_e$. For ISR events this quantity is reduced to $2(E_e - E_\gamma^{\rm ISR}) = 2\overline{E}_e$. The idea of the $\Sigma-$method is, therefore, to replace $2E_e$ in the JB method by $2\overline{E}_e$. Thus, the kinematic variables are given in the following way

$$y_\Sigma = \frac{E'_\gamma(1-\cos\theta'_\gamma)}{\Sigma},$$

$$Q^2_\Sigma = \frac{(E'_e\sin\theta'_e)^2}{1-y_\Sigma},$$

$$x_\Sigma = \frac{Q^2_\Sigma}{sy_\Sigma}.$$

As one can see in Fig. 34 the resolution of Q^2_Σ and W_Σ is significantly better than for the JB method, while for x results of both methods are comparable.

5.4 Trigger selection

As mentioned in Sect. 3.2.10 the ZEUS experiment uses the three level trigger system to reduce the event rate to a level which can be written to disk. For DVCS events, required triggers are almost entirely based on the requirement of finding two electromagnetic clusters in the CAL. The online selection criteria depicted in the following section were designed to select DVCS events and at the same time to reject as many background events as possible.

This analysis was performed using a trigger selection slot with the identification DIS11 or DST93 which is called the QED-Compton bit. The definition of a slot is the same as for a bit - a specific logic for the event filtering. The DST93 trigger selection slot makes use of slots at the FLT, SLT and TLT. All the trigger levels were working in the same configuration during the whole running period covered in this thesis.

5.4.1 FLT selection

The FLT is a hardware trigger. At this level there are plenty of events and the decision has to be made up very quickly. The most significant slot for this analysis was the FLT62 bit which is called the multielectron bit. All the events used in this analysis had to pass the FLT62 bit. This slot triggers on two or more isolated electromagnetic (EM) clusters, ISOE. The cluster is electromagnetic if more than 90% of its energy is deposited in the EMC. This slot yields a low rate and was not prescaled throughout the entire period of the data taking. The definition of ISOE depends on the region of the location of the EM cluster. If the cluster is located in the RCAL or in the BCAL then the condition $E_{\rm ISOE} > 2\,{\rm GeV}$ is imposed. If it is located in the FCAL, the energy threshold depends on the impact position in the FCAL ring[11]: in the first ring is infinite, in the second ring $E_{\rm ISOE} > 20\,{\rm GeV}$, in the third ring $E_{\rm ISOE} > 10\,{\rm GeV}$ and outside the third inner ring $E_{\rm ISOE} > 5\,{\rm GeV}$.

---

[11] The first towers of cells around the beam pipe are defined as the first FCAL ring. The second and third towers of cells form the second and third FCAL rings, respectively.

Due to the specific definition of the FLT62 the efficiency of this slot strongly depends on the energy of a less energetic cluster. This effect was studied in this analysis and is described in Sect. 6.2.8.

5.4.2 SLT selection

On the basis of the FLT62 bit a more detailed trigger selection was carried out at the SLT stage. At this level the full CAL information is available in terms of energy deposits and timing.

The SLT selection makes use of the SLT05 slot which is devoted to the QED-Compton study. At this stage more accurate clustering algorithms are performed. The cuts on energy of the EM cluster are more restrictive depending on the impact position of a particle. If the cluster is located in the RCAL or in the BCAL then the condition imposed is $E^{\mathrm{RCAL,BCAL}} > 2\,\mathrm{GeV}$, while for the FCAL the threshold is $E^{\mathrm{FCAL}} > 10\,\mathrm{GeV}$. This high energy cut in the FCAL takes into account possibility of a detection of particles coming from the dissociation of the proton.

Beam-beam interactions can be distinguished from the beam-gas background thanks to the calorimeter timing. This is possible due to the fact that *ep* interactions take place within the vertex region of the detector during time interval defined by the bunches traversing the centre of the ZEUS detector contrary to the proton-gas interactions in the beam pipe. The clock starts at 0 ns when the bunch crossing takes place at the IP. The distances of the FCAL and RCAL from the IP are 220 cm and 150 cm, respectively, where the distance of 30 cm corresponds to time of 1 ns. This allows to use the timing information of the different CAL sections for rejection of the background. The event is retained when all the following conditions are fulfilled:

- $t_{\mathrm{FCAL}} < 8\,\mathrm{ns}$,
- $t_{\mathrm{RCAL}} > -8\,\mathrm{ns}$,
- $t_{\mathrm{FCAL}} - t_{\mathrm{RCAL}} < 8\,\mathrm{ns}$,
- $t_{\mathrm{Up}} - t_{\mathrm{Down}} > -10\,\mathrm{ns}$,

where t_{FCAL} and t_{RCAL} are the timing for the FCAL and the RCAL, respectively. t_{Up} and t_{Down} stand for the timing of the upper and lower half of the BCAL. Three timing cuts for the RCAL and FCAL remove upstream and downstream interactions of protons with residual gas in the beam pipe. The relative timing cut, $t_{\mathrm{Up}} - t_{\mathrm{Down}}$, is used to remove cosmic muons. As they mostly come from above, they hit the upper BCAL approximately 12 ns earlier than the lower BCAL.

Furthermore, events are vetoed at the SLT when one of the following conditions holds:

- $E - p_Z + 2 \cdot E_{\mathrm{LUMI}\gamma} < 30\,\mathrm{GeV}$,
- $E - p_Z > 100\,\mathrm{GeV}$,

where E and p_Z are the energy and the longitudinal momentum of the event assuming a nominal vertex position at $X_{\mathrm{vtx}} = Y_{\mathrm{vtx}} = Z_{\mathrm{vtx}} = 0$, and $E_{\mathrm{LUMI}\gamma}$ denotes the energy measured in the LUMIγ calorimeter. This condition is formulated in a way to retain ISR events in which the incoming electron radiates a photon in the backward direction of the CAL.

Moreover, sparks are rejected at the SLT stage. Each CAL cell is read out by two PMTs. A high PMT imbalance suggests that most of the energy deposited in the cell was sampled by only one PMT, while a low imbalance means that both PMTs sampled the same amount of energy. A very high imbalance which can be caused by a self-maintained discharge, is a signature of *sparks*. Sparks are suppressed by removing single isolated cells with the imbalance above the certain threshold.

5.4.3 TLT selection

At the TLT stage, more time is available to make up a decision and a software trigger is used. Therefore, more refined electron finder algorithms for an electron identification can select the events. The logical definition of the TLT for DVCS events can be described in the following way, assuming the logical AND between all the conditions:

- number of hadronic islands with energy greater that 2 GeV is equal to 0,
- two EM islands,
- one EM island with energy greater than 4 GeV,
- another EM island with energy greater than 2 GeV,
- HAC0 islands are considered as EM ones,
- energy associated to the FCAL first ring is less than 50 GeV,
- difference of azimuthal angles for islands is greater than $\pi/2$ radians,
- $E - p_Z > 30\,\mathrm{GeV}$, where both quantities are calculated using the CTD tracks if they are available or CAL deposits are used otherwise.

The definition of an island is based on a clustering algorithm (see Sect. 5.2) which aims to merge cells in the CAL belonging to the shower of a single particle.

In addition, the characteristic patterns of hit cells for cosmic muons and for muons which travel in the proton beam-halo are used at the TLT to reject these backgrounds. Moreover, tighter timing cuts comparing to the SLT selection as well as special algorithms [116] to reject beam-halo are applied.

It can be noticed that the TLT trigger used in the DVCS analysis basically does not depend on the tracking information and is predominantly a calorimeter trigger.

Table 2 contains number of events which passed the DST93 bit selection for the analysed data samples and were written to tape. For these events the offline analysis was performed.

Table 2. Number of events which passed the DST93 bit selection

Running period	Beams	Number of events passing the DST93 bit
1996–1997	e^+p	912893
1998–1999	e^-p	322731
1999–2000	e^+p	1398816

5.5 Offline preselection

The event sample obtained with the online trigger selection still contains some contamination from non-*ep* interactions and from non-DVCS *ep* interactions which have to be removed. Before applying cuts on quantities based on calorimeter energy and position values, some corrections were implemented which are described in this section.

The present analysis was performed using the ORANGE program [19]. All the data had to pass the EVTAKE subroutine, which contains the result of data quality tests performed during and after the data taking. Moreover, noise suppression NOISE96S [117] subroutine was applied for each event to reduce the noise level and sparks in the CAL and RCALCORR to correct energy deposits in cells on the energy-scale effect. The first subroutine removes all cells with an energy below a threshold which is 60 (140) MeV for the EMC (HAC) cells. Cells that are also fired in all events of a run are considered as noisy cells and their deposits are not taken into account. After all noisy cells are removed, all the EMC deposits in the RCAL cells are scaled up or down according to [99]. The average correction for RCAL is roughly 2.2%, while the overall correction for all EMC deposits in the BCAL is 5%.

As for the position and energy corrections in the RCAL (see Sect. 4.6), the SRTD, the RHES and the RPRES deposits were used, it was required that only good SRTD, RHES and RPRES runs were taken into account in the final analysis. Since in the 98–00 running period the SRTD had a lot of dead and noisy channels, for the final selection only runs with number of dead channels less than 10 were taken into account. The MC simulation was corrected for this effect (see Fig. 36). Moreover, only runs with a reasonable signal in the presampler were used in the final sample. Table 3 contains the numbers of runs which were excluded from the analysis due to the presampler problems.

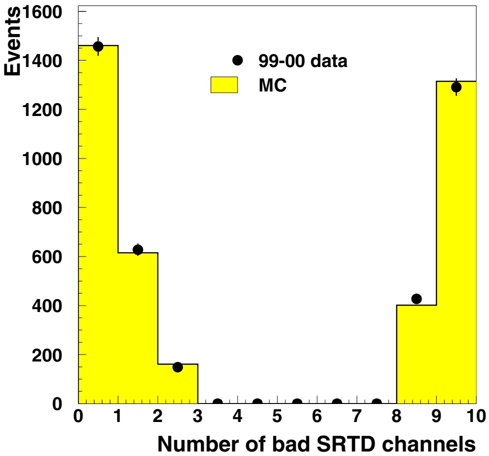

Fig. 36. Comparison of number of dead SRTD channels for the 99–00 e^+p data (dots) and the MC simulation (histograms). Only statistical uncertainties are shown

Table 3. Run ranges excluded from the analysis due to the presampler problems

Year	Run range	Integrated luminosity (pb^{-1})	Note
1996	21259–21690	1.6	RCAL-south top off
1998	31153–31165	0.02	whole presampler off
2000	35933–36098	2.0	several channels affected

Moreover, all the shifted-vertex runs[12] were not taken into account to the final selection.

5.6 Final selection

For the kinematic range of this analysis, the signature of elastic DVCS and BH events consists of a photon and a scattered electron with balanced transverse momenta.

The final selection was based on the two isolated EM clusters in the EMC: the EM1 in the RCAL and the EM2 either in the BCAL or in the RCAL. The EM1 and EM2 clusters belong to a scattered electron and a photon. In order to identify elastic events, there should be no additional signal in the CAL above the noise level. The following selection criteria were applied:

- EM1 in the RCAL with energy $E_1 > 15\,\mathrm{GeV}$ and EM2 with polar angle $0.6 < \theta_2 < 2.75\,\mathrm{rad}$ $(1.2 > \eta_2 > -1.6)$, either in the RCAL with energy $E_2 > 3\,\mathrm{GeV}$, or in the BCAL with energy $E_2 > 2.5\,\mathrm{GeV}$. The angular range of the EM2 corresponds to the region of high efficiency for track reconstruction in the CTD.
- At most one track in the CTD. If a track was found, it was required to match one of the EM clusters and be well reconstructed, i.e. its *distance of the closest approach*[13] (DCA) had to be less than 20 cm, and at least three superlayers crossed in the CTD.
- The probabilities P_1^{Si} and P_2^{Si} of being a scattered electron for the EM1 and EM2 clusters were required to be greater than 0.9 and 0.7, respectively. These variables are calculated by the SINISTRA95 electron finder.
- $40 < E - p_Z < 70$ GeV, where E is the total energy and p_Z the sum of $E\cos\theta$ over the whole CAL. This requirement rejects photoproduction events and beam-gas background. In contrast to the cut on the trigger level the energy in the LUMIγ calorimeter is not included here. Therefore, this cut also rejects events, where photons radiated from the incoming electrons carry an energy of $E_\gamma^{\mathrm{ISR}} \gtrsim (2E_e - 40\,\mathrm{GeV})/2 = 7.5\,\mathrm{GeV}$.
- Total energy deposited in the FCAL had to be less than 1 GeV to suppress the proton-dissociative events.
- Energy in the hadronic part of the BCAL should be less than 1 GeV to ensure that clusters are electromagnetic and, therefore, suppress background from hadrons.

---

[12] In the 2000 running period, run numbers between 37588 and 37639 were taken with a shifted vertex position with respect to the nominal IP.

[13] Distance of the closest approach is a distance of the cluster from the CTD track extrapolation.

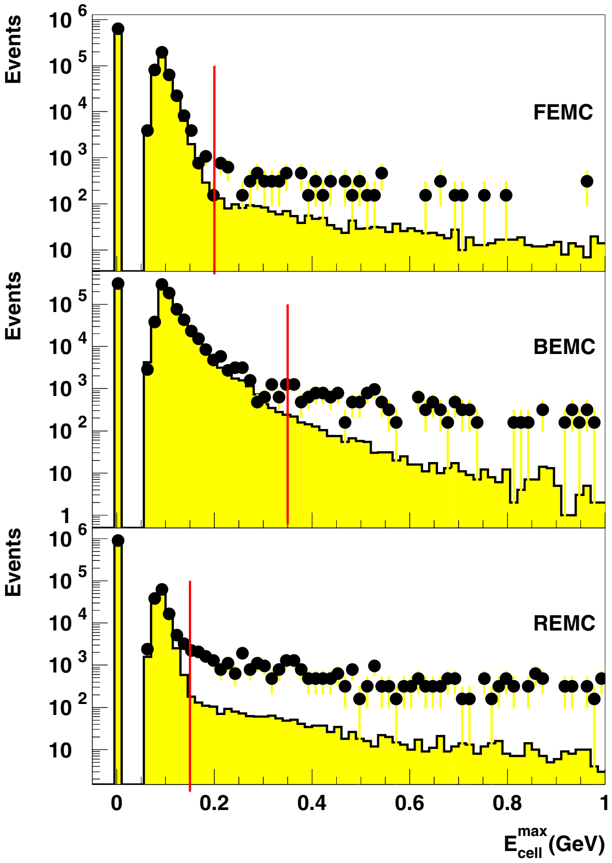

Fig. 37. Maximum cell energy not associated to the EM1 and EM2 clusters for the FEMC, BEMC and REMC sections. The 99–00 data sample (dots) is normalised to random-trigger events (histogram) up to 130 MeV. The straight line shows the applied cut

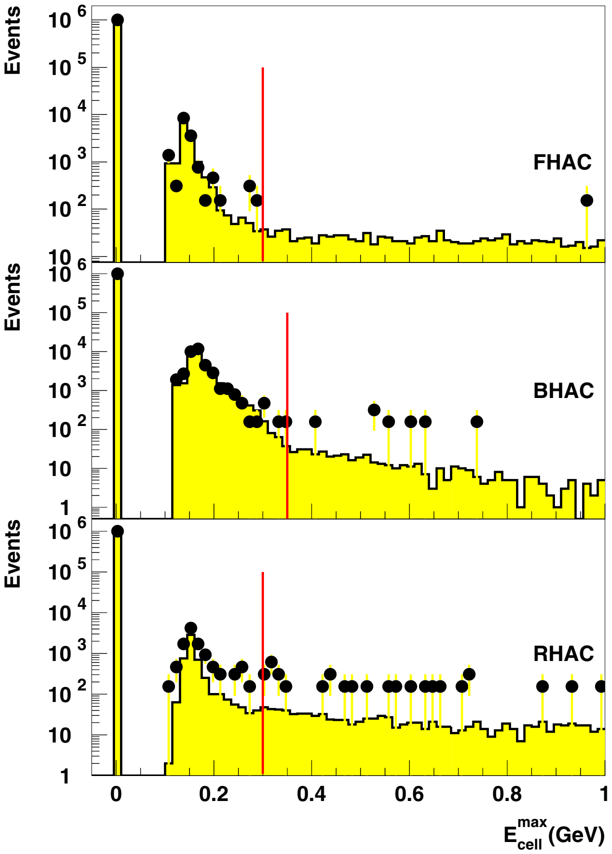

Fig. 38. Maximum cell energy not associated to the EM1 and EM2 clusters for the FHAC, BHAC and RHAC sections. The 99–00 data sample (dots) is normalised to random-trigger events (histogram) up to 150 MeV. The straight line shows the applied cut

- Calorimeter cells not associated with the two EM clusters in the CAL were required to have energy less than: 150 (200) MeV in the FEMC and 200 (300) MeV in the FHAC; 200 (350) MeV in the BEMC and 250 (350) MeV in the BHAC; 150 (150) MeV in the REMC and 300 (300) MeV in the RHAC for the 96–97 (98–00) running period. These thresholds were determined by means of randomly triggered events by requiring that only 0.1% of all events have the maximal cell energy above the threshold. Figures 37 and 38 show the distributions of the maximal cell energy not associated with the EM1 and the EM2 clusters for the random-trigger events and the 99–00 data sample. The latter set was normalised to the random-trigger events up to 130 (150) MeV for the EMC (HAC) sections. This elasticity requirement as well as the next selection criterion rejects most events in which the proton dissociates into a hadronic system.
- For the 98–00 data sample, the energy measured in the FPC was required to be less than 1 GeV.
- All events for which a position of the EM1 cluster (X_1, Y_1) satisfied one of the following conditions

$$(X_1, Y_1) : \begin{cases} |X_1| < 13 \text{ and } |Y_1| < 7 \\ |Y_1| < 11 \text{ and } X_1 < -7 \text{ and } X_1 > -14 \\ |Y_1| < 11 \text{ and } X_1 < 13 \text{ and } X_1 > 4 \end{cases}$$

  were rejected.

  In the RCAL region close to the beam hole the reconstruction of the energy and impact position of the electron is affected by energy leakage into the beam hole. In order to ensure an accurate reconstruction of the EM1 cluster an above cut on its impact position at the RCAL surface was applied. It ensures a minimum distance to the edge of the RCAL hole of about 4 cm.
- Calorimeter cracks cut was applied. Due to the poor MC simulation of the energy leakage in the crack region between the north and the south halves of the RCAL, the regions $|X - 10.0| < 2.5$ and $|X + 10.0| < 2.5$ were excluded from the present analysis. Figure 39 shows the coverage of the $X - Y$ plane of the RCAL for the data and the MC simulation normalised to the same number of events. One can see that the MC generator does not reproduce the lower number of hits in the region of the cracks at $X = \pm 10$ cm. Another reason to reject these regions is the loss of efficiency of the electron finders in the cracks. Moreover, neither the SRTD nor the RHES fully cover the crack region which results in the poor reconstruction of the impact position.
- The position of the EM1 cluster (X_1, Y_1) was required to be found in the RCAL outside the following four regions

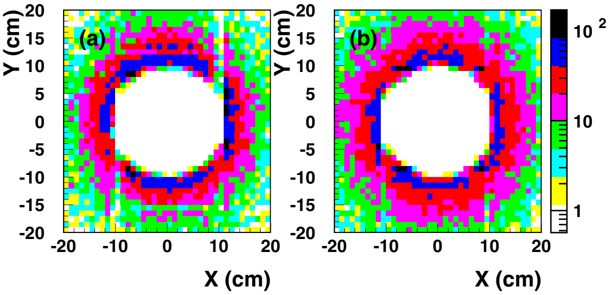

Fig. 39. Coverage of the $X-Y$ plane in the RCAL for **a** the data and **b** the MC-simulation events

$$(X_1,Y_1):\begin{cases}-16<X_1<-7 \text{ and } 4<Y_1<12\\ 3<X_1<12 \quad\text{ and } 4<Y_1<12\\ -16<X_1<-7 \text{ and } -4<Y_1<-12\\ 3<X_1<12 \quad\text{ and } -4<Y_1<-12.\end{cases}$$

The average signal in the SRTD is approximately proportional to the amount of inactive material in front of the RCAL. It was shown [91] that the amount of the dead material is substantially higher in four regions close to the corners of the RCAL beam hole. Moreover, the exact position and the amount of inactive material differs between the data and the MC simulation. Thus, it was decided to reject from this analysis events with hits in these regions.

After applying the above cuts, a total of 18627 events remains in the sample.

For the purpose of this analysis, the values of Q^2 and W were determined for each event, independently of its topology, under the assumption that the EM1 cluster is the scattered electron. This assumption is always valid for DVCS events in the Q^2 range considered here. The value of Q^2 was calculated using the electron method, while W was determined using the double-angle method. No explicit cut on t was applied in the event selection. Events for which $40 < W < 140$ GeV and $5 < Q^2 < 100$ GeV^2 were retained. A total of 11291 events remained in the final data sample. Figure 40 shows the coverage of the $W-Q^2$ plane by the events after applying the final-selection criteria before the kinematic cuts on W and Q^2 were applied. The regions excluded from analysis are also depicted by the lines.

5.7 Analysis strategy

All the remaining events were subdivided into three samples defined as follows:

- γ **sample**: EM2, with no track pointing to it, is the photon candidate and EM1 is the scattered-electron candidate. Both BH and DVCS processes contribute to this topology. The sample consisted of 3945 events. Figure 41 shows calorimeter deposits for an event classified as belonging to the γ sample.
- e **sample**: EM2, with the right-charge track pointing to it, is the scattered-electron candidate and EM1 is the photon candidate. This sample is dominated by the BH process. The contribution from DVCS is predicted to be negligible, due to the large Q^2 required for a large electron scattering angle. This sample contained 7059 events.
- **wrong-sign-**e **sample**: EM2, with the wrong-charge-sign track pointing to it, may have originated from the e^+e^- final state accompanying the scattered electron, where one of the right-sign electrons escaped detection. This background sample is due to non-resonant e^+e^- production and to J/ψ production with a subsequent decay. Other sources are negligible, as will be discussed later. This sample consisted of 287 events.

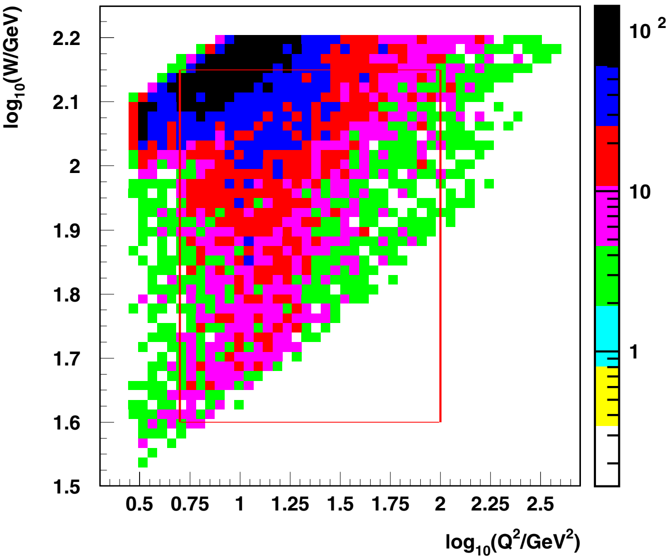

Fig. 40. Coverage of the $W-Q^2$ plane by events after the final selection. Lines indicate the kinematic cut applied

The wrong-sign-e sample was used to subtract the background contributions to the e sample in each kinematic bin. The background-subtracted e sample was then used to investigate the BH contribution to the γ sample.

6 Monte Carlo simulation

Most of the high-energy physics quantities cannot be calculated analytically but need to be simulated using Monte Carlo (MC) techniques. An accurate simulation of physics processes and response of the experiment is vital in any analysis to understand first of all the acceptance of the detector and the trigger efficiency by comparing the number of originally generated events with the number of detected ones. In order to determine the resolution of measured variables one has to compare the reconstructed value with the generated one by means of the MC generator. Moreover, the MC program is indispensable to test physics models by comparing the generated distributions with the ones observed in the data and further to extract model and detector independent results to compare with other experiments or theoretical calculations. In order to check a measurement for systematic uncertainties by adjusting the input distributions to the detector simulation, the MC programs are also necessary. Finally the MC generators are helpful for various background studies.

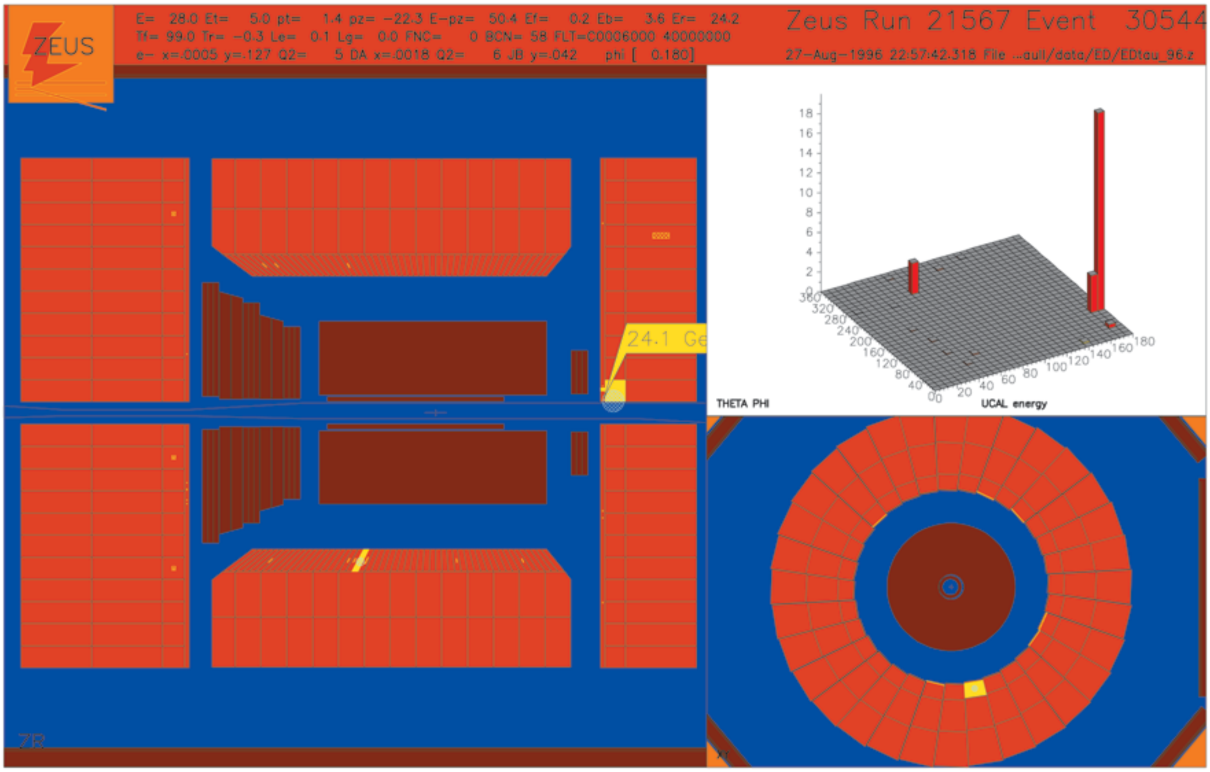

Fig. 41. DVCS candidate as seen by the ZEUS detector

In the following, the stages of the MC simulation in the ZEUS experiment are sketched. Several MC generators for the cross-section calculation and background studies used in this analysis are described. Moreover, in the second part of this section, the MC studies concerning resolution of the kinematic variables, trigger efficiency and determination of the calorimeter energy scale are presented.

6.1 Steps of the MC simulation in ZEUS

The simulation of physics events in ZEUS is performed in two steps. In the first step, the *ep* scattering process is simulated by means of a MC generator. It provides the four-momenta of all the particles involved in the interaction: incoming, intermediate and final-state particles, as well as their types and the production vertices. In the second step, a simulation of the detector response and trigger to the outgoing particles are simulated. MOZART [118] (MOnte carlo for Zeus Analysis, Reconstruction and Trigger) is a program which performs the full simulation of the ZEUS detector. It is based on the GEANT [119] package, which takes into account the geometry and materials of all detector components, as well as the magnetic field in the CTD. It incorporates the present understanding of the detector accumulated from test-beam results and current physics analyses. The three level trigger decision, which is based on the detector signals, is simulated with the ZGANA [120] package (Zeus Geant ANAlysis). The simulated detector responses of all its components are stored in the same ADAMO tables as the physics data and thus they can be processed by means of the same event reconstruction program ZEPHYR and offline analysis code.

Since the proton-beam energy and electron-beam charge were changed during the data taking periods covered in this study, the three independent MC samples were generated to take into account these changes.

6.2 Monte Carlo generators

In order to extract the DVCS cross section from the measured event rate, several MC programs were used. First of all the MC samples for the DVCS process were generated by means of the GenDVCS program. They served for the signal extraction, as well as for the study of the resolution of measured quantities and acceptance corrections. Moreover, in order to distinguish between the DVCS signal and background processes, which can have the same signature in the detector, several other MC programs were also used.

In the following, the main concepts of the MC generators used in this analysis and their implementation in software packages are described.

6.2.1 GenDVCS

The MC generator dedicated to the DVCS study is GenDVCS [121]. It was written and developed for the purposes of this analysis. GenDVCS is based on the FFS model (see Sect. 2.5.1) and simulates the elastic DVCS process only. The basic steps of the generation procedure are:

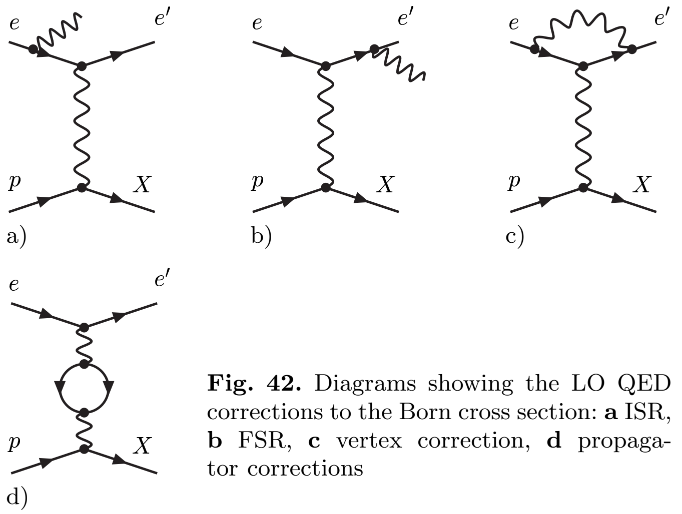

Fig. 42. Diagrams showing the LO QED corrections to the Born cross section: **a** ISR, **b** FSR, **c** vertex correction, **d** propagator corrections

- the four-momenta of the scattered electron and of the photon are generated according to the FFS $\gamma^* p \to \gamma p$ cross section of the form (4).
  The parameterisation ALLM97 [122] of the F_2 structure function of the proton was used as input. In this empirical fit to the $\gamma^* p$ total cross-section data, the Q^2 dependence of ρ was parametrised as $\rho = \frac{\pi}{2}(0.176 + 0.033 \ln Q^2)$ [121].
- the four-momentum of the scattered proton is generated according to the exponential function

$$\frac{d\sigma^{ep}_{\mathrm{DVCS}}}{dt} \propto \exp\left(-b|t|\right).$$

  In GenDVCS b was assumed to be constant and was set to $4.5\,\mathrm{GeV}^{-2}$ over the whole phase space [6]. While this dependence is important for the normalisation of the calculated DVCS cross section, it does not affect the acceptance corrections.
- the generated distribution of the azimuthal angle between the electron and proton scattering planes in the $\gamma^* p$ centre-of-mass system is flat.

Higher order contributions to the Born level cross section of (4) have to be taken into account as they can result in corrections to the observed variables. These corrections originate from the emission of additional real or virtual photon from the electron line. The QED corrections to the Born level process are shown in Figs. 42a–d. In the propagator correction also called the self-energy or vacuum polarisation correction (Fig. 42d), all charged fermions with $m^2 \leq Q^2$ have to be considered. Radiative corrections coming from the proton line are much smaller than the leptonic ones and were neglected.

These QED contributions can not only change the observed cross section but also introduce new types of events, since additional photons can emerge. The radiated photons affect the relation between the kinematics of the $\gamma^* p$ interaction and the measured quantities such as the electron angle and its energy. The size of the effect on the Q^2, W and x reconstruction depends on the reconstruction method. Thus, it is important that these contributions are accounted for in the MC generator. For proper treatment of radiative effects, the GenDVCS generator was interfaced to the HERACLES [123] generator, which includes corrections for initial- and final-state photon emission from the electron line, as well as vertex and propagator corrections.

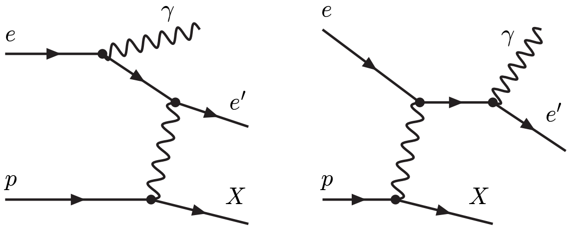

Fig. 43. Diagrams of the BH process

6.2.2 GRAPE-Compton

The elastic and inelastic BH processes, $ep \to e'\gamma p'$ and $ep \to e'\gamma X$, corresponding to the diagrams of Fig. 43, were simulated using the GRAPE-Compton[14] [124] generator.

For the elastic cross-section calculation, the electric and magnetic proton form factors G_E and G_M, respectively, are used in GRAPE. G_E is calculated according to the formula of the dipole fit

$$G_E = \left(1 + \frac{|t|}{0.71\,\mathrm{GeV}^2}\right)^{-2},$$

and G_M is calculated from the relation

$$G_M = \mu_p G_E,$$

where μ_p is the Bohr magneton.

The electromagnetic proton structure functions are parametrised following [125] for $M_X < 2\,\mathrm{GeV}$ (the proton resonance region) and using ALLM97 for $M_X > 2\,\mathrm{GeV}$. These two parameterisations are based on fits to the experimental data of the total $\gamma^* p$ cross sections.

In GRAPE calculation of the proton vertex covers the whole kinematic region divided into three categories of elastic ($M_X = m_p$), quasi-elastic ($|t| < 1\,\mathrm{GeV}^2$ or $m_p + m_{\pi^0} < M_X < 5\,\mathrm{GeV}$) and DIS ($|t| > 1\,\mathrm{GeV}^2$ and $M_X > 5\,\mathrm{GeV}$) processes. Moreover, the ISR and FSR corrections could be included. When the ISR process is turned on, the correction for the photon self energy (the vacuum polarisation) is included according to the parameterisation in [126] by modifying the photon propagator. The FSR corrections are performed by PYTHIA [127] using the parton-shower method. The hadronic final state is generated using the MC event generator SOPHIA [128].

The GRAPE generator gave identical results to the Compton 2.0 [129] generator for the elastic BH process. For the DVCS signal extraction the GRAPE program was used because it also simulates the hadronic final state for the inelastic BH process.

---

[14] Hereafter, the GRAPE-Compton generator is referred to as GRAPE.

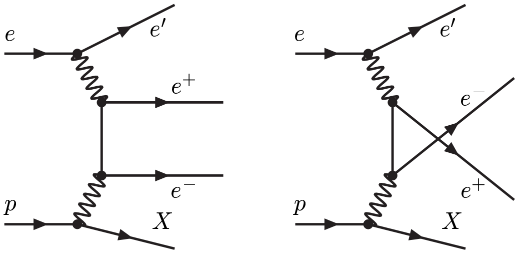

Fig. 44. Feynman diagrams for the process $ep \to e'e^+e^-X$

6.2.3 GRAPE-Dilepton

In the study of the DVCS process, a precise estimation of the dilepton-production background, $ep \to e'e^+e^-X$ (X denotes either the intact proton or its dissociative state) is important, since it forms a background contributing to the e sample. This process was studied by means of the GRAPE-Dilepton [124] generator. In this program a calculation of the cross section is based on Feynman diagrams with virtual $\gamma\gamma, \gamma Z^0, Z^0Z^0$ collisions and a photon conversion into a lepton pair. For the purposes of this analysis only the process of the photon-photon collision, corresponding to the diagrams of Fig. 44 was taken into account. This $\gamma^*\gamma^*$ process was found to be dominant in most of the phase space.

The other rules of the cross-section calculation in GRAPE-Dilepton follows the details for GRAPE described in Sect. 6.2.2.

6.2.4 ZEUSVM

The ZEUSVM [130] program is the generator used to simulate the elastic vector-meson production process $ep \to e'Vp'$ depicted in Fig. 45. ZEUSVM generates kinematic distributions according to basic phenomenological functional relations with a minimum number of free parameters. The Q^2 and W distributions are generated according to the parameterisation of the total $\gamma^*p \to Vp$ cross section

$$\sigma_{\text{tot}}^{\gamma^*p\to Vp}(Q^2, W) \propto \frac{W^\delta}{(M_V^2 + Q^2)^n},$$

where δ and n are parameters and M_V is the vector-meson mass. The four-momentum of the outgoing proton is generated according to the exponential function

$$\frac{d\sigma_{\text{tot}}^{ep\to e'Vp'}}{dt} \propto \exp\left(-b|t|\right).$$

In the generation procedure the parameters δ, n and b were taken from the fit of the resulting cross section of the diffractive production of vector mesons to data. The distributions of the helicity angles were generated flat. Then for proper acceptance corrections the helicity angle distributions were reweighted in a way to preserve s-channel helicity conservation. Moreover, the ZEUSVM program was interfaced to packages for QED radiative corrections based on HERACLES.

The ZEUSVM program was used to simulate the background contributing to the e sample from diffractive J/ψ electroproduction. Moreover, the diffractive production of ρ, ω and ϕ mesons in electroproduction was studied as the potential source of the background in the e sample and in the γ sample (see Sects. 7.1.2, 7.1.4, and 7.2.4).

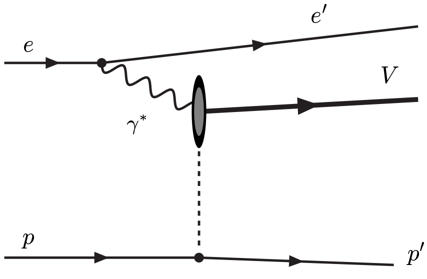

Fig. 45. Diagram of diffractive vector-meson production at HERA

6.2.5 DJANGOH and RAPGAP

In order to study a possible background from low- multiplicity DIS events, additional samples were generated using the diffractive generator RAPGAP [131] and the non-diffractive generator DJANGOH [132].

The non-diffractive ep scattering in DIS, $ep \to e'X$, was simulated by means of the DJANGOH program. The factorisation theorem allows to divide the event generation into several independent steps such as the hard scattering process and the subsequent soft QCD cascades and hadronisation.

In the first step DJANGOH calculates the event kinematics basing on PDF in the framework of the QPM. Moreover, HERACLES includes leading order QED radiative corrections from the electron or quark lines to the Born level cross section. Since the corrections are proportional to the square of the charge, the corrections associated with quarks are smaller than the leptonic ones and usually are incorporated in the PDF.

In the second step QCD cascades are simulated using the colour-dipole model (CDM) implemented in ARIADNE [133]. QCD parton cascade is formed by the gluon radiation and quark-antiquark production, which originate from colour flow between the struck parton and the proton remnant. The boson-gluon fusion (BGF) process, which is particularly important at low values of x, is not described in this program and therefore it is included additionally. The combined code is called CDMBGF.

The process when the coloured partons produced in the QCD cascades form colourless hadrons is not calculable in the perturbative QCD calculations. The hadronisation is therefore described by phenomenological models. The LUND string fragmentation model [134] implemented in JETSET [135] is used.

The RAPGAP generator was used for the simulation of diffractive DIS events, $ep \to e'XN$. It parametrises the inclusive diffractive cross section in terms of the diffractive

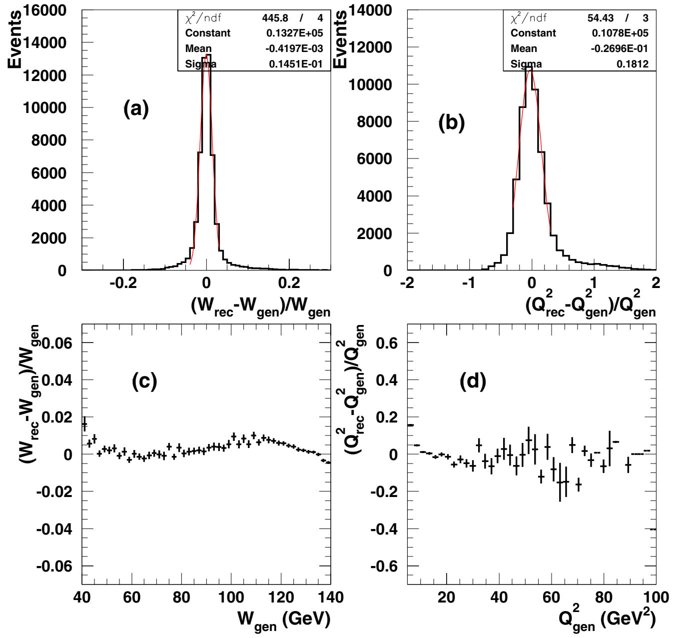

Fig. 46. Resolution of the kinematic variables W **a** and Q^2 **b** with the Gaussian fit imposed. Resolution of W as a function of W_{gen} **c** and Q^2 as a function of Q^2_{gen} **d**

structure function $F_2^{D(4)}(x, Q^2, x_{\mathbb{P}}, t)$. In order to simulate QED radiative effects RAPGAP is interfaced with HERACLES. QCD cascades are simulated via parton showers as implemented in the LEPTO [136] program or with the CDMBGF model as implemented in ARIADNE. The hadronisation and subsequent decays are performed using the JETSET routines.

6.2.6 Monte Carlo studies

In the following, the results of studies based on the MC samples are described. They concern the resolution of the kinematic variables used to the cross-section calculation, the trigger efficiency estimation and the energy scale of the CAL.

6.2.7 Resolution of the kinematic variables

A study of the resolution of the W and Q^2 quantities was done using the MC sample based on the GenDVCS program by direct comparison of the reconstructed quantities W_{rec} and Q^2_{rec} obtained after the full detector simulation with the generated quantities W_{gen} and Q^2_{gen}.

Figure 46 shows the resolution of the W and Q^2 variables. The mean resolution for the reconstruction of W is 1.5% and it stays almost unchanged for the whole W range, while the mean resolution of Q^2 is 18% and it fluctuates a lot at high-Q^2 values.

6.2.8 Trigger efficiency

Since the definition of the FLT62 slot contains the cut on the cluster energy to be greater than 2 GeV (see Sect. 5.4.1), which is very close to the selection cut $E_2 > 2.5$ GeV or $E_2 > 3$ GeV depending on its position (see Sect. 5.6), the FLT62 trigger efficiency as a function of E_2 has to be compared between the data and the MC simulation. For this measurement the independent triggers were selected. For the 96–97 data set the equivalent triggers were found as the FLT30 and TLT-DIS01 or TLT-DIS03 slots, while for the 98–00 running periods the FLT30 and DST52 or DST53 bits were applied. All the triggers used for the efficiency study are defined for inclusive DIS data and do not have the appropriate low energy cut in their definition. In addition, they were not prescaled during the quoted data periods.

The pure BH-event sample was selected with one track pointing to the BCAL or to the RCAL cluster and at least one isolated EM cluster in the RCAL, satisfying all cuts defined in Sect. 5.6 for the e sample. Additionally more restrictive conditions were imposed on the selection:

- one track originating from a vertex and associated to the low energy cluster,
- Z_{vtx} coordinate of the vertex satisfying $|Z_{\text{vtx}}| < 50$ cm to exclude "satellite bunches" taking part in the interaction,
- $0.5 < p_2 < 10$ GeV, where p_2 is a momentum calculated from the track in the CTD,
- $Q^2 > 4$ GeV^2,
- $dE/dx > 1.2$, where dE/dx is the energy loss in the CTD normalised to dE/dx for pions in the momentum range 0.3–0.4 GeV,
- $0 < Z_{\text{width}} < 0.7$, where Z_{width} is the energy weighted width of the cluster in the Z direction (see Sect. 7.2.2).

For all events N^{tot} selected by means of the final selection criteria excluding the DST93 trigger requirement, cuts defined above and independent triggers (FLT30 and TLT-DIS01 or TLT-DIS03 for 96–97 and FLT30 and DST52 or DST53 for 98–00) and then imposing the FLT62 requirement N^{FLT62}, the following quantity was calculated in bins of E_2

$$\epsilon^{\text{FLT62}} = \frac{N^{\text{FLT62}}}{N^{\text{tot}}},$$

for the data $\epsilon^{\text{FLT62}}_{\text{data}}$ and the GRAPE MC sample $\epsilon^{\text{FLT62}}_{\text{MC}}$ separately. The quantity ϵ^{FLT62} is the FLT62 trigger efficiency.

Figure 47 shows the FLT62 trigger efficiency as a function of E_2 for the three data sets divided on two cases when the cluster is either in the BCAL or in the RCAL. The FLT62 trigger efficiency is significantly below 50% for $E_2 < 2$ GeV and for higher E_2 values it grows up rapidly reaching almost 100% at $E_2 \approx 6$ (5) GeV in the BCAL (RCAL). The data were parametrised be means of the function

$$\epsilon^{\text{FLT62}}(E_2) = 1 - p_1 \cdot \left(\frac{10 - E_2}{8}\right)^{p_2}, \qquad (9)$$

where p_1 and p_2 are free parameters. The result of a fit of the form (9) to the 99–00 data set is imposed in Fig. 47 on all running periods to show differences. The p_1, p_2 parameters differ for the three data sets. For the 96–97 running period the trigger efficiency is in a noticeable way higher than

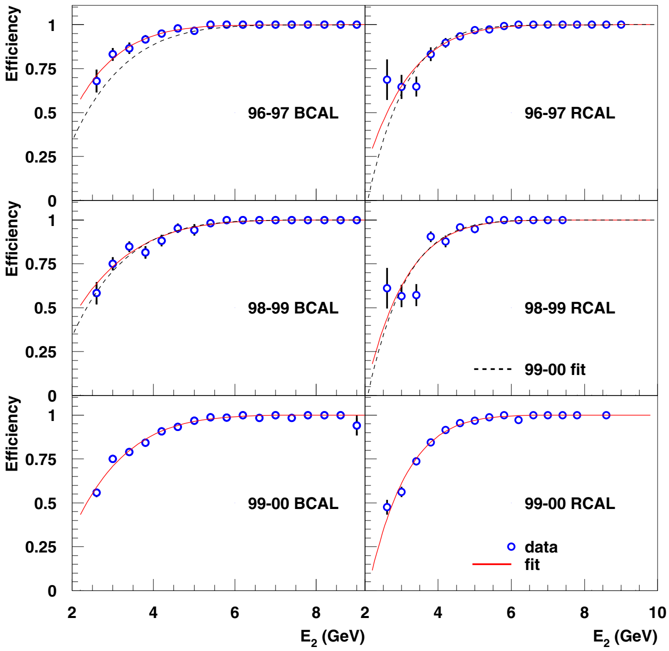

Fig. 47. FLT62 trigger efficiency as a function of E_2 and cluster position being either in the BCAL (left) or in the RCAL (right) for the 96–97, 98–99 and 99–00 running periods for the data. The function of the form (9) is fitted to the three running periods (full line) and a result of the fit for the 99–00 data imposed on the 96–97 and 98–99 sets (dashed line) for the BCAL and the RCAL clusters separately

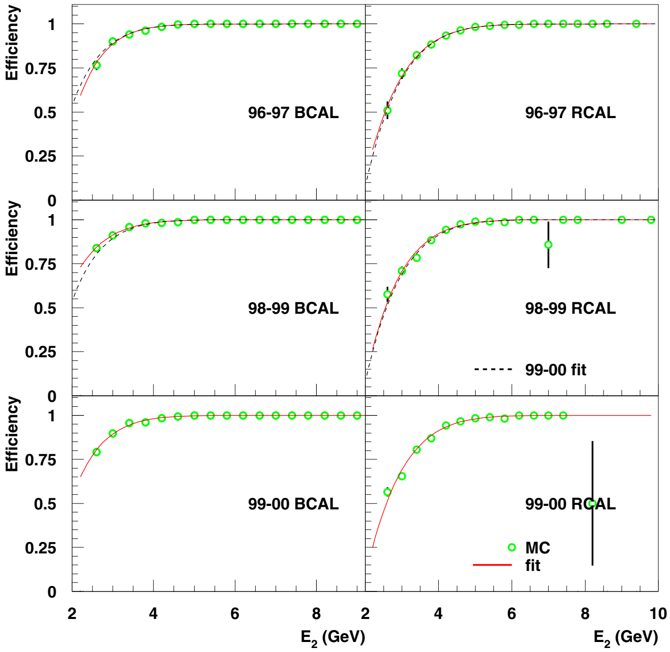

Fig. 48. FLT62 trigger efficiency as a function of E_2 and cluster position being either in the BCAL (left) or in the RCAL (right) for the MC simulation corresponding to three running periods analogous as for the data. The function of the form (9) is fitted to the points (full line) and a result of the fit for the 99–00 running period imposed on the 96–97 and 98–99 sets (dashed line) for the BCAL and the RCAL separately

for subsequent years. It deteriorates mostly for the 99–00 data period. Moreover, for clusters in the BCAL it rises more slowly with E_2 than for the RCAL. The 98–99 and 99–00 data sets seem to exhibit the same behaviour within statistical uncertainties.

The analogous plots for the GRAPE MC simulation are shown in Fig. 48. Again a function of the form (9) was fitted to the points. For the MC sets the FLT62 trigger efficiency is the same for the three running periods when the low energy cluster is in the RCAL, while it differs slightly for the BCAL. This result confirms that the trigger was simulated in the same way during the whole analysed running periods. Moreover, the difference between the FLT62 trigger efficiency shape in the BCAL and the RCAL follows the behaviour of the data.

Finally, the difference between the FLT62 trigger efficiency for the data and the MC simulation was investigated using the weight $we(E_2)$ defined as

$$we(E_2) = \frac{\epsilon^{\mathrm{FLT62}}_{\mathrm{data}}(E_2)}{\epsilon^{\mathrm{FLT62}}_{\mathrm{MC}}(E_2)}.$$

Figure 49 shows $we(E_2)$ for the three running periods, for the BCAL and RCAL clusters separately. One can see that the FLT62 trigger efficiency, neglecting single bins, is higher for the MC simulation. It means that the MC program does not reproduce the real trigger properly and has to be corrected. Also it changes between running periods but within the statistical uncertainty it is the same for the 96–00 sets in the RCAL. In addition, it differs significantly for the clusters in the BCAL for the 96–97 and the 98–00 running periods.

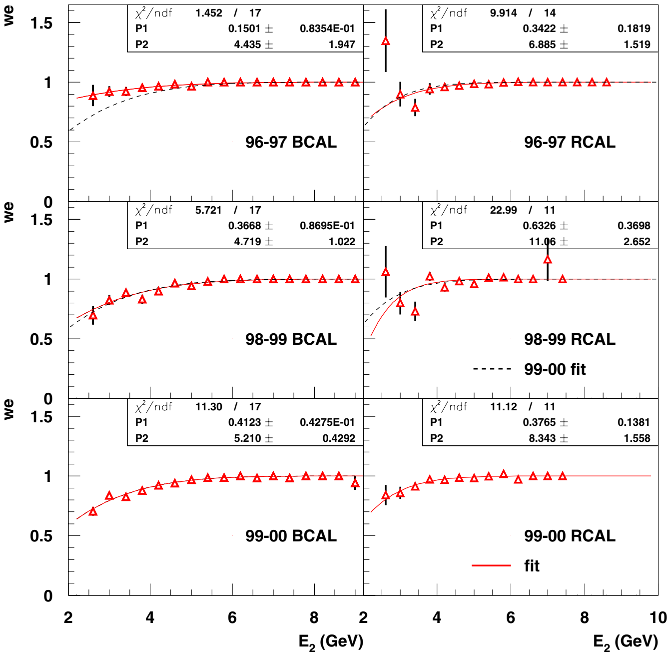

Fig. 49. Weight of the FLT62 trigger efficiency as a function of E_2 and cluster position being either in the BCAL (left) or in the RCAL (right) for the three running periods. Fitted functions imposed as also shown in Fig. 48. Values of the fitted parameters p_1, p_2 are also depicted

As the result of this study all the MC sets used in this analysis were reweighted using $we(E_2)$ on an event-by-event basis. The large deviations from the fitted function, mainly in the low-E_2 bins, were the reason why the bin-by-bin correction factor was applied.

6.2.9 Energy scale

Two methods were used to correct the energy scale for electromagnetic shower leakage in the BCAL and in the RCAL. The first method was based on the comparison of the energy deposited in the CAL and the momentum of the charged particle in the CTD, while the second one used the transverse momentum balance of the final-state particles.

The energy scale was studied by means of the e sample. In this sample the electron track is within the CTD coverage, so is well reconstructed. One can define a quantity

$$R_p = E_2/p_2 - 1,$$

where E_2 is the energy of an electron measured in the CAL and p_2 is the total momentum of the electron measured in the CTD.

Figure 50 depicts the R_p distribution for the 96–97 data and MC events for the electron going either to the BCAL or to the RCAL. The Gaussian function was fitted to the R_p distribution. The same procedure was performed for both the data and the MC simulation. Each fit produces a mean value. If the peak is centred at 0 then the energy scale is equal to 1 and the data do not need to be corrected for. This method provides an absolute energy scale of the response of the CAL in the data independently on the MC generator. Also it provides an absolute determination of the energy scale of the MC simulation. The difference in the absolute energy scales in the data and the MC sample defines the relative energy scale.

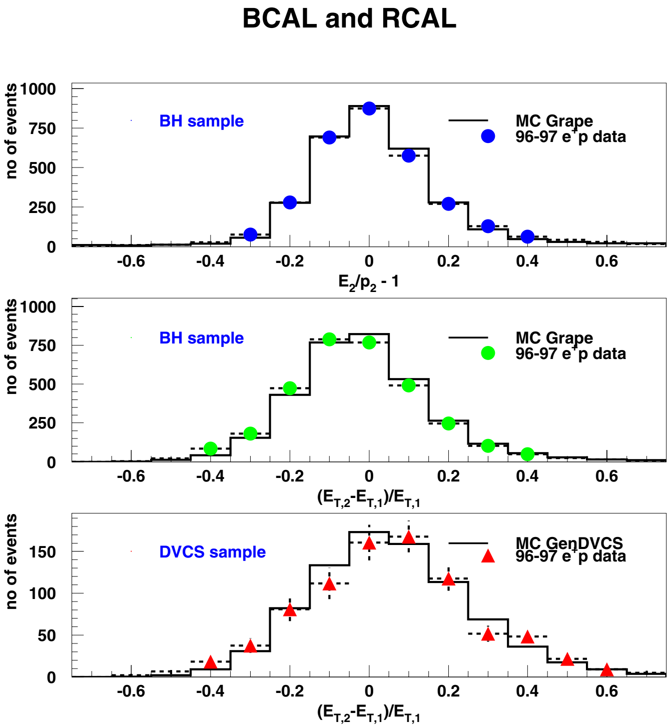

Fig. 50. (Upper) Distribution of $R_p = E_2/p_2 - 1$ for the e sample in the data and in the GRAPE MC simulation. (Middle) Distribution of $R_T = E_{T,2}/E_{T,1} - 1$ for the e sample in the data and in the GRAPE MC simulation. (Lower) Distribution of $E_{T,2}/E_{T,1} - 1$ for the γ sample in the data and in the GenDVCS MC simulation after the background subtraction

The average values of R_p were found as

$$\langle R_p^{\mathrm{data}} \rangle = -0.009 \pm 0.003$$

and

$$\langle R_p^{MC} \rangle = -0.008 \pm 0.002,$$

for the data sample and the MC events, respectively. Only statistical uncertainties are quoted. It is seen that there is no difference in the average values for both sets within statistical uncertainties.

For the absolute and relative energy-scale studies one can also use both clusters present in the e sample. Due to transverse-momentum conservation of the final-state electron and the photon, the distribution of

$$R_T = E_{T,2}/E_{T,1} - 1,$$

should be centred at 0 for the data as well as for the GRAPE MC events, where $E_{T,2} = E_2 \sin\theta_2$ and $E_{T,1} = E_1 \sin\theta_1$ are transverse energy of the electron and the photon, respectively.

Figure 50 shows the distributions of R_T for the e sample. The average values of R_T are

$$\langle R_T^{\mathrm{data}} \rangle = -0.039 \pm 0.004$$

and

$$\langle R_T^{\mathrm{MC}} \rangle = -0.025 \pm 0.002$$

for the e sample in the data and in the MC simulation, respectively. Only statistical uncertainties are quoted. The average R_T values are unequal for the data and the MC events. The previous study [137] also showed a difference. Finally Fig. 50 depicts the R_T distribution for the γ sample after the background subtraction. The DVCS signal is compared to the GenDVCS MC predictions. Again a shift between the data and the GenDVCS prediction is found.

R_p and R_T were studied in bins of p_2, which is the variable giving the best determination of the energy of a charged particle. The e sample was divided into four intervals of p_2 for $2.5 < p_2 < 6.5$ GeV. For each of the intervals, the $\langle R_p \rangle$ and $\langle R_T \rangle$ values were calculated for the data and the GRAPE MC simulation. Figure 51 shows the $\langle R_p \rangle$ values for the data and the MC events and the difference between $\langle R_p^{\mathrm{MC}} \rangle - \langle R_p^{\mathrm{data}} \rangle$. The shift of the absolute energy scale was parametrised by a function

$$R_p^{\mathrm{MC}} - R_p^{\mathrm{data}} = -0.01\ (0.02) + 0.003\ (0.004) \cdot p_2,$$

where numbers in brackets denote statistical uncertainties. One can see that there is no significant difference within the present uncertainties between the data and the MC simulation.

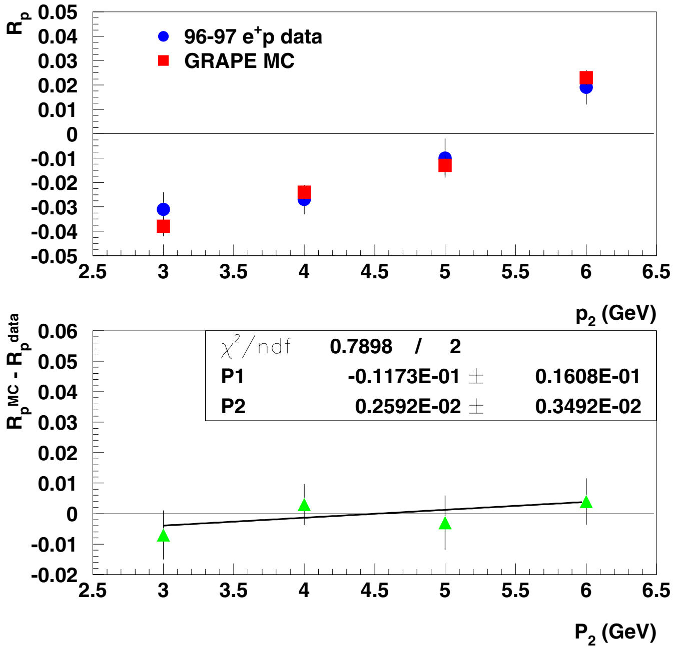

Fig. 51. (Upper) Distribution of R_p as a function of p_2 for the 96–97 data (dots) and the GRAPE MC simulation (squares). (Lower) Difference of R_p for the MC and the data as a function of p_2. The linear fit is imposed on the points. Only statistical uncertainties are depicted

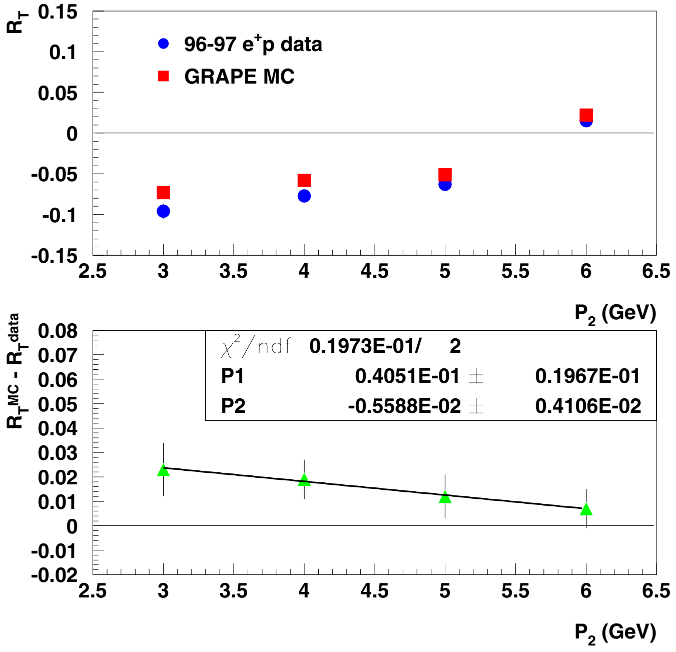

Fig. 52. (Upper) Distribution of R_T as a function of p_2 for the 96–97 data (dots) and the GRAPE MC simulation (squares). (Lower) Difference of R_T for the MC and the data as a function of p_2. The linear fit is imposed on the points. Only statistical uncertainties are depicted

Analogously, Fig. 52 shows the p_2 dependences of $\langle R_T \rangle$ for the e sample in the data and the GRAPE MC simulation and the difference $R_T^{\rm MC} - R_T^{\rm data}$ parametrised as

$$R_T^{\rm MC} - R_T^{\rm data} = 0.04\ (0.02) - 0.006\ (0.005) \cdot p_2 . \qquad (10)$$

In order to correct for the relative energy scale, the energy of the low energy cluster in the data was scaled up according to the formula (10).

The analogous study was performed for the 98–99 and 99–00 data. Results of the corresponding linear fits are

$$R_p^{\rm MC} - R_p^{\rm data} = -0.04\ (0.02) + 0.009\ (0.003) \cdot p_2$$

and

$$R_T^{\rm MC} - R_T^{\rm data} = 0.04\ (0.02) - 0.006\ (0.003) \cdot p_2 , \qquad (11)$$

which follow both investigated data sets. As a consequence, (11) was used to correct the 98–99 and 99–00 data for energy scale.

7 Background study

The selection criteria described earlier were designed to select elastic DVCS events. While being effective for the removal of events with different detector signature and kinematics, the selection cuts may not be able to remove contributions from other processes characterised by similar kinematics and detector response. These contributions have to be evaluated and removed before any quantitative measurement can be extracted from the data. The most important tool for the background estimation is the comparison of the data sample with the MC events.

In the following, the main background sources contributing to the DVCS process are investigated. This is studied for the e sample and the γ sample separately.

7.1 Background in the e sample

In this section, it will be shown that the e sample is dominated mainly by BH events. The proper understanding of components of the e sample will allow one to determine an amount of the BH background for the DVCS process, which enters the γ sample.

Several additional processes can contribute to the same event topology as the elastic BH events in the e sample in a sizeable way: the elastic and inelastic dilepton production in two-photon interactions, the diffractive electroproduction of J/ψ vector mesons and the inelastic BH.

The dilepton and J/ψ production processes were studied using the wrong-sign-e sample, because the both processes have an opposite-charged electron with respect to the electron beam in the final state. Such an electron was used to extract events belonging to the wrong-sign-e sample and then to obtain the estimation of a number of events for the both processes contributing to the e sample.

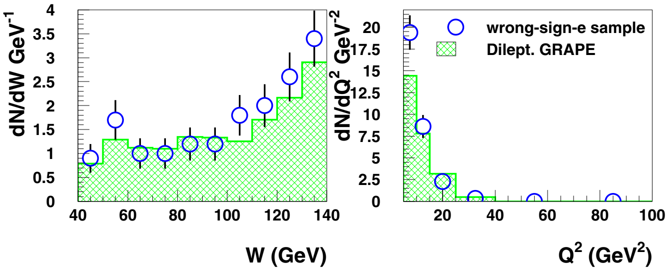

Fig. 53. Distribution of W (left) and Q^2 (right) for the wrong-sign-e sample. The 99–00 data (open circles) are compared to the GRAPE-Dilepton MC expectation (histogram)

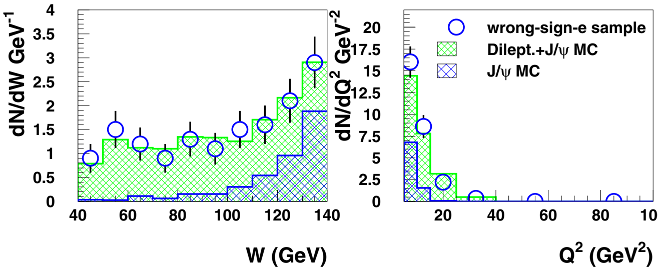

Fig. 54. Distribution of W (left) and Q^2 (right) for the wrong-sign-e sample. The 99–00 data (open circles) are compared to a sum of the dilepton and J/ψ MC expectation (light shaded histogram). The contribution from J/ψ events is also depicted (dark shaded histogram)

7.1.1 Dileptons

Elastic and inelastic dilepton production in two-photon events, $ep \to e'e^+e^-p'$ and $ep \to e'e^+e^-X$, can contribute to the same event topology as the BH events when one of the final-state electrons escapes detection, so only two of them are observed in the CAL. Moreover, if a track associated with one of detected electrons is not measured in the CTD due to a large polar angle, this electron is classified as a photon in the e sample. The second observed electron deposits an energy either in the RCAL or in the BCAL. If the charge of a track is the same as the initial electron, the event is classified to the e sample, otherwise the event is recognised as belonging to the wrong-sign-e sample. The third electron is not seen in the CAL either because an energy deposit is less than the noise level or due to a very small or very large polar angle not being within the CAL coverage.

The dilepton production was studied using events belonging to the wrong-sign-e sample. In Fig. 53 distributions of W and Q^2 are shown for the wrong-sign-e sample representing the data and the MC events. For the MC sample the elastic and inelastic events were mixed up. All events in the wrong-sign-e sample are assumed to come from the dilepton production process. It was found that description of the data is the best for mixture of 70% elastic and of 30% inelastic events. Nevertheless, the excess of events observed in high W and low Q^2 region over the MC expectation, suggests that an additional process can contribute to the wrong-sign-e sample.

7.1.2 J/ψ background

Diffractive elastic J/ψ vector-meson electroproduction $ep \to e'(J/\psi)p'$, with $J/\psi \to e^+e^-$, can yield the same event topology as the e sample, when one of the final-state electrons escapes detection. Moreover, the scattered electron hits the RCAL outside the CTD coverage and only right-charged electron, which comes from the decay of the J/ψ, yields a signal in the BCAL or in the RCAL within the CTD acceptance.

This background was also studied by means of the wrong-sign-e sample. The J/ψ events can contribute to this sample when the opposite-charged electron is detected while the right-charged one escapes detection. In Fig. 54 the wrong-sign-e sample is compared to the sum of two background contributions from the dilepton and J/ψ electroproduction processes. Using the χ^2 minimisation method, it was found that the best description of the data is for 75 (90)% dilepton and 25 (10)% J/ψ events in the 98–00 (96–97) running period.

Due to the pretty good description of the wrong-sign-e sample by the MC simulation, which is the sum of elastic and inelastic dilepton and J/ψ electroproduction processes, these processes were taken as the only background contribution to this sample in the data. Nevertheless, other possible vector-meson contributions, which may also fake both the wrong-sign-e and e samples in the similar way, will also be investigated in Sect. 7.1.4. The MC sample was normalised to the total number of events in the wrong-sign-e sample and then used to statistically subtract the dilepton and J/ψ electroproduction contributions from the e sample. It was found that these contributions together comprise 4.5% of the e sample.

7.1.3 Proton-dissociative BH background

The final selection criteria to extract elastic DVCS events from the data also select a small fraction of inelastic[16] events in which secondary particles of the low-mass hadronic system escape detection in the CAL. This proton- dissociative background arises in the e sample as well as in the γ sample. Two methods to investigate a fraction of inelastic BH events in the data were investigated. Both are based on the fact that the GRAPE MC program can generate the elastic as well the inelastic contributions to both samples. This inelastic component can be used to the proton-dissociative background study. The first method concentrates on the fact that for a clean sample of the elastic BH events one should observe a balance of the transverse momenta of the two final-state particles. It means that the difference of the azimuthal angles $\Delta\phi_{12}$ for these two particles should have a peak around π radians. Any significant deviation from this value reflects mainly the inelastic background. The second method discussed here is based on the measurement of a proton remnant using the PRT1 for the 96–97 running period and the FPC for the 98–00 data. Moreover, as a check

---

[16] Proton-dissociative process is referred to as inelastic.

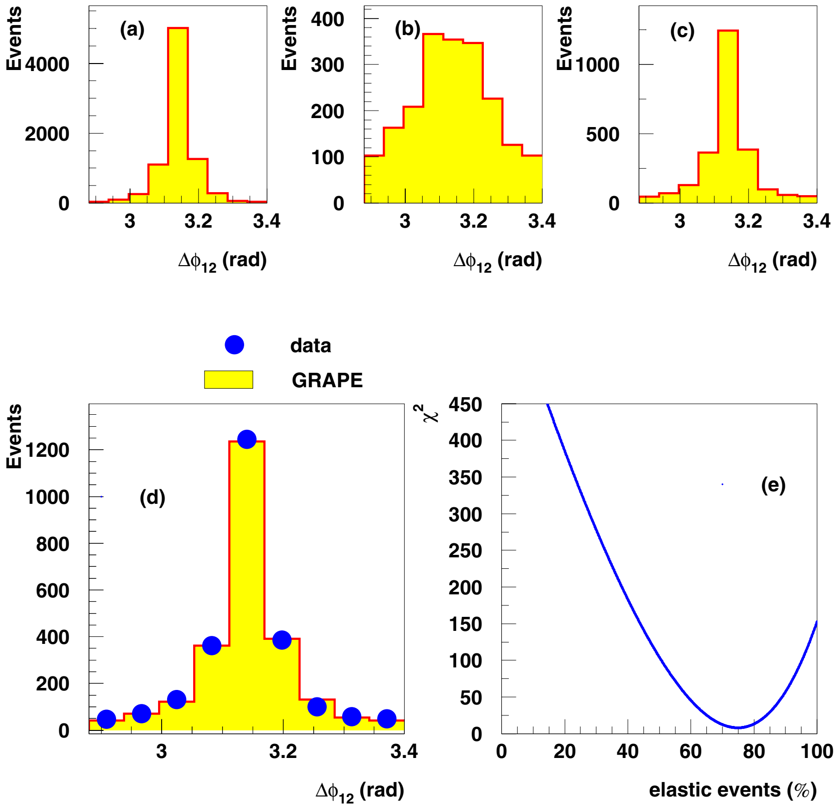

Fig. 55. Distribution of the difference in the azimuthal angle for an electron and a photon $\Delta\phi_{12}$ for the BH process; **a** elastic component of the GRAPE MC sample, **b** inelastic component of GRAPE, **c** the 96–97 data, **d** the comparison of the data (points) with the best mixture of the elastic (75%) and inelastic (25%) MC components (histogram), **e** the χ^2 distribution as a function of the fraction of elastic contribution to the BH process

of the inelastic GRAPE MC program, the FCAL method was used.

$\Delta\phi_{12}$ method

Analysing the data belonging to the e sample, it was found that the difference in the azimuthal angles $\Delta\phi_{12}$ for EM1 and EM2 clusters is not well described by the elastic GRAPE MC component solely. The addition of the inelastic contribution improves the agreement between the data and the GRAPE MC expectation. Figures 55a–c show the $\Delta\phi_{12}$ distribution for the elastic and inelastic GRAPE MC sample and the data, respectively. Mixing up the elastic and inelastic components of the MC events and fitting to the data in order to minimise the χ^2 function (see Fig. 55e), it was found that the best description of the 96–97 data by GRAPE is achieved for $(75 \pm 3)\%$ of the elastic component giving $\chi^2_{\rm min}/ndf = 8.09/8$. Figure 55d depicts the comparison of the $\Delta\phi_{12}$ distribution for the 96–97 data with the best mixture of the elastic and inelastic MC components of the BH process. One can see that mixed GRAPE MC describes the data pretty well.

The same study for the other running periods yields $(75 \pm 4)\%$ of the elastic component with $\chi^2_{\rm min}/ndf = 5.16/8$ for 98–99 and $(71.1 \pm 2.4)\%$ with $\chi^2_{\rm min}/ndf = 27.06/8$ for 99–00. The results are consistent within the three running periods.

PRT1/FPC method

Inelastic events are tagged by the PRT1 when one of the PRT1 counters gives a signal above a threshold. These events are observed in the forward direction with energy above 1 GeV in the FPC, relaxing the elasticity cut. In fact the proton-dissociative events with no energy deposited are experimentally not distinguishable from the elastic ones. Therefore, these two processes have to be separated on a statistical basis using the inelastic GRAPE MC program. Assuming that the non-diffractive background is negligible, the overall fraction $F^{\rm tot}_{\rm pdiss}$ of the proton- dissociative events in the data was calculated as

$$F^{\rm tot}_{\rm pdiss} = \frac{F^{\rm data}_{\rm pdiss}}{F^{\rm GRAPE}_{\rm pdiss}}\,, \tag{12}$$

where $F^{\rm data}_{\rm pdiss}$ and $F^{\rm GRAPE}_{\rm pdiss}$ denote the fractions of tagged proton-dissociative events in the data and in the inelastic GRAPE MC simulation, respectively.

Figures 56a–e show the fractions of the inelastic events tagged by the PRT1 in inelastic GRAPE, in the e sample in the 96–97 data, the total fraction of the proton-dissociative events in the e sample in the data and in the γ sample in Q^2, respectively. For all sets the straight line is fitted to the points. Figures 57a–e show the analogous dependencies in five bins of W. Figures 58–e show the analogous plots as a function of Q^2 for the 99–00 running period and the FPC used and Figs. 59a–e as a function of W. It is observed that $F^{\rm tot}_{\rm pdiss}$ does not depend on neither Q^2 nor W. The inelastic contribution was estimated from the straight-line fit to the e sample in the data corrected according to (12) as fixed and equal to $F^{\rm tot}_{\rm pdiss} = (17.95 \pm 1.10)\%$ for the PRT1 and $F^{\rm tot}_{\rm pdiss} = (11.05 \pm 0.96)\%$ for the FPC. The uncertainties are statistical.

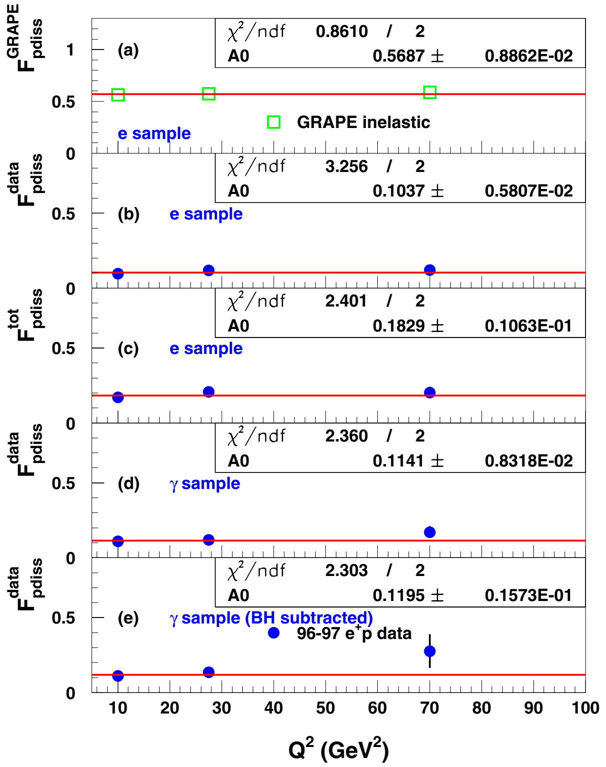

Fig. 56. Fraction of the proton-dissociative events tagged by the PRT1 as a function of Q^2 in the e sample in GRAPE **a**, in the 96–97 data **b**, the data corrected for GRAPE **c**, fraction of inelastic events in the γ sample in the data **d** and in the γ sample in the data after BH background subtraction **e**. The straight-line fit is also shown

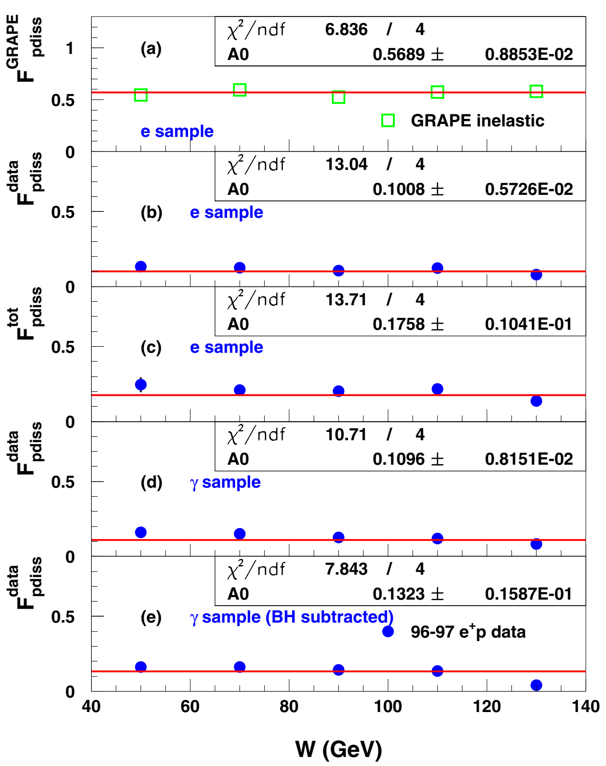

Fig. 57. Fraction of the proton-dissociative events tagged by the PRT1 as a function of W in the e sample in GRAPE, in the 96–97 data **b**, the data corrected for GRAPE **c**, fraction of inelastic events in the γ sample in the data **d** and in the γ sample in the data after BH background subtraction **e**. The straight-line fit is also shown

The fractions of the tagged proton-dissociative background were found for the e sample as

$$F^{\rm data}_{\rm pdiss} = [10.3\ (3.97) \pm 0.6\ (0.33)]\%,$$

and for the γ sample as

$$F^{\rm data}_{\rm pdiss} = [12.6\ (3.77) \pm 1.6\ (0.76)]\%,$$

for the PRT1 (FPC). The fractions are equal for the two samples within the statistical uncertainties.

The PRT1 result $F^{\rm tot}_{\rm pdiss} = (17.95 \pm 1.10)\%$ is consistent with the $\Delta\phi_{12}$ method $F^{\rm tot}_{\rm pdiss} = (25 \pm 3)\%$ within three standard deviations. No attempt was made to quantify the systematic uncertainty because of little sensitivity to the cross section. The difference of the measured fractions of proton-dissociative events is due to the different PRT1 and FPC detector configurations in the two running periods.

FCAL method

Alternatively, as a check for the inelastic GRAPE MC program, the energy deposits in the FCAL towers close to the beam pipe were used for tagging the proton-dissociative events instead of the PRT1 and the FPC. If one relaxes the elasticity cut and allows for any energy deposit above the noise threshold in the FCAL, the observed signal comes mostly from low-mass system resulting from the dissociation of a proton. Figure 60 shows the distribution of the energy flow in the FCAL for events with energy deposits above the noise threshold in the FCAL. The data are compared to the inelastic GRAPE MC expectation. A reasonable agreement suggests that inelastic GRAPE describes the low-mass distribution of the proton dissociation pretty well.

The fractions of inelastic BH events in the e sample, estimated according to the PRT1/FPC method, were taken as nominal in this analysis. A use of mixed GRAPE resulted in a better description of the data in several distributions sensitive to the inelastic component. On the other hand, it was found that this fraction of inelastic BH events has little sensitivity to the cross section (see Sect. 8.6).

The estimation of $F^{\rm tot}_{\rm pdiss}$ in the γ sample was not possible due to a lack of the MC program dedicated to the inelastic DVCS process.

7.1.4 Other contributions

The other sources of background taken into account as a potential contribution to the e sample are:

- diffractive ϕ meson electroproduction ($ep \to e'\phi p'$, $\phi \to \pi^0\pi^+\pi^-$),
- diffractive ω meson electroproduction ($ep \to e'\omega p'$, $\omega \to \pi^0\pi^+\pi^-$),

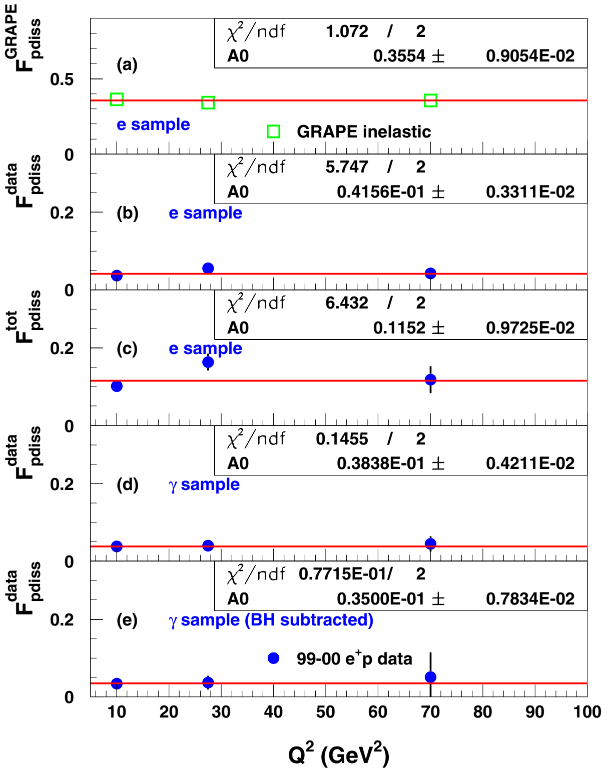

Fig. 58. Fraction of the proton-dissociative events tagged by the FPC as a function of Q^2 in the e sample in GRAPE **a**, in the 99–00 data **b**, the data corrected for GRAPE **c** and fraction of inelastic events in the γ sample in the data **d**. The straight-line fit is also shown

- diffractive ρ meson electroproduction ($ep \to e'\rho p'$, $\rho \to \pi^+\pi^-$).

All the listed processes may also contribute to the wrong-sign-e sample, as they have a particle with an opposite charge with respect to the initial-state electron. Moreover, all of them have charged particles in the final state, which can fake the BH signal in the e sample if only two of the final-state particles give a reasonable deposit in the CAL and the final selection criteria described in Sect. 5.6 are fulfilled.

The detailed study of efficiency of the final selection criteria was performed for each process by means of the ZEUSVM program. The MC simulation shows that the most effective cut to reject the ϕ vector-meson events was found to be a cut of the number of the EM clusters in the CAL. Since the discussed process has more than two particles in the final state, the probability that more than two of them give energy deposits in the CAL is greater than 50%. Moreover, for two-cluster events it is probable (57%) that both are associated to the tracks in the CTD, while for one-track events it is likely (48%) that a track is not well reconstructed. The same study was performed for the remaining vector mesons. Conclusions are the same for ω due to the same final state. The ρ mesons are not seen in the e sample mainly due to the $Q^2 > 5\,\mathrm{GeV}^2$ cut.

The study showed that a contribution from the ϕ, ω and ρ electroproduction to the e sample is below 0.1%, thus it can be neglected. Also this background does not contribute to the wrong-sign-e sample.

Moreover, vector-meson photoproduction processes were studied as a potential contribution to a background for both e and wrong-sign-e samples. It was found that none of events survive final cuts mainly due to the restrictive $E - p_Z$ requirement (see Sect. 5.6).

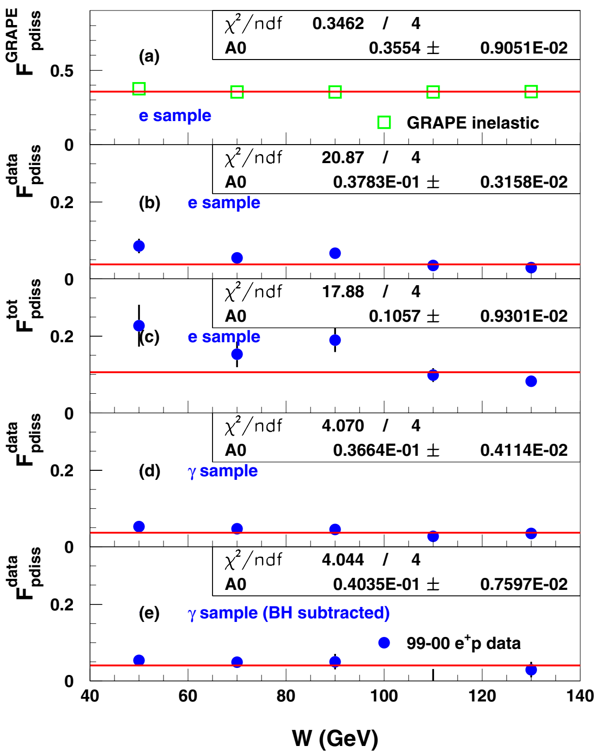

Fig. 59. Fraction of the proton-dissociative events tagged by the FPC as a function of W in the e sample in GRAPE **a**, in the 99–00 data **b**, the data corrected for GRAPE **c** and fraction of inelastic events in the γ sample in the data **d**. The straight-line fit is also shown

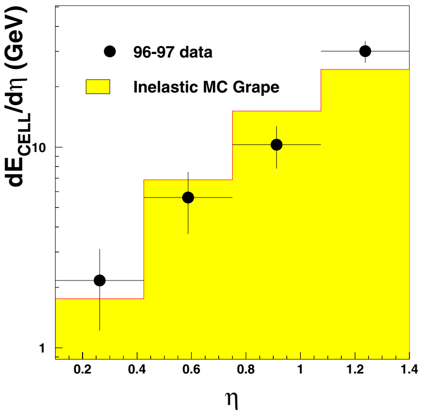

Fig. 60. Energy-flow distribution $dE_{\mathrm{cell}}/d\eta$ as a function of η for the FCAL region. The data (points) are compared to the inelastic GRAPE MC expectation (histogram)

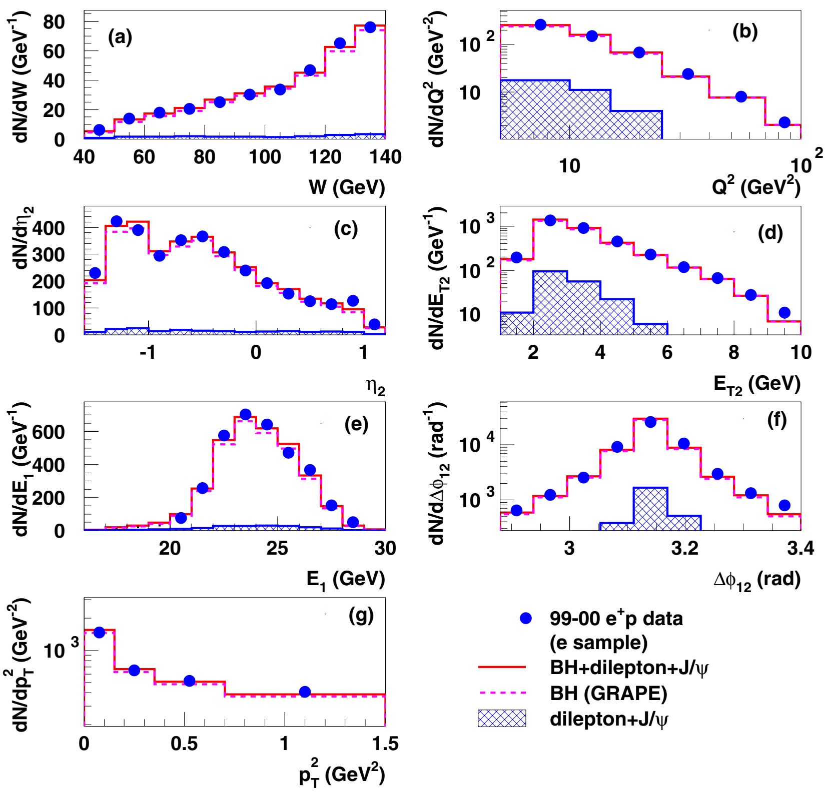

Fig. 61. Distributions of the e sample in **a** W, **b** Q^2, **c** η_2 – the pseudorapidity of the electron, **d** E_{T2} – the transverse energy of the electron, **e** E_1 – the energy of the photon, **f** $\Delta\phi_{12}$ – the difference of the azimuthal angles of γ and e, and **g** p_T^2. The data are represented by the points and the histograms represent: the sum of the prediction of GRAPE for the BH process and dilepton and J/ψ background (solid); the prediction of GRAPE for the BH alone (dashed) normalised to the data (including both elastic and inelastic contributions); and the prediction of the dilepton and J/ψ alone (hatched)

7.1.5 Control plots for the e sample

Finally, it can be concluded that the e sample consists only of the elastic and inelastic BH processes which altogether comprise about 95% of this sample. Remaining events comes from the dilepton production and diffractive J/ψ electroproduction processes.

Figures 61a–g show several distributions for the e sample compared to the MC predictions for the BH process, dilepton production and diffractive J/ψ electroproduction events. The MC distributions are normalised to the data in such a way that the sum of dilepton and J/ψ events is normalised to the wrong-sign-e sample (see Sect. 7.1.2), then this normalised background is added to the MC expectations for the BH process and a final normalisation established to the total number of events in the e sample. One can see that the MC predictions are in good agreement with the data.

After the subtraction of the dilepton and J/ψ backgrounds, for the 96–97 (99–00) e^+p samples, the number of remaining BH events in the e sample was 2523 (3289), while the expected number from the GRAPE simulation was 2601 (3358). The absolute expectation of the GRAPE simulation reproduced the number of BH data events to within $(3 \pm 5)\%$ for 96–97 and $(2 \pm 4)\%$ for 99–00, where uncertainties include the statistical uncertainty as well as the uncertainties due to the trigger efficiency and the estimation of the inelastic BH contribution.

7.2 Background in the γ sample

In the following, it will be shown that in the γ sample, the significant background comes only from the elastic and inelastic BH processes, as well as from the proton-dissociative DVCS events.

7.2.1 BH background and normalisation issue

The proper estimation of the number of BH events contributing to the γ sample is the crucial point for the subsequent extraction of the DVCS cross sections. The normalisation of the GRAPE MC sample was done according to the prescription given in Sect. 7.1.5. A question arises whether the GRAPE MC program simulates fractions of events participating the e sample and the γ sample correctly. If, for some reason, it overestimates a number of events in the e sample, it would result in underestimation of the DVCS events in the final γ sample (and vice versa) since in this case one subtracts too many background events from the γ sample. In order to check the GRAPE simulation of the elastic BH events with either an electron going to the RCAL with $\theta_\gamma < \theta_e$ (γ sample) or a photon with $\theta_\gamma > \theta_e$ (e sample), the Compton 2.0 [129] program was used. The same number of 40000 events was generated by means of these two generators in the same phase-space region used in this analysis and several distributions were compared.

Figure 62 shows the comparison of the electron-energy distributions generated using both MC programs. Two bumps are clearly seen. The low energy peak comes from elastic BH events participating the e sample, while the higher energy one contains the elastic BH events contributing to the γ sample. Moreover, Fig. 62 depicts the ratio of the number of Compton 2.0 events to GRAPE events. Comparing the total numbers of events in the bumps, about 1%

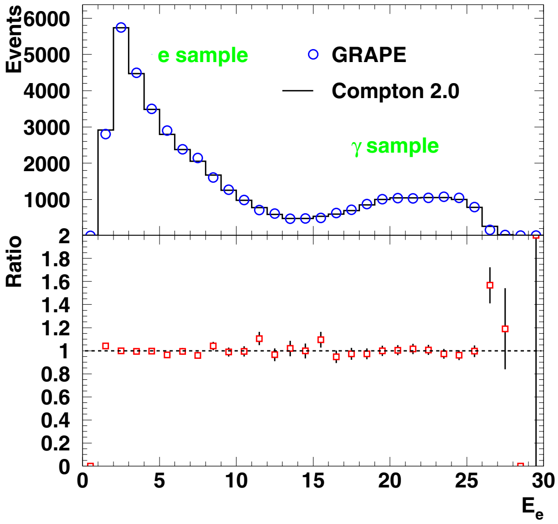

Fig. 62. The GRAPE MC predictions (open circles) compared to the Compton 2.0 predictions (histogram) for the elastic BH process. (Upper) The distribution of the electron energy E_e for the elastic BH process. (Lower) The ratio of the number of Compton 2.0 events over GRAPE events as a function of E_e

excess of number of events contributing to the e sample was found for GRAPE. On the other hand, the total elastic $ep \to e'\gamma p'$ cross section was found to be the same within 0.08% for the both programs. These results indicate that the both programs give the same predictions within the statistical uncertainty.

Figure 63 shows the distributions of the electron polar angle. Again, both MC programs yield the same results within the statistical uncertainties.

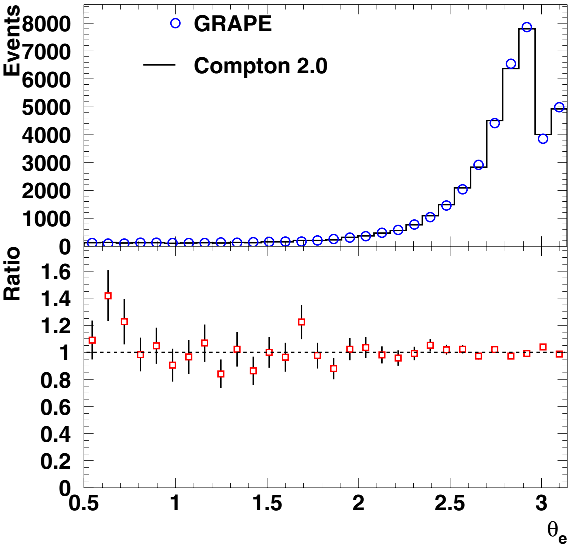

Fig. 63. The GRAPE MC predictions (open circles) compared to the Compton 2.0 predictions (histogram) for the elastic BH process. (Upper) The distribution of the electron polar angle θ_e for the elastic BH process. (Lower) The ratio of the number of Compton 2.0 over GRAPE events as a function of θ_e

It was decided to use the GRAPE program because it simulates the hadronic final state for the inelastic BH process, contrary to the Compton 2.0 program.

7.2.2 Inclusive diffractive and non-diffractive contributions

A possible contribution to the γ sample could come from low-multiplicity diffractive events

$$ep \to e'Xp'. \tag{13}$$

The RAPGAP program shows that following final states X could contribute to the γ sample:

- $\pi^0\pi^0$,
- $\pi^0\eta$,
- $K_L^0 K_S^0$,
- $\pi^0\omega$.

First two processes must be Odderon induced, but recent results show that they are not observed in diffraction [138], hence their contribution to the γ sample can be neglected. The third process with $K_L^0 K_S^0$ in a final state will be investigated in Sect. 7.2.4 for the ϕ meson electroproduction and showed that this contribution to the γ sample can be neglected. The same motivation concerns the last process with $\pi^0\omega$ in the final state. The study for the ω vector meson showed that the number of events coming from the ω electroproduction in the data is small and can be neglected. It means that none of diffractive final states quoted above can produce background for the γ sample.

The next point is the non-diffractive inclusive background. The DJANGOH MC simulation which generates process (13) yields the following final states X surviving the selection criteria listed in Sect. 5.6:

- π^0,
- η,
- $\pi^0\eta$,
- $\pi^0\pi^0$.

The normalisation of the DJANGOH MC sample to the luminosity in the data predicts that more than 90% of the total γ sample comes from these processes. Taking into account that about 50% of the γ sample consists of the BH events, this number seems to be overestimated and should be verified. Using cross sections for above processes estimated in the photoproduction region [139, 140] and the formulae taken from [141], one can estimate cross sections for mean values of $W = 89$ GeV and $Q^2 = 9.6$ GeV^2 of this analysis. Table 4 contains the evaluated cross-section values

Table 4. Cross sections estimated for the non-diffractive processes in the kinematic range of this analysis

Process	$\sigma^{\gamma^* p \to Xp}$ (pb)
$\gamma^* p \to \pi^0 p$	1.6
$\gamma^* p \to \eta p$	1.2
$\gamma^* p \to fp, f \to \pi^0\pi^0$	0.18
$\gamma^* p \to a_2^0 p, a_2^0 \to \pi^0\eta$	0.71
Total	3.69

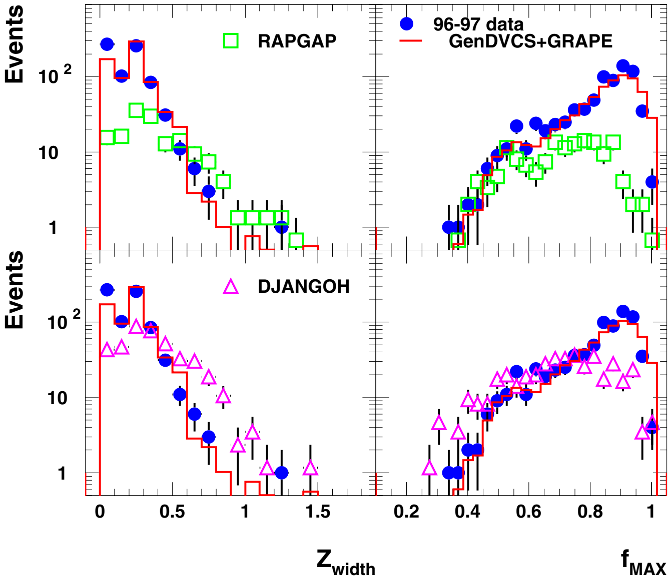

Fig. 64. Distributions of (left) the energy weighted Z width of the EM2 cluster expressed in units of the EM cell width, (right) the fraction of the EM2 cluster energy deposited in the most energetic cell in the cluster

for four non-diffractive processes which could contribute to the γ sample. It was found that the inclusive non-diffractive background is about 1000 times smaller than the overall number of events in the γ sample. Thus this background can be neglected.

Another way to study the π^0 and η background contributing to the γ sample is an analysis of the shower shapes. It can be expected that π^0 and η clusters, which are built up by two photons coming from the π^0 or η decay, should be broader, so the energy deposit in a single calorimeter cell ought to be smaller than in case of a single photon. For the purpose of this study the two shower-shape variables were defined:

- the energy weighted width of the EM cluster in the Z direction

$$Z_{\mathrm{width}} = \frac{\sum_i (|Z^i_{\mathrm{cell}} - \bar{Z}| \cdot E^i_{\mathrm{cell}})}{\sum_i E^i_{\mathrm{cell}}},$$

where E^i_{cell} and Z^i_{cell} denote the energy and Z coordinate of the i–th cell and $\bar{Z}$ stands for the average Z coordinate of the EM cluster. The sum is over all cells of the EM cluster.

- fraction of the EM cluster energy which is deposited in the most energetic cell of the cluster

$$f_{\mathrm{MAX}} = \frac{\text{energy of the most energetic cell in the cluster}}{\text{total energy in the cluster}}.$$

The distributions of these two shower-shape variables were studied for the EM2 cluster in the BCAL, which should be generated by a photon in case of the γ sample. In Fig. 64 the π^0 and η shower-shape distributions generated by DJANGOH and RAPGAP, normalised to the luminosity of the data, are compared to the 96–97 data. These plots show that the cluster reconstructed in the data have the same shapes as the photon clusters generated by the sum of the GRAPE and GenDVCS simulations. At the same time the π^0 and η showers seem to be quite different because of too small f_{MAX} and too large Z_{width}. These results prove that clusters seen in the data have different origins than those produced by the π^0 and η particles. Thus, the hadronic background from low-multiplicity processes cannot account for the excess of the data above the BH prediction in the γ sample.

7.2.3 Proton-dissociative DVCS background

The ZEUS measurements of elastic vector-meson production [142–144] support, with relatively large uncertainties, the assumption that the fraction of proton-dissociative events in diffractive interactions is process independent. Therefore, due to a lack of the MC program dedicated to the inelastic DVCS process in this analysis, the fraction $F^{\mathrm{tot}}_{\mathrm{pdiss}}$, determined from the measurements of the diffractive J/ψ photoproduction [144], was used for the 96–97 data:

$$F^{\mathrm{tot}}_{\mathrm{pdiss}} = 22.0 \pm 2.0(\mathrm{stat.}) \pm 2.0(\mathrm{syst.})\%$$

for the 98–00 data:

$$F^{\mathrm{tot}}_{\mathrm{pdiss}} = 17.5 \pm 1.3(\mathrm{stat.})^{+3.7}_{-3.2}(\mathrm{syst.})\%.$$

The above fractions are consistent, within large uncertainties, with those estimated using the events in the γ sample either tagged by the PRT1 or the FPC, after subtracting the inelastic BH contributions (see Sect. 7.1.3).

7.2.4 Other contributions

In addition other processes with the same signature were investigated as a potential source of background in the γ sample:

- diffractive ϕ electroproduction ($ep \to e'\phi p'$, $\phi \to K^0_L K^0_S$),
- diffractive ω electroproduction ($ep \to e'\omega p'$, $\omega \to \pi^0\gamma$).

The diffractive ϕ electroproduction could contribute to the DVCS event topology when the ϕ meson decays into two kaons ($\phi \to K^0_L K^0_S$) with the subsequent decay of the K^0_S into two neutral pions which further decay into two photons. If a scattered electron is detected in the RCAL and only one product of a decay of the vector meson gives a deposit in the CAL, an event topology is exactly the same like in the γ sample, so the γ sample would be contaminated by ϕ mesons. The final selection efficiency was studied for this channel of the ϕ decay by means of the MC simulation. Events mostly do not pass the selection cuts because either more than two clusters were found in the CAL, more than one track per event was reconstructed in the CTD or Q^2 value was too low. Using the cross section [145, 146] for selected ϕ events in the γ sample, the expected number of the ϕ events contaminating the γ sample was found below 0.1% of the total γ sample. Thus, the ϕ background can be neglected.

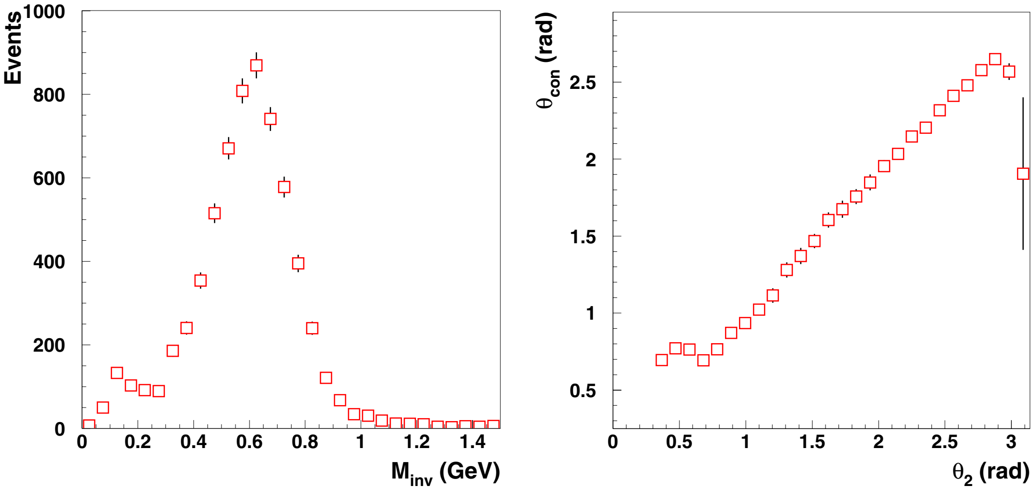

Fig. 65. Distribution of M_{inv} for the EM2 cluster and a condensate (left) and correlation between polar angles of the EM2 cluster θ_2 and of a condensate θ_{con} (right) for the $ep \to e'\omega p'$, $\omega \to \pi^0\gamma$ process in the γ sample as simulated by the ZEUSVM program

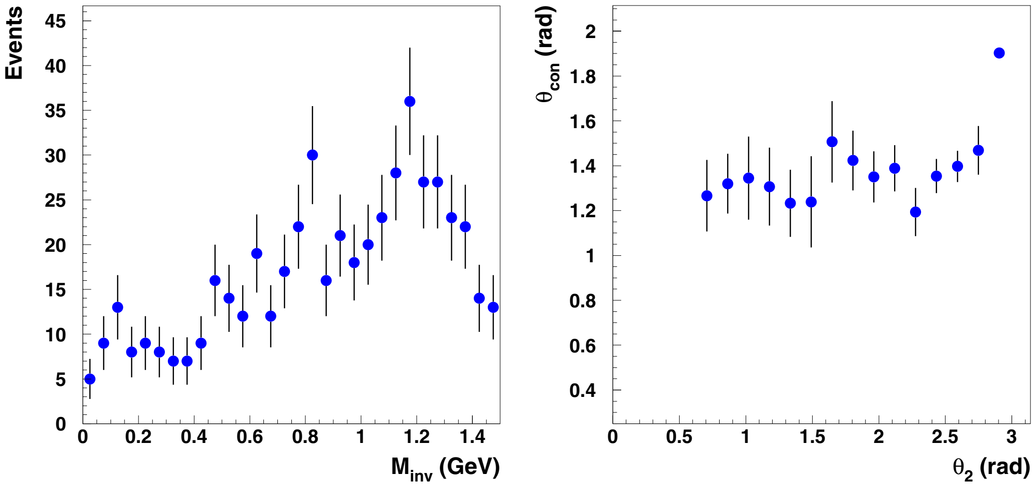

Fig. 66. Distribution of M_{inv} for the EM2 cluster and a condensate (left) and correlation between polar angles of the EM2 cluster θ_2 and of a condensate θ_{con} (right) for the $ep \to e'\omega p'$, $\omega \to \pi^0\gamma$ process in the γ sample in the data

The second process which was taken into account is a ω electroproduction, where the vector meson decays into $\pi^0\gamma$. If a scattered electron and only one of the decay products deposit energy in the CAL, this topology is like in the γ sample. The calculation of the cross section for the ω vector meson [147] shows that only about 0.3% of all events in the γ sample would come from this process. This means that this background can also be neglected.

The ω cross-section values can be verified by an attempt to find any ω-like events in the γ sample. The ZEUSVM MC simulation of the ω electroproduction shows that if one builds up condensates using cells not belonging to two EM clusters, the EM2 cluster from SINISTRA95 and the highest energy condensate are correlated for ω events. Figure 65 shows an invariant mass M_{inv} for these two EM objects. It is seen that a peak situated at about $M_{\text{inv}} = 0.65$ GeV comes from the decay products of the ω. The M_{inv} value is underestimated due to raw energy and position values used for the condensate. Moreover, the MC simulation shows that a strong correlation in the polar angles of these two objects (Fig. 65), demonstrates that both comes from one decay. Hence, a potential way to see the ω background in the data is to analyse these two dependencies for events belonging to the γ sample.

Figure 66 presents the invariant mass of the EM2 and the condensate system M_{inv} and dependence of polar angles θ_{con} vs θ_2 computed for a condensate and the EM2 cluster, respectively. Neither the M_{inv} distribution nor the θ dependence indicate that these two objects are correlated and come from the ω decay. It means that no significant amount of the ω background is observed in the γ sample.

7.2.5 Control plots for the γ sample

Finally, it can be concluded that the γ sample consists only of the elastic and inelastic DVCS events as well as the elastic and inelastic BH background which comprises about 44% of this sample. Other background processes contributing to this sample were found to be negligible.

Figures 67a–g show several distributions for the γ sample before the BH background subtraction. The data are compared with the prediction for the elastic and inelastic BH process, using the normalisation obtained by means of the e sample for GRAPE. A clear excess over the BH prediction is evident. Moreover, the data exhibit different shapes from those expected for BH, indicating a different process.

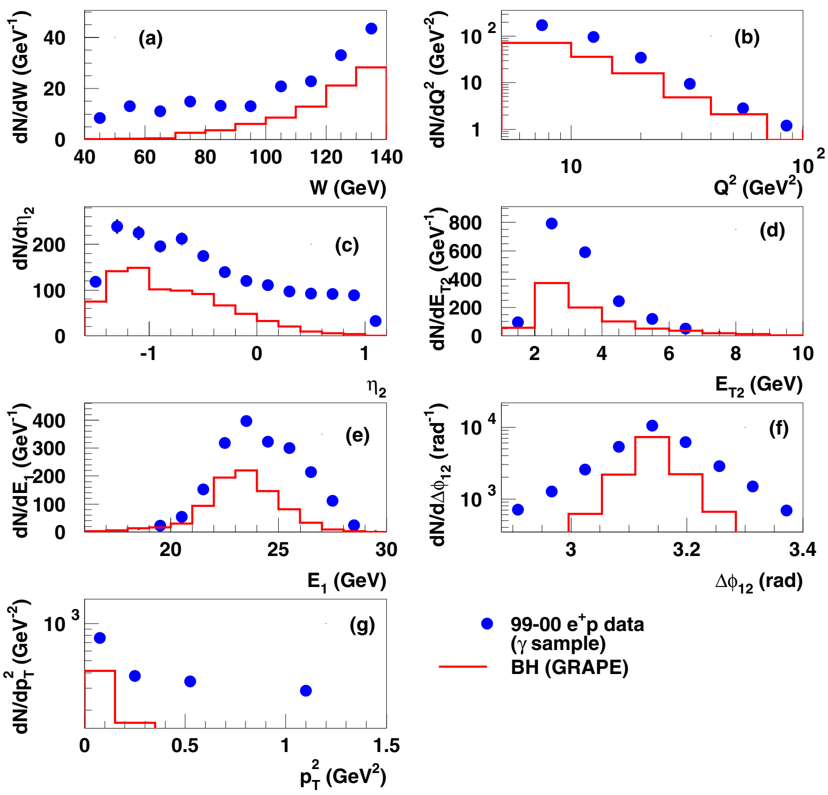

Fig. 67. Distributions of the γ sample in **a** W, **b** Q^2, **c** η_2 – the pseudorapidity of the γ, **d** E_{T2} – the transverse energy of the γ, **e** E_1 – the energy of the scattered e, **f** $\Delta\phi_{12}$ – the difference in azimuthal angles of the γ and e, and **g** p_T^2. The data are represented by the points and the histograms represent the prediction of GRAPE for the BH process, normalised to the e sample (including both elastic and inelastic contributions)

7.3 Beam-gas interactions

Protons from the beam can interact with molecules of residual gas in the beam pipe. At vacuum of 10^{-9} Torr and an effective length in front of the ZEUS detector of $\sim 100\,\text{m}$ the rate of beam-gas interactions is about 50 kHz of which a significant fraction may give signals in the detector. Most beam-gas events can be identified using the calorimeter timing cut at the SLT (see Sect. 5.4.2). Moreover, events interacting outside the ZEUS detector are rejected effectively using veto counters.

In order to get rid of this background from the data a number of events coming from non-colliding electron and proton bunches has to be scaled with the ratio of currents in the paired and unpaired bunches and then the number of background events should be subtracted from the data.

A data sample of unpaired bunches was analysed, in which only either electron or proton bunches were filled. No beam-gas event neither in the γ sample nor in the e sample fulfilling all the selection criteria was found.

8 Extraction of the cross sections

In the kinematic region of this analysis the interference between the DVCS and BH processes is negligible when the cross section is integrated over the angle between the e and p scattering planes [10, 11]. Thus the cross section for exclusive production of real photons may be treated as a simple sum of the contributions from the DVCS and the BH processes. The latter can, therefore, be subtracted and the DVCS cross section determined.

In the following, the extraction of the single differential ep cross section as well as the extraction of the $\gamma^* p$ cross section are described. Finally, the systematic uncertainties are discussed.

8.1 DVCS control distributions

Before describing the extraction of the cross sections the agreement between the data and the MC sample will be discussed on the basis of several control distributions. In Figs. 68a–g the data after subtraction of the elastic and inelastic BH background are compared to the absolute expectations of GenDVCS. The best agreement of normalisation of the data with the MC simulation is achieved when the absolute normalisation of the latter is decreased by 10%. This was obtained by increasing the value of b from 4.5 (assumed in the FFS model) to $4.9\,\text{GeV}^{-2}$ (see Sect. 6.2.1). Overall, good agreement between the data and the MC simulation is found, demonstrating that the excess of photon candidates over the expectation of BH is due to DVCS.

8.2 Unfolding procedure

After the final selection and the background subtraction, the measured number of events in each Q^2 and W bin does not directly reflect the DVCS cross section. The "true" distributions and the experimentally measured ones differ due to the finite resolution of the reconstructed quantities. Furthermore, the probability to observe an event in the

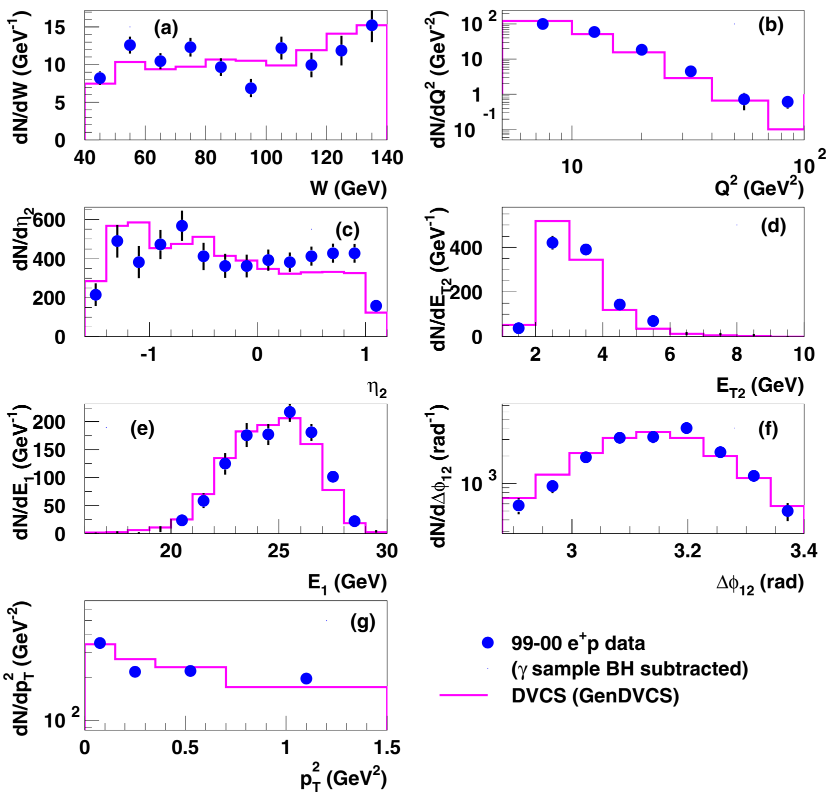

Fig. 68. Distributions of the γ sample, after subtraction of the BH contribution, in the same variables as in Fig. 67. The data are shown as points. The histogram represents the predictions of the GenDVCS MC program, normalised to the number of events in the data. The DVCS proton-dissociative background is not subtracted from the data

final sample is reduced by the trigger efficiency and the offline selection cuts. The procedure to obtain the cross section by correcting the data for smearing, migration and acceptance effects is commonly called "unfolding".

In general, the relation between the number of events $N_i^{\rm gen}$ produced in an $i-$th bin of the event variable and the number of events $N_j^{\rm meas}$ observed in the $j-$th bin of the corresponding measured (reconstructed) variable is described by the relation

$$N_j^{\rm meas} = \sum_i T_{ij} N_i^{\rm gen}, \qquad (14)$$

where T_{ij} is the transfer matrix. In the case of MC simulations the transfer matrix from (14) can be calculated easily because both measured numbers of events $N_{i,{\rm MC}}^{\rm meas}$ and generated ones $N_{i,{\rm MC}}^{\rm gen}$ are precisely known. If the MC simulation is able to describe the data precisely enough, the assumption can be done that

$$T_{ij}^{\rm data} = T_{ij}^{\rm MC},$$

where $T_{ij}^{\rm data}$ and $T_{ij}^{\rm MC}$ denote the transfer matrices for the data and the MC sample, respectively.

A detailed outline of the available unfolding procedures used in ZEUS can be found in [148]. For the purposes of this analysis the bin-by-bin unfolding procedure was chosen, which is the most frequently method used in ZEUS. This method approximates the transfer matrix by a diagonal matrix. The consequence is that it takes into account only migrations out of and into a bin under consideration. Moreover, the bins are not longer correlated, i.e. the information, where migrating events come from and go to, is lost.

For the diagonal transfer matrix

$$T_{ij} = \delta_{ij} T_i,$$

where δ_{ij} denotes the Kronecker's symbol and the diagonal elements are expressed as

$$T_i = \frac{N_{i,{\rm MC}}^{\rm meas}}{N_{i,{\rm MC}}^{\rm gen}}.$$

Substituting above expressions into (14) one obtains the unfolded number of events in the data

$$N_{i,{\rm data}}^{\rm unf} = \frac{N_{i,{\rm MC}}^{\rm gen}}{N_{i,{\rm MC}}^{\rm meas}} \cdot N_{i,{\rm data}}^{\rm meas},$$

where $N_{i,{\rm data}}^{\rm meas}$ denotes the measured number of events in the data.

The bin-by-bin unfolding method needs a good description of the data by the MC simulation over the whole kinematic range.

8.3 Efficiency, purity and acceptance

For an unbiased measurement, bins are required to be chosen in a kinematic region where the event acceptance is high enough. The bin size has to be sufficiently large to have many events generated and reconstructed in the same

Table 5. Values of the *ep* cross sections for the DVCS process as a function of Q^2 for the e^+p and e^-p data

Q^2 bin (GeV^2)	Q^2 (GeV^2)	$\frac{d\sigma}{dQ^2}$ ($\mathrm{pb/\,GeV}^2$) 96–97 e^+p	$\frac{d\sigma}{dQ^2}$ ($\mathrm{pb/\,GeV}^2$) 98–99 e^-p	$\frac{d\sigma}{dQ^2}$ ($\mathrm{pb/\,GeV}^2$) 99–00 e^+p
5–10	7.5	$4.40 \pm 0.34^{+0.62}_{-0.56}$	$4.34 \pm 0.49^{+0.53}_{-0.51}$	$4.21 \pm 0.27^{+0.32}_{-0.39}$
10–15	12.5	$1.10 \pm 0.14^{+0.17}_{-0.19}$	$1.02 \pm 0.20^{+0.20}_{-0.20}$	$1.33 \pm 0.11^{+0.11}_{-0.12}$
15–25	20	$0.37 \pm 0.06^{+0.06}_{-0.08}$	$0.28 \pm 0.08^{+0.08}_{-0.08}$	$0.35 \pm 0.04^{+0.04}_{-0.05}$
25–40	32.5	$0.10 \pm 0.03^{+0.04}_{-0.04}$	$0.11 \pm 0.04^{+0.04}_{-0.04}$	$0.11 \pm 0.03^{+0.03}_{-0.03}$
40–70	55	$0.04 \pm 0.02^{+0.02}_{-0.02}$	—	$0.014 \pm 0.008^{+0.008}_{-0.008}$
70–100	85	$0.002 \pm 0.007^{+0.007}_{-0.008}$	—	$0.019 \pm 0.008^{+0.008}_{-0.008}$

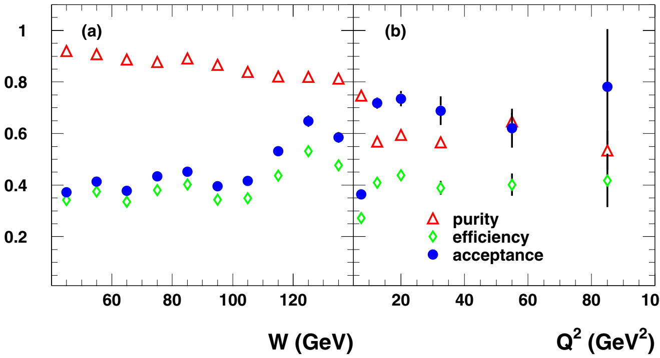

Fig. 69. Bin purity, efficiency and acceptance as a function of W **a** and Q^2 **b**

bin. These requirements can be quantified by introducing the bin efficiency $\mathcal{E}_i$, purity $\mathcal{P}_i$ and acceptance $\mathcal{A}_i$ as

$$\mathcal{E}_i = \frac{\text{Number of events generated and measured in the } i\text{-th bin}}{\text{Number of events generated in the } i\text{-th bin}},$$

$$\mathcal{P}_i = \frac{\text{Number of events generated and measured in the } i\text{-th bin}}{\text{Number of events measured in the } i\text{-th bin}},$$

$$\mathcal{A}_i = \frac{\text{Number of events measured in the } i\text{-th bin}}{\text{Number of events generated in the } i\text{-th bin}},$$

where all the three quantities are connected by a relation

$$\mathcal{E}_i = \mathcal{P}_i \cdot \mathcal{A}_i. \tag{15}$$

Figures 69a and b show the bin purity, efficiency and acceptance of each bin in W and Q^2, respectively. The bin efficiency expresses the probability of staying an event in the bin in which it was generated. Excluding the first bin, the efficiency is almost flat in Q^2, reaching 40–45%. The bin purity is a measure of migrations from adjacent bins into the measured bin. It is generally higher than 80% in W and lower in Q^2 where it reaches about 60%. This behaviour is a consequence of better resolution in W than in Q^2. The acceptance measures the effect of the trigger and offline selection cuts on the measured number of events. The acceptance reaches values of 40–60% for W and about 70% for $Q^2 > 10\,\mathrm{GeV}^2$. This behaviour, which is opposite to the purity behaviour, is a consequence of the relation (15), where $\mathcal{E}_i \sim$ const, so $\mathcal{A}_i \sim 1/\mathcal{P}_i$.

8.4 Extraction of the *ep* differential cross sections

The *ep* cross sections for the DVCS process as a function of W and Q^2 were evaluated using the expressions

$$\frac{d\sigma}{dW}(W_i) = \frac{(N_i^{\mathrm{obs}} - N_i^{\mathrm{BH}}) \cdot (1 - F_{\mathrm{pdiss}}^{\mathrm{tot}})}{N_i^{\mathrm{MC}}} \cdot \frac{d\sigma_{\mathrm{DVCS}}^{ep}}{dW}(W_i),$$

and

$$\frac{d\sigma}{dQ^2}(Q_i^2) = \frac{(N_i^{\mathrm{obs}} - N_i^{\mathrm{BH}}) \cdot (1 - F_{\mathrm{pdiss}}^{\mathrm{tot}})}{N_i^{\mathrm{MC}}} \cdot \frac{d\sigma_{\mathrm{DVCS}}^{ep}}{dQ^2}(Q_i^2),$$

where N_i^{obs} is the total number of data events in the γ sample in bin i in W and Q^2, N_i^{BH} denotes the number of BH events in the γ sample in that bin, determined from GRAPE after normalising to the e sample, and N_i^{MC} is the number of events expected in the γ sample from GenDVCS for the luminosity of the data. The factor $F_{\mathrm{pdiss}}^{\mathrm{tot}}$ is the fraction of the proton-dissociative DVCS events in the data (see Sect. 7.2.3), $\frac{d\sigma_{\mathrm{DVCS}}^{ep}}{dW}(W_i)$ and $\frac{d\sigma_{\mathrm{DVCS}}^{ep}}{dQ^2}(Q_i^2)$ are the *ep* single differential cross sections computed from the FFS model.

The *ep* cross sections have been computed in the ranges $5 < Q^2 < 100\,\mathrm{GeV}^2$ and $40 < W < 140\,\mathrm{GeV}$, separately for the 96–97, 98–99 and 99–00 data periods. Tables 5–7 list all the *ep* cross-section values with the first uncertainty being statistical and the second systematic.

8.5 $\gamma^* p \to \gamma p$ cross-section determination

The $\gamma^* p$ cross section for the DVCS process as a function of W and Q^2 was evaluated using the expression

$$\sigma(\gamma^* p \to \gamma p)(W_i, Q_i^2) = \frac{(N_i^{\mathrm{obs}} - N_i^{\mathrm{BH}}) \cdot (1 - F_{\mathrm{pdiss}}^{\mathrm{tot}})}{N_i^{\mathrm{MC}}} \times \sigma_{\mathrm{DVCS}}^{\gamma^* p}(W_i, Q_i^2),$$

where all quantities are defined in the same way as for the *ep* single differential cross sections and $\sigma_{\mathrm{DVCS}}^{\gamma^* p}$ is the $\gamma^* p$ cross section computed according to the FFS expression (4).

Table 6. Values of the ep cross sections for the DVCS process as a function of W for the e^+p data

W bin (GeV)	W (GeV)	$\frac{d\sigma}{dW}$ (pb/ GeV) 96–97 e^+p	$\frac{d\sigma}{dW}$ (pb/ GeV) 99–00 e^+p
40–50	45	$0.46 \pm 0.07^{+0.07}_{-0.08}$	$0.50 \pm 0.06^{+0.07}_{-0.07}$
50–60	55	$0.49 \pm 0.07^{+0.07}_{-0.08}$	$0.55 \pm 0.06^{+0.06}_{-0.07}$
60–70	65	$0.63 \pm 0.08^{+0.09}_{-0.13}$	$0.49 \pm 0.06^{+0.06}_{-0.06}$
70–80	75	$0.41 \pm 0.07^{+0.08}_{-0.08}$	$0.55 \pm 0.06^{+0.06}_{-0.08}$
80–90	85	$0.40 \pm 0.07^{+0.08}_{-0.08}$	$0.39 \pm 0.05^{+0.06}_{-0.06}$
90–100	95	$0.42 \pm 0.08^{+0.08}_{-0.09}$	$0.28 \pm 0.05^{+0.06}_{-0.06}$
100–110	105	$0.56 \pm 0.09^{+0.10}_{-0.13}$	$0.51 \pm 0.07^{+0.07}_{-0.08}$
110–120	115	$0.43 \pm 0.08^{+0.09}_{-0.11}$	$0.34 \pm 0.06^{+0.07}_{-0.07}$
120–130	125	$0.29 \pm 0.08^{+0.10}_{-0.09}$	$0.33 \pm 0.06^{+0.06}_{-0.07}$
130–140	135	$0.22 \pm 0.09^{+0.14}_{-0.09}$	$0.39 \pm 0.06^{+0.09}_{-0.07}$

Table 7. Values of the ep cross sections for the DVCS process as a function of W for the e^-p data

W bin (GeV)	W (GeV)	$\frac{d\sigma}{dW}$ (pb/ GeV) 98–99 e^-p
40–73	56.7	$0.49 \pm 0.06^{+0.06}_{-0.06}$
73–107	90	$0.41 \pm 0.06^{+0.07}_{-0.06}$
107–140	123.3	$0.26 \pm 0.06^{+0.07}_{-0.07}$

Table 8. Values of the cross sections for the $\gamma^*p \to \gamma p$ DVCS process as a function of Q^2 for the e^+p and e^-p data. Values are quoted at the centre of each Q^2 bin and for the average W value of the whole sample, $W = 89\,\mathrm{GeV}$, obtained from GenDVCS

Q^2 bin (GeV^2)	Q^2 (GeV^2)	$\sigma^{\gamma^*p\to\gamma p}$ (nb) e^+p	$\sigma^{\gamma^*p\to\gamma p}$ (nb) e^-p
5–10	7.5	$5.42 \pm 0.33^{+0.29}_{-0.34}$	$5.63 \pm 0.77^{+0.30}_{-0.33}$
10–15	12.5	$2.64 \pm 0.22^{+0.11}_{-0.13}$	$2.20 \pm 0.52^{+0.13}_{-0.14}$
15–25	20	$1.23 \pm 0.14^{+0.05}_{-0.07}$	$0.96 \pm 0.31^{+0.10}_{-0.06}$
25–40	32.5	$0.59 \pm 0.12^{+0.04}_{-0.04}$	$0.61 \pm 0.28^{+0.06}_{-0.05}$
40–70	55	$0.20 \pm 0.08^{+0.03}_{-0.02}$	—
70–100	85	$0.16 \pm 0.09^{+0.02}_{-0.03}$	—

The γ^*p cross sections have been computed in the ranges $5 < Q^2 < 100\,\mathrm{GeV}^2$ and $40 < W < 140\,\mathrm{GeV}$, separately for the 96–97, 98–99 and 99–00 data periods and then combined for the positron samples (96–97 and 99–00). Tables 8–10 list all the $\gamma^*p \to \gamma p$ cross-section values with the first uncertainty being statistical and the second systematic.

8.6 Systematic uncertainties

The systematic uncertainties of the measured cross sections were determined by changing the selection cuts or the analysis procedure in turn and repeating the extraction of the cross sections. Figures 70 and 71 show the relative systematic uncertainty as a function of Q^2 and W, respectively, for the 37 systematic checks:

1. all the selection cuts discussed in Sect. 5.6 were shifted according to the resolutions of the corresponding variables:

Table 9. Values of the cross sections for the $\gamma^*p \to \gamma p$ DVCS process as a function of W for the e^+p and e^-p data. Values are quoted at the centre of each W bin and for the average Q^2 value of the whole sample, $Q^2 = 9.6\,\mathrm{GeV}^2$, obtained from GenDVCS

W bin (GeV) e^+p	W (GeV) e^+p	$\sigma^{\gamma^*p\to\gamma p}$ (nb) e^+p	W bin (GeV) e^-p	W (GeV) e^-p	$\sigma^{\gamma^*p\to\gamma p}$ (nb) e^-p
40–50	45	$2.19 \pm 0.24^{+0.11}_{-0.14}$			
50–60	55	$2.96 \pm 0.28^{+0.13}_{-0.18}$			
60–70	65	$3.62 \pm 0.36^{+0.18}_{-0.23}$	40–73	56.7	$2.94 \pm 0.39^{+0.16}_{-0.13}$
70–80	75	$3.88 \pm 0.42^{+0.18}_{-0.26}$			
80–90	85	$3.59 \pm 0.45^{+0.18}_{-0.25}$			
90–100	95	$3.29 \pm 0.55^{+0.21}_{-0.20}$	73–107	90	$4.06 \pm 0.69^{+0.35}_{-0.25}$
100–110	105	$6.24 \pm 0.77^{+0.31}_{-0.49}$			
110–120	115	$4.86 \pm 0.76^{+0.39}_{-0.44}$			
120–130	125	$4.69 \pm 0.82^{+0.32}_{-0.36}$	107–140	123.3	$3.8 \pm 1.1^{+0.3}_{-0.4}$
130–140	135	$5.55 \pm 0.99^{+0.91}_{-0.30}$			

Table 10. Values of the cross sections for the $\gamma^* p \to \gamma p$ DVCS process as a function of W for the e^+p data in three Q^2 ranges. Values are quoted at the centre of each W bin and for the average Q^2 values obtained from GenDVCS

W bin (GeV) e^+p	W (GeV) e^+p	$\sigma^{\gamma^* p\to\gamma p}$ (nb) $5 < Q^2 < 8\,\mathrm{GeV}^2$ $Q^2 = 6.2\,\mathrm{GeV}^2$	$\sigma^{\gamma^* p\to\gamma p}$ (nb) $8 < Q^2 < 13\,\mathrm{GeV}^2$ $Q^2 = 9.9\,\mathrm{GeV}^2$	$\sigma^{\gamma^* p\to\gamma p}$ (nb) $13 < Q^2 < 30\,\mathrm{GeV}^2$ $Q^2 = 18.0\,\mathrm{GeV}^2$
40–65	52.5	$5.63 \pm 0.58^{+0.40}_{-0.35}$	$2.52 \pm 0.26^{+0.09}_{-0.18}$	$0.99 \pm 0.13^{+0.05}_{-0.10}$
65–90	77.5	$6.57 \pm 0.91^{+0.47}_{-0.81}$	$3.12 \pm 0.39^{+0.21}_{-0.17}$	$1.34 \pm 0.17^{+0.05}_{-0.09}$
90–115	102.5	$9.5 \pm 1.5^{+0.8}_{-1.4}$	$3.94 \pm 0.61^{+0.32}_{-0.30}$	$1.91 \pm 0.30^{+0.12}_{-0.12}$
115–140	127.5	$7.6 \pm 1.6^{+1.5}_{-0.6}$	$5.83 \pm 0.89^{+0.49}_{-0.48}$	$1.64 \pm 0.47^{+0.13}_{-0.15}$

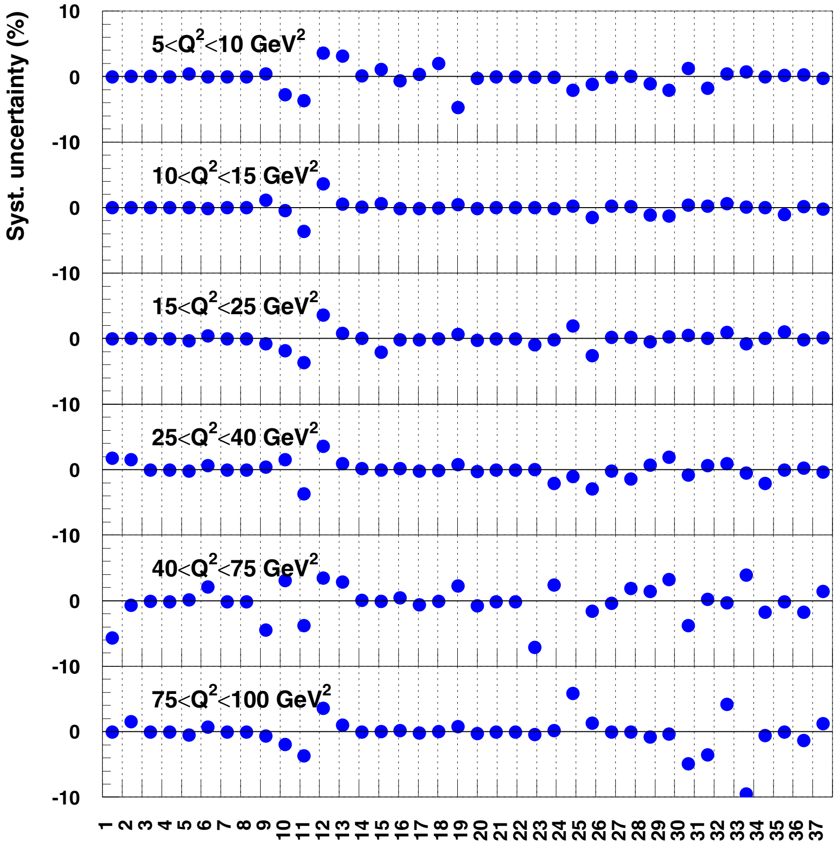

Fig. 70. Systematic uncertainties for the $\gamma^* p \to \gamma p$ DVCS process measured for $40 < W < 140\,\mathrm{GeV}$ and $5 < Q^2 < 100\,\mathrm{GeV}^2$ for the 99–00 e^+p data sample. The uncertainties in six Q^2 bins are shown. The numbers in X axis are the systematic check numbers given in the text

- DCA $< 25\,\mathrm{cm}$ (1)[17] and DCA $< 15\,\mathrm{cm}$ (2),
- $E_1 > 16\,\mathrm{GeV}$ (3) and $E_1 > 14\,\mathrm{GeV}$ (4),
- $P_2^{\mathrm{Si}} > 0.75$ (5) and $P_2^{\mathrm{Si}} > 0.65$ (6),
- $P_1^{\mathrm{Si}} > 0.95$ (7) and $P_2^{\mathrm{Si}} > 0.85$ (8),
- $Q^2 > 5.5\,\mathrm{GeV}^2$ (13) and $Q^2 > 4.5\,\mathrm{GeV}^2$ (14),
- $E_2 > 2.6\,\mathrm{GeV}$ (15) and $E_2 > 2.4\,\mathrm{GeV}$ (16),
- $\theta_2 < 2.8\,\mathrm{rad}$ (17) and $\theta_2 < 2.7\,\mathrm{rad}$ (18),
- $43 < E - p_Z < 67\,\mathrm{GeV}$ (23) and $37 < E - p_Z < 73\,\mathrm{GeV}$ (24),
- $E_{\mathrm{FPC}} < 1.1\,\mathrm{GeV}$ (27) and $E_{\mathrm{FPC}} < 0.9\,\mathrm{GeV}$ (28),
- all events for which a position of the EM1 cluster (X_1, Y_1) satisfies the following condition

$$|X_1| < 13.5\,\mathrm{cm} \quad \text{and} \quad |Y_1| < 7.5\,\mathrm{cm}\ (19)$$

and

$$|X_1| < 12.5\,\mathrm{cm} \quad \text{and} \quad |Y_1| < 6.5\,\mathrm{cm}\ (20),$$

were rejected,
- the SRTD impact position corresponding to the EM1 cluster $(X_1^{\mathrm{SRTD}}, Y_1^{\mathrm{SRTD}})$ was changed accordingly

$$X_1^{\mathrm{SRTD}} = X_1^{\mathrm{SRTD}} + 2\,\mathrm{mm}$$

---

[17] The number in brackets is the systematic check number in Figs. 70 and 71.

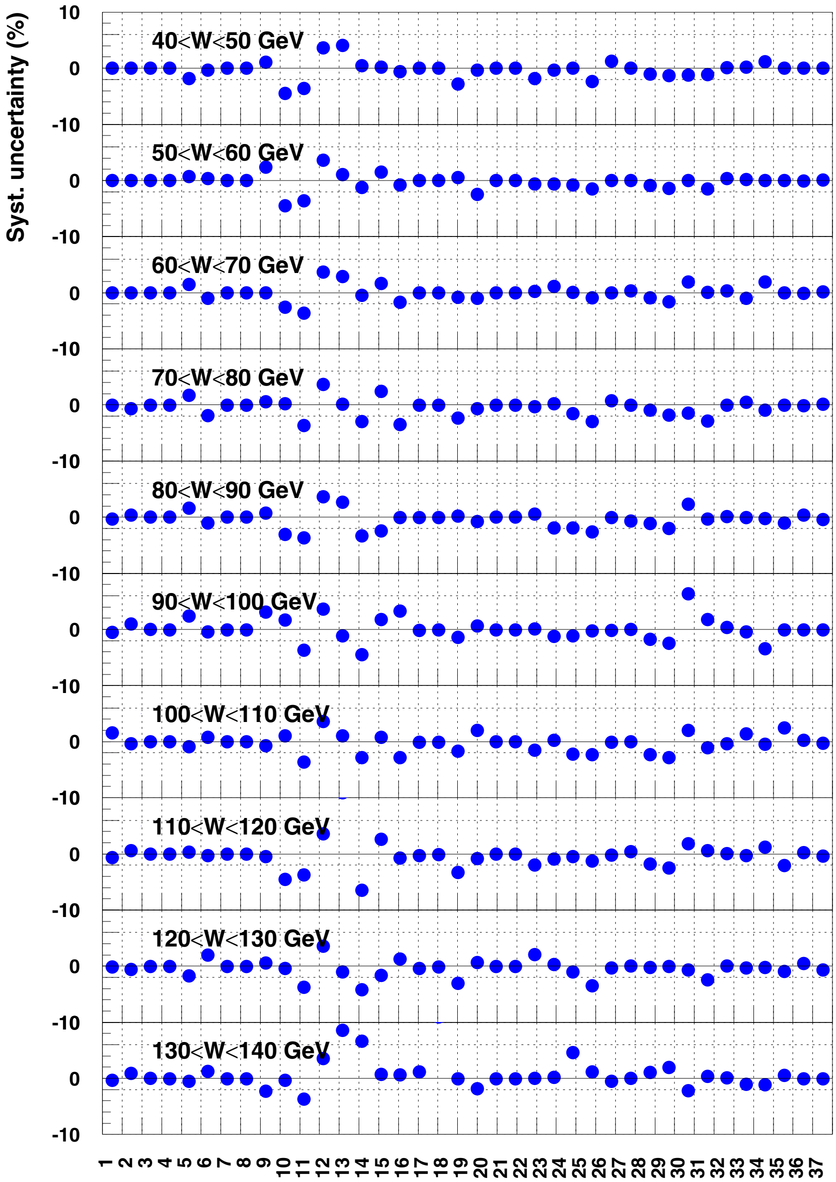

Fig. 71. Systematic uncertainties for the $\gamma^* p \to \gamma p$ DVCS process measured for $40 < W < 140\,\mathrm{GeV}$ and $5 < Q^2 < 100\,\mathrm{GeV}^2$ for the 99–00 e^+p data sample. The uncertainties in ten W bins are shown. The numbers in X axis are the systematic check numbers given in the text

$$\text{and} \quad Y_1^{\mathrm{SRTD}} = Y_1^{\mathrm{SRTD}} + 2\,\mathrm{mm} \quad (35),$$

and

$$X_1^{\mathrm{SRTD}} = X_1^{\mathrm{SRTD}} - 2\,\mathrm{mm}$$

$$\text{and} \quad Y_1^{\mathrm{SRTD}} = Y_1^{\mathrm{SRTD}} - 2\,\mathrm{mm} \quad (36).$$

The most significant contributions came from varying the lower Q^2 cut. The average change in the cross section due to this cut was ±2%. The largest change in the cross section, ±10%, was found in the highest-W bin, while it was ±4% in the lowest-Q^2 bin.

2. the elasticity cut was changed by

$$+30\,\mathrm{MeV} \text{ in the EMC and } +50\,\mathrm{MeV} \text{ in the HAC } (9)$$

and

$$-30\,\mathrm{MeV} \text{ in the EMC and } -50\,\mathrm{MeV} \text{ in the HAC } (10).$$

The average change in the cross section was ±2% in all bins of Q^2 and W, while the largest change in the cross section, observed when the cut was lowered, was −4% in the lowest-W bins and −4% in the lowest-Q^2 bin.

3. the fraction of the inelastic component in the BH events was varied in the range

$$\begin{aligned} &(17.95 + 1.10)\% \text{ for 96–97} \\ \text{and} \quad &(11.05 + 0.96)\% \text{ for 98–00 } (11), \\ &(17.95 - 1.10)\% \text{ for 96–97} \\ \text{and} \quad &(11.05 - 0.96)\% \text{ for 98–00 } (12), \end{aligned}$$

leading to a change in the cross section of about ±1%, evenly distributed over the bins.

4. the trigger efficiency was varied within its statistical uncertainty as

$$we(E_2) + \sigma_{we(E_2)} \ (29),$$

$$we(E_2) - \sigma_{we(E_2)} \ (30).$$

This resulted in average changes of the cross section of about ±2%. The biggest variation of the cross section of ±3% was observed in the lowest-Q^2 bin and in the two highest-W bins.

5. the electromagnetic energy scale was varied within its uncertainty of

$$+1.5\% \ (31) \text{ and } -1.5\% \text{ for EM2 (low energy) } (32),$$
$$+1\% \text{ for EM1 (high energy) } (25),$$

resulting in a ±3% average change of the cross section in both Q^2 and W. The largest change was ±3% for the lowest-Q^2 bins and ±5% for the highest-W bin.

6. in GenDVCS, the t dependence was modified by varying b as

$$b = 4\,\text{GeV}^{-2} \ (33) \text{ and } b = 7\,\text{GeV}^{-2} \ (34),$$

and a Q^2-dependent t slope using the formula (see Sect. 9.2.2)

$$b = 8(1 - 0.15\ln(Q^2/2))\,\text{GeV}^{-2} \ (37).$$

The average change in the cross section was ±1%, with the largest variation of ±3% in the highest-Q^2 bin.

The uncertainty on the proton-dissociative contribution [144], $F^{\text{tot}}_{\text{pdiss}}$, leads to an overall normalisation uncertainty of

$$+4.0\% \text{ for } e^-p \quad \text{and} \quad +3.5\% \text{ for } e^+p \ (11),$$
$$-4.0\% \text{ for } e^-p \quad \text{and} \quad -3.5\% \text{ for } e^+p \ (12).$$

The systematic uncertainties typically are small compared to the statistical uncertainties. The individual systematic uncertainties, including that due to $F^{\text{tot}}_{\text{pdiss}}$, were added in quadrature separately for the positive and negative deviations to obtain the total systematic uncertainties listed in Tables 5–10. An overall normalisation uncertainties in the luminosity determination of ±1.8% and ±2.0% for the e^-p and e^+p data, respectively, were not included because they are small comparing to the above contributions.

9 Results and discussion

In this section the results of the measurement of the ep differential and γ^*p cross sections are discussed. This is the first measurement of the DVCS process for the whole ZEUS data in 1996–2000. The results are shown for the e^+p and e^-p interactions separately. They are given with statistical alone and statistical and systematic uncertainties added in quadrature. The results are compared with the H1 results. Finally, the measured values are compared to the predictions based on the several DVCS models.

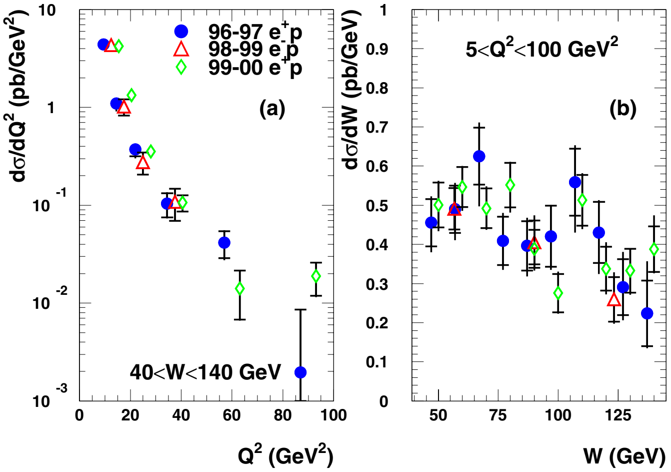

Fig. 72. The ep differential cross sections as a function of Q^2 for $40 < W < 140\,\text{GeV}$ **a** and as a function of W for $5 < Q^2 < 100\,\text{GeV}^2$ **b** for the 96–97 (dots), 98–99 (triangles) and 99–00 data (diamonds) for the DVCS process. The data points for the 98–99 e^-p and 99–00 e^+p running periods are displaced horizontally for ease of visibility

9.1 The *ep* differential cross sections

The measured ep differential cross sections of the DVCS process as a function of Q^2 and W are shown in Figs. 72a and b, respectively. The data are presented for three running periods: 96–97 e^+p, 98–99 e^-p and 99–00 e^+p separately. Due to limited statistics the $d\sigma/dQ^2$ cross section for e^-p is not measured in the last two Q^2 bins. For the same reason $d\sigma/dW$ for e^-p is shown in three W bins only.

The different proton-beam energy for the 96–97 (820 GeV) and 98–00 (920 GeV) running periods causes the results for these two periods can not be compared directly. Nevertheless, the comparison can be performed between the 98–99 e^-p and 99–00 e^+p data sets at the ep differential cross section level. Within present uncertainties the two results seem to be compatible with no difference, indicating no sensitivity of the present analysis to the interference term for BH and DVCS.

9.2 The γ^*p cross sections

The W dependence of the γ^*p DVCS cross section σ^{γ^*p} for $Q^2 = 9.6\,\text{GeV}^2$ is shown in Fig. 73, separately for e^+p and e^-p interactions. Due to the limited statistics, the e^- sample is shown in three W bins only. One observes a good agreement between the two cross sections.

A fit of the form $\sigma^{\gamma^*p} \propto W^\delta$ was performed separately for the positron and electron data. For the e^+p data, the value $\delta = 0.75 \pm 0.15(\text{stat.})^{+0.08}_{-0.06}(\text{syst.})$ is comparable to the result determined for J/ψ electroproduction [144]. This steep rise of the cross section is a strong indication for a hard underlying process. The same fit to the e^-p data yields $\delta = 0.45 \pm 0.36(\text{stat.})^{+0.08}_{-0.07}(\text{syst.})$, which is compatible with the e^+p result.

The positron sample has been subdivided into three Q^2 ranges. The W dependence of σ^{γ^*p} in these three Q^2 bins

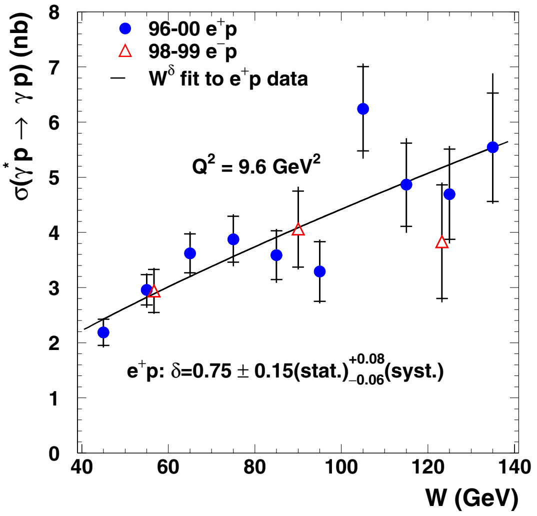

Fig. 73. The DVCS cross section, $\sigma(\gamma^* p \to \gamma p)$, as a function of W for an average $Q^2 = 9.6\,\mathrm{GeV}^2$, for e^+p data (dots) and e^-p data (triangles). The solid line is the result of the fit W^δ to the positron data

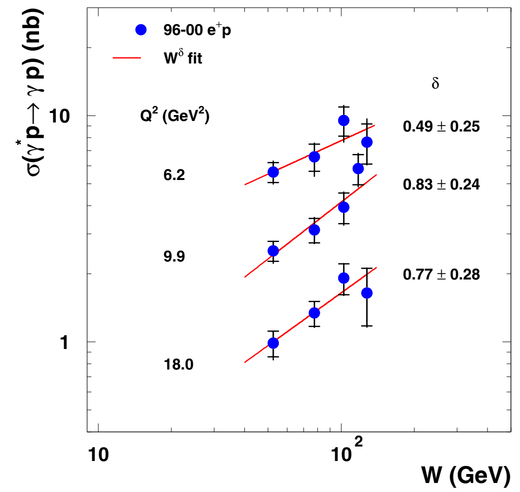

Fig. 74. The DVCS cross section, $\sigma(\gamma^* p \to \gamma p)$, as a function of W for three Q^2 values for e^+p data as denoted in the figure. The corresponding ranges in Q^2 are listed in Table 10. The solid line is the result of the fit W^δ. The values of δ and their statistical uncertainties are given in the figure. The last data point for $Q^2 = 9.9\,\mathrm{GeV}^2$ is displaced horizontally for ease of visibility

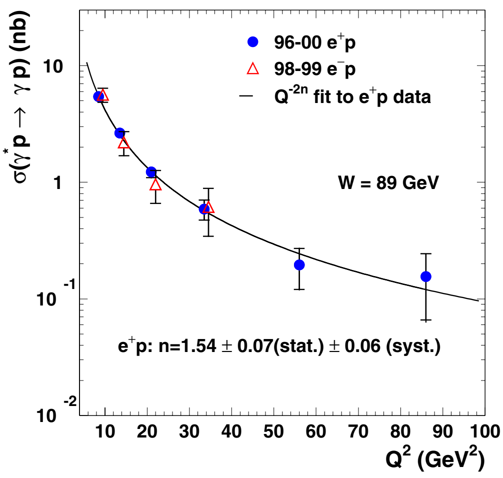

Fig. 75. The DVCS cross section, $\sigma(\gamma^* p \to \gamma p)$, as a function of Q^2 for $W = 89\,\mathrm{GeV}$, separately for e^+p data (dots) and e^-p data (triangles). The solid line is the result of the fit Q^{-2n} to the positron data. The e^-p data points are displaced horizontally for ease of visibility

is presented in Fig. 74. The results are compatible with no dependence of δ on Q^2 although also with the increase with Q^2 observed in exclusive production of light vector mesons [142, 149].

The Q^2 dependence of $\sigma^{\gamma^* p}$, for $W = 89\,\mathrm{GeV}$, is shown in Fig. 75. There is no significant difference between the e^+ and e^- data, which confirms the assumption that the measurement is insensitive to the interference term.

A fit of the form Q^{-2n} to the e^+p data gives a value of $n = 1.54 \pm 0.07(\mathrm{stat.}) \pm 0.06(\mathrm{syst.})$. This value is lower than $n \simeq 2$ which is characteristic for the exclusive vector-meson production [142, 150]. The fit to the e^-p data gives $n = 1.69 \pm 0.21(\mathrm{stat.})^{+0.09}_{-0.06}(\mathrm{syst.})$ indicating that the DVCS cross section is less suppressed in Q^2 than the exclusive vector-meson electroproduction.

9.2.1 Comparison with the H1 results

The H1 measurement for the DVCS process [14] was performed in the ranges $2 < Q^2 < 20\,\mathrm{GeV}^2$, $30 < W < 120\,\mathrm{GeV}$ and $|t| < 1\,\mathrm{GeV}^2$ using integrated luminosity of $8\,\mathrm{pb}^{-1}$ of data taken during the 1997 running period. These intervals yield mean values of Q^2 and W as $Q^2_{\mathrm{H1}} = 4.5\,\mathrm{GeV}^2$ and $W_{\mathrm{H1}} = 75\,\mathrm{GeV}$, respectively. They are significantly different from the values of this analysis[18] $Q^2_{\mathrm{ZEUS}} = 9.6\,\mathrm{GeV}^2$ and $W_{\mathrm{ZEUS}} = 89\,\mathrm{GeV}$. For comparison of the two results the H1 cross section in the i−th bin of Q^2_i and for mean W_{H1} denoted as $\sigma^{\mathrm{meas}}_{i,\mathrm{H1}}$ has to be extrapolated to the ZEUS value of W_{ZEUS} using a formula

$$\sigma^{\mathrm{extrap}}_{i,\mathrm{ZEUS}} = \sigma^{\mathrm{meas}}_{i,\mathrm{H1}} \cdot \frac{\sigma^{\gamma^* p}_{\mathrm{DVCS}}(W_{\mathrm{ZEUS}}, Q^2_i)}{\sigma^{\gamma^* p}_{\mathrm{DVCS}}(W_{\mathrm{H1}}, Q^2_i)}, \qquad (16)$$

where $\sigma^{\gamma^* p}_{\mathrm{DVCS}}$ is the cross section defined according to (4) based on the FFS calculation and $\sigma^{\mathrm{extrap}}_{i,\mathrm{ZEUS}}$ denotes the H1 measurement in the i−th bin moved to the ZEUS value W_{ZEUS}. The b slope is assumed to be fixed. The similar expression can be used in bins of W. Figures 76a and b show results of the comparison as functions of Q^2 and W, respectively. One can see that the H1 data lie systematically below the measurement of this thesis.

If one takes into account that the FFS model does not describe the data pretty well at low Q^2 mainly due to Q^2-dependent b slope, the formula (16) seems not to be proper for moving the H1 points to the ZEUS kinematic region. Thus, incorporating the Q^2-dependent b and the

---

[18] The results of this analysis are referred to as the ZEUS measurement.

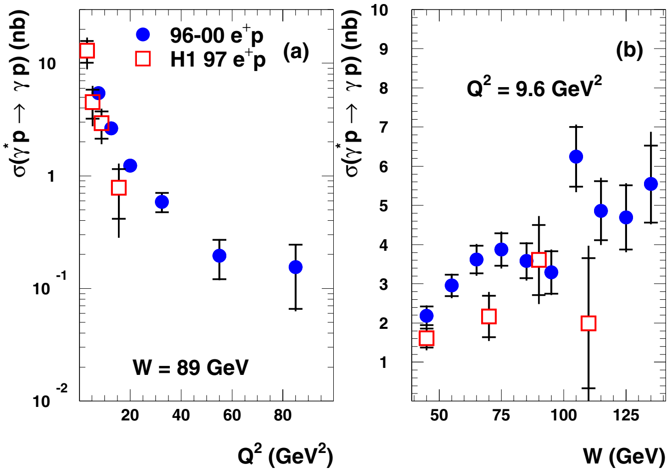

Fig. 76. The DVCS cross section, $\sigma(\gamma^* p \to \gamma p)$, as a function of Q^2 **a** for $W = 89\,\mathrm{GeV}$ and as a function of W **b** for $Q^2 = 9.6\,\mathrm{GeV}^2$ for the measurements of this thesis (dots) and the H1 97 e^+p data (squares)

parameterisation of the Q^2 dependence obtained in this analysis, the following expression was derived

$$\sigma_{i,\mathrm{ZEUS}}^{\mathrm{extrap}} = \sigma_{i,\mathrm{H1}}^{\mathrm{meas}} \cdot \frac{b_{\mathrm{H1}}}{b_{\mathrm{ZEUS}}} \cdot \left(\frac{Q^2_{\mathrm{ZEUS}}}{Q^2_{\mathrm{H1}}} \right)^{-n} , \qquad (17)$$

assuming $b = 8(1 - 0.15 \ln(Q^2/2))$ (for details see Sect. 9.2.2) and $n = 1.54$, which is the value taken from the fit to $\sigma^{\gamma^* p}$ dependence on Q^2 of the ZEUS e^+p data. This formula is valid under assumption that n does not depend on Q^2 nor W. The equivalent procedure for extrapolating in Q^2 can not be applied due to unknown δ dependence on Q^2 below $6.2\,\mathrm{GeV}^2$. Applying (17) instead of (16) for comparison between the H1 and ZEUS points, a similar systematic shift as before for the H1 measurement was found (not shown in figure).

Recently, the new H1 measurement was reported [151] in an extended kinematic range of $4 < Q^2 < 80\,\mathrm{GeV}^2$, $30 < W < 140\,\mathrm{GeV}$ and $|t| < 1\,\mathrm{GeV}^2$ using integrated luminosity of $26\,\mathrm{pb}^{-1}$ of data taken during the 2000 e^+p running period. The new H1 measurement is in fair agreement with the ZEUS e^+p results (comparison in [151]) except for $W \sim 70\,\mathrm{GeV}$ for which the H1 point is lower by about two standard deviations.

9.2.2 Comparison with models

GPD-based predictions

In Fig. 77 the cross section $\sigma^{\gamma^* p}$ as a function of Q^2 for the e^+p data is compared to the FFS expectations (see Sect. 2.5.1) based on the ALLM97 parameterisation of the parton distribution functions. The primarily assumed b slope of the t distribution in GenDVCS, $b = 4.5\,\mathrm{GeV}^{-2}$, was found not to describe the data (see Sect. 8.1) and was increased to $b = 4.9\,\mathrm{GeV}^{-2}$ to give a good description of normalisation of the data. Nevertheless, for $Q^2 > 20\,\mathrm{GeV}^2$, the e^+p data lie significantly above the FFS prediction.

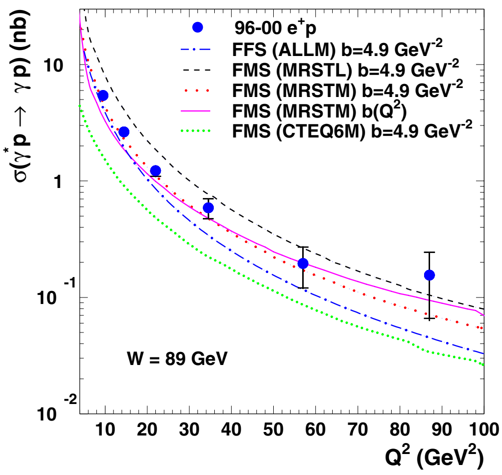

Fig. 77. $\sigma(\gamma^* p \to \gamma p)$ as a function of Q^2 compared to the GPD-based theoretical predictions of FFS and FMS, where MRSTL (MRSTM) indicates the LO (NLO) parameterisation of PDF. The MRSTM expectations are also shown for the Q^2-dependent b values described in the text. The CTEQ6 prediction is only shown for the NLO parameterisation of PDF

Freund, McDermott and Strikman (FMS) [49] have made an attempt to model the GPD based on DVCS data [14, 16, 17, 152, 153]. This was achieved by modelling $\Im\mathrm{m}\,\mathcal{A}_{\mathrm{DVCS}}$ at the input scale using the aligned jet model [154, 155]. This was then compared to the imaginary part of the DIS amplitude, calculated within the same framework, which was found to be smaller by a factor of about two. The comparison enabled the normalisation of $\mathcal{A}_{\mathrm{DVCS}}$ at the input scale μ to be set using F_2 structure function data. The inclusive PDF for quark singlet $q(x, \mu^2)$ and for gluons $g(x, \mu^2)$ were set such that the function H, which is the only important GPD at small x, was given at the scale μ by $H_q(x, \xi, t, \mu^2) = q(x, \mu^2)e^{-b|t|}$ and $H_g(x, \xi, t, \mu^2) = xg(x, \mu^2)e^{-b|t|}$ independently on ξ. Then $\mathcal{A}_{\mathrm{DVCS}}$ was evolved to higher Q^2 values using LO skewed evolution in pQCD.

A comparison of the measured $\sigma^{\gamma^* p}$ as a function of Q^2 for fixed W with the predictions based on the MRST and CTEQ6 parameterisations of the PDF [156, 157] is presented in Fig. 77. Four FMS curves are shown. Two curves show the results of modelling based on LO (MRSTL) and NLO (MRSTM) parton distribution functions. The latter leads to predictions closer to the data with a fixed value of the t slope, $b = 4.9\,\mathrm{GeV}^{-2}$. Similar conclusions are reached when the CTEQ6 parameterisations [158–160] are used (NLO CTEQ6 for $b = 4.9\,\mathrm{GeV}^{-2}$ is only shown). The difference between the MRST and CTEQ6 curves at LO and NLO reflects the relative size of the quark singlet and gluon distributions for each set. The comparison illustrates that within the framework of the forward input model for GPD, the DVCS cross section remains sensitive to the input PDF and to the calculation accuracy (LO or NLO). Moreover, all of the theory curves seem to have a too steep Q^2 dependence to describe all of the data points.

It was pointed out [6] that the b slope of the DVCS cross section should depend strongly on Q^2 at small x in the transition region from small to large Q^2. At $Q^2 \approx 2\,\mathrm{GeV}^2$, it is expected that the slope will be pretty close to $b \approx 8\,\mathrm{GeV}^{-2}$ for exclusive ρ vector-meson electroproduction [161]. At large Q^2, the b slope drops rather rapidly with increasing Q^2 reaching $b \approx 5\,\mathrm{GeV}^{-2}$ at $Q^2 \approx 10\,\mathrm{GeV}^2$ for the meson ρ [162].

The fourth curve in Fig. 77 shows predictions based on MRSTM, assuming the b slope Q^2-dependent. The best agreement between the data and the predictions is achieved using a parameterisation obtained by FMS from a fit to a preliminary version of the present data [152] for the range of $2 < Q^2 < 100\,\mathrm{GeV}^2$

$$b(Q^2) = b_0(1 - 0.15\ln(Q^2/2))\,\mathrm{GeV}^{-2}, \qquad (18)$$

with $b_0 = 8\,\mathrm{GeV}^{-2}$. This modification of the b slope gives a great improvement in agreement with the data and it also emphasises the need of a direct measurement of the t dependence of the DVCS cross section. It has to be stressed that b, which has never been measured for DVCS, is a source of the largest theoretical uncertainty in the DVCS predictions.

Colour-dipole predictions

The W and Q^2 dependencies of $\sigma^{\gamma^* p}$ have been compared to the expectations of the three calculations based on CDM (see Sect. 2.5.2): by Donnachie and Dosch (DD) [61], by Forshaw, Kerley and Shaw (FKS) [58,62,63] and by McDermott, Frankfurt, Guzey and Strikman (MFGS) [60,63]. All the models differ in a calculation of the dipole-proton cross section σ_d.

In the DD model, σ_d is modelled within the framework of the two $\mathbb{P}$ approach, where small dipoles interact predominantly with the hard $\mathbb{P}$ and large dipoles with the soft $\mathbb{P}$. The model has no energy dependence, i.e. σ_d is a function of R only. The free parameters of this model have been determined from $\bar{p}p$ and pp experiments and inclusive diffractive data at HERA. Thus, the DVCS prediction has no free parameters.

In the FKS model, the dipole cross section is assumed to depend solely on the properties of the dipole-proton system itself, independent of the virtuality of the incoming or outgoing photon. The idea was then to extract information on σ_d by assuming a parametric form of the dipole cross section to fit the structure function and diffractive data in the region $x \leq 0.001$ and $0 < Q^2 < 60\,\mathrm{GeV}^2$. This was implemented by assuming a Regge type energy dependence of σ_d separately for small ($R \to 0$) and large ($R \to 1\,\mathrm{fm}$) dipoles. This model has no free parameters for the DVCS prediction.

The MFGS model is directly based on the known behaviour of hard QCD processes at small x, driven by the gluon distributions. Using the phenomena of colour transparency, it directly relates σ_d for small dipoles to LO gluon distributions at large Q^2. For DVCS this model implements LO GPD using CTEQ4 gluon distributions as input to the LO skewed evolution. The parameters of the model are not adjusted to fit data, but nonetheless good accounts of the DIS and J/ψ photoproduction data were obtained. This model focuses on small dipoles only.

The comparisons of the three CDMs discussed above with the data are shown in Figs. 78 and 79 in W and Q^2, respectively. In all cases the exponential t dependence, $e^{-b|t|}$,

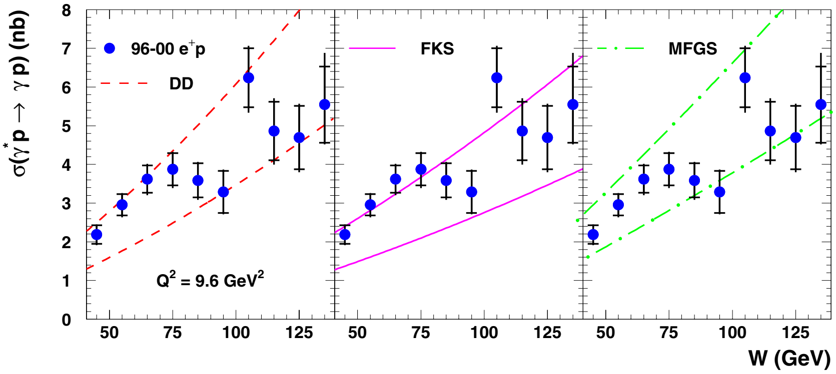

Fig. 78. The DVCS cross section, $\sigma(\gamma^* p \to \gamma p)$, as a function of W, as also shown in Fig. 73, for the e^+p data. The data are compared to the theoretical predictions of the DD, FKS and MFGS models of colour-dipole interactions. The curves correspond to fixed b values, $b = 4\,\mathrm{GeV}^{-2}$ (upper) and $b = 7\,\mathrm{GeV}^{-2}$ (lower)

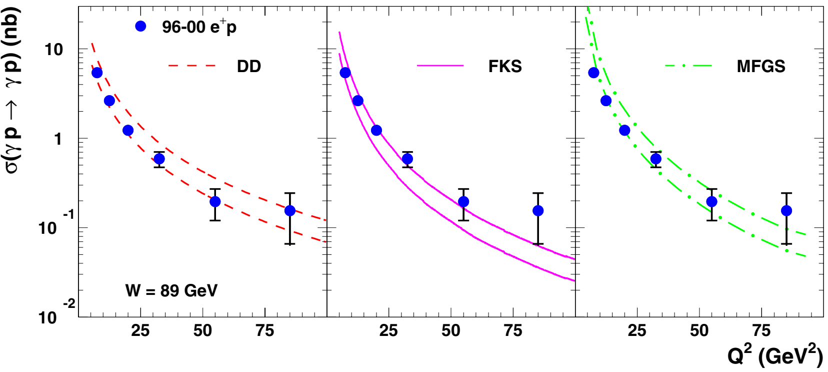

Fig. 79. The DVCS cross section, $\sigma(\gamma^* p \to \gamma p)$, as a function of Q^2, as also shown in Fig. 75, for the e^+p data. The data are compared to the theoretical predictions of the DD, FKS and MFGS models of colour-dipole interactions. The curves correspond to fixed b values, $b = 4\,\mathrm{GeV}^{-2}$ (upper) and $b = 7\,\mathrm{GeV}^{-2}$ (lower)

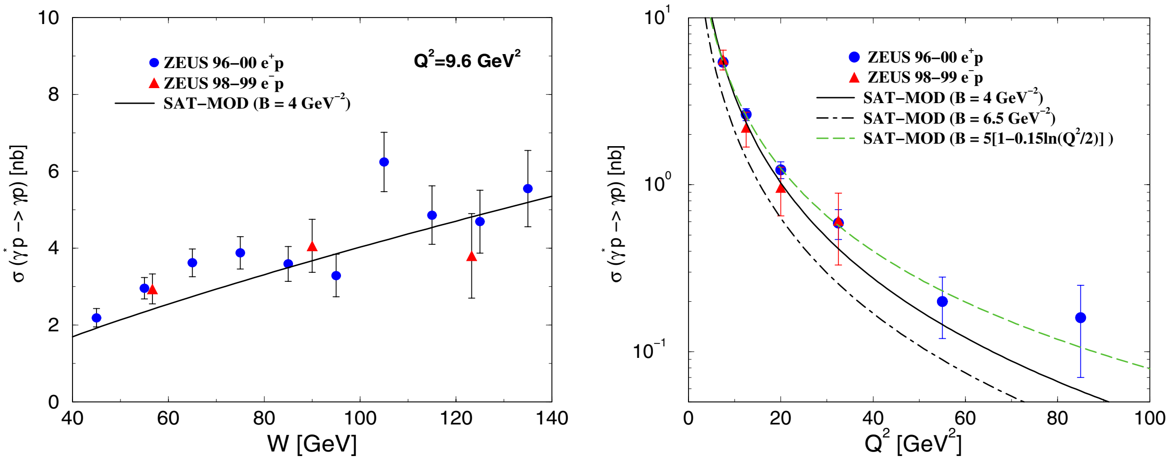

Fig. 80. The DVCS cross section, $\sigma(\gamma^* p \to \gamma p)$, as a function of W (left) and Q^2 (right). The curves are the result for the saturation model using $b = 4\,\mathrm{GeV}^{-2}$ (solid), $b = 6.5\,\mathrm{GeV}^{-2}$ (dot-dashed) or Q^2-dependent b slope value (dashed). Plots taken from [65]

was assumed. The model expectations are represented by curves corresponding to the fixed values of $b = 4\,\mathrm{GeV}^{-2}$ (upper) and $b = 7\,\mathrm{GeV}^{-2}$ (lower), chosen for illustration. All three predictions give a reasonable description of the data preferring low (FKS) or large (DD, MFGS) b slope values. The consistency of all the predictions with the data is very promising for the dipole models. It should be emphasised that the uncertainty in b implies an associated uncertainty in the normalisation of the cross sections, which can be also Q^2-dependent.

The recent approach by Favart and Machado (FM) [64, 65] parametrises the dipole cross section via the saturation model [56,57], which interpolates between small and large dipole configurations, providing colour transparency behaviour $\sigma_d \sim R^2$ for small dipoles and constant behaviour $\sigma_d \sim \sigma_0$ for large ones. The calculation was performed using the three- and four-flavour analyses. The inclusion of charm gives a slightly lower normalisation for the total DVCS cross section than using only the light quarks if one considers the same b value. Free parameters of this model have been obtained from a fit to the HERA data [56].

In Fig. 80 the result of the saturation model adopted by FM to DVCS [64,65] compared to the data as a function of W is shown. The four-flavour analysis shows good agreement for a fixed value of the slope, $b = 4\,\mathrm{GeV}^{-2}$. In the same figure, the saturation model for the Q^2 behaviour is depicted. In order to illustrate the sensitivity to the slope value, the model predictions for both values $b = 4\,\mathrm{GeV}^{-2}$ and $b = 6.5\,\mathrm{GeV}^{-2}$ are shown. For $Q^2 > 40\,\mathrm{GeV}^2$, the model seems to underestimate the data. The reason can be two-fold:

- the b slope decreases with Q^2,
- some additional effects take place at higher Q^2.

In order to investigate the Q^2-dependent b, the slope of the form (18) has been proposed. This dependence describes $\sigma^{\gamma^* p}$ up to the highest measured values of Q^2 and gives a good normalisation for $b_0 = 5\,\mathrm{GeV}^{-2}$ (see Fig. 80).

The QCD evolution was implemented recently by Bartels, Golec-Biernat and Kowalski [163,164] to the original saturation model and will be referred to as BGBK. In this approach the dipole cross section depends on the gluon distribution as

$$\sigma_d = \sigma_0 \left[1 - \exp\left(-\frac{\pi^2 R^2 \alpha_s(\mu) \tilde{x} g(\tilde{x}, \mu^2)}{3\sigma_0}\right)\right],$$

where $\tilde{x} = x(1 + 4m_q^2/Q^2)$. The parameters of the model were determined from a fit to DIS data with the LO DGLAP evolution [165–167]. The DGLAP evolution improves description of the data for large-Q^2 regime.

The BGBK dipole cross section adopted by FM to DVCS as a function of Q^2 using $b = 4\,\mathrm{GeV}^{-2}$ is shown in Fig. 81. There is an effect in the overall normalisation which is higher than for the saturation model and a slower decrease at large Q^2 in contrast with the model without the QCD evolution. The BGBK model reproduces well the measurement for all Q^2 values. This suggests that the DGLAP evolution starts playing an important rôle for large Q^2.

In order to investigate the skewedness effect for DVCS, the FM approach implements approximation of the ratio of off-forward to forward PDF following [168] as

$$R_{q,g}(Q^2) = \frac{2^{2\lambda+3}}{\sqrt{\pi}} \frac{\Gamma(\lambda + 5/2)}{\Gamma(\lambda + 3 + p)}, \tag{19}$$

where $p = 0$ for quarks (R_q) and $p = 1$ for gluons (R_g). The quantity λ is the exponent of the $x^{-\lambda}$ behaviour of the input forward PDF and Γ denotes the gamma function. The skewedness effect defined by (19) is much larger for singlet quarks than gluons. For DVCS a two gluon exchange is assumed and the skewedness effect is implemented by multiplying the total cross section by the factor R_g^2.

The results of the skewedness correction for the saturation model and the BGBK predictions in Q^2 are shown in Fig. 81. The main effect is an increase of the overall normalisation of $\sigma^{\gamma * p}$ by about 40%, while the DVCS cross section is only slightly modified for large Q^2 values.

If s-channel helicity is conserved in DVCS [169], the virtual photon must be transversely polarised due to the real photon in the final state. As the wave function of the

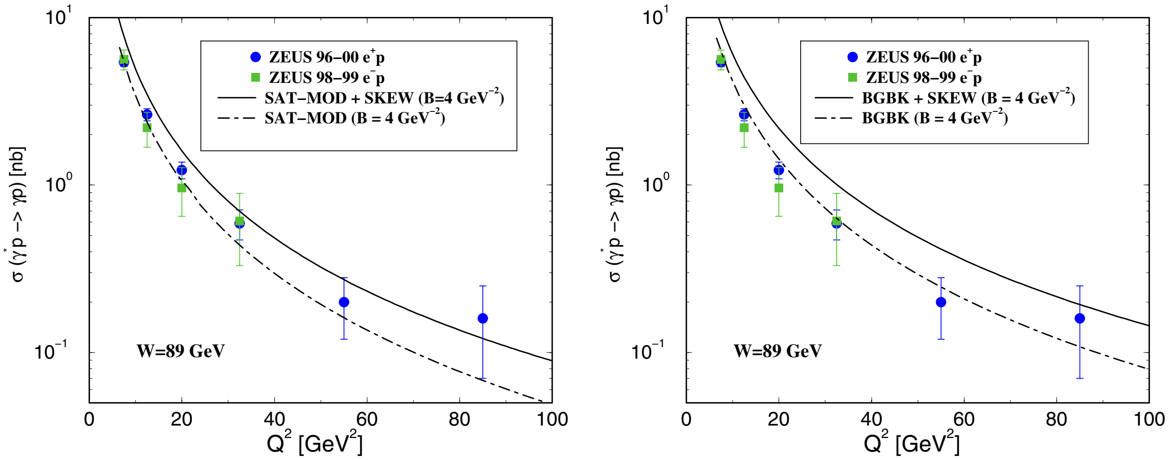

Fig. 81. The DVCS cross section, $\sigma(\gamma^* p \to \gamma p)$, as a function of Q^2 compared to the saturation model (left) and BGBK model (right). The curves are the result for models without (dot-dashed) and with (solid) skewedness effect using the fixed slope $b = 4\,\mathrm{GeV}^{-2}$. Plots taken from [65]

transversely polarised photon can select large dipole sizes, whose interactions are predominantly soft, DVCS constitutes a good probe of the transition between soft and hard regimes of DIS. In particular, the transition can be tested by the W dependence of the cross section. Such a feature provides a particularly relevant test of different realisations of the CDM. Nonetheless, the present results for DVCS show how important is a measurement of the b slope in order to discriminate between the available theoretical approaches, with an amount of the data used to this analysis [65].

10 Summary and conclusions

In this thesis the deeply virtual Compton scattering (DVCS) has been studied in the kinematic range $5 < Q^2 < 100\,\mathrm{GeV}^2$ and $40 < W < 140\,\mathrm{GeV}$. The measurement was based on a data sample corresponding to an integrated luminosity of $95\,\mathrm{pb}^{-1}$ ($17\,\mathrm{pb}^{-1}$) for e^+p (e^-p) interactions, which was collected with the ZEUS detector during the 1996–2000 data taking period, when HERA was operating with 27.5 GeV electrons (98–99) or positrons (96–97, 99–00) and 820 GeV (96–97) or 920 GeV (98–00) protons.

The analysis was based on a ten-fold increase of statistics over a previous HERA 1997 e^+p results [14, 15], and it significantly extended the Q^2 range probed. Moreover, this thesis also presents the first measurement of the e^-p cross sections.

The DVCS signal has been obtained by selection of events with an electron and a photon in the kinematic region, where DVCS has been foreseen to dominate. A large excess of events over the Bethe-Heitler events, which have the same signature as the DVCS process in the detector, has been observed. By means of the Monte Carlo program GenDVCS, newly developed for this analysis, the $\gamma^* p \to \gamma p$ cross sections have been determined.

No significant difference between the e^+p and e^-p interactions was observed. The Q^2 dependence of the DVCS cross section follows approximately a Q^{-3} behaviour. The precision of the data allowed an accurate determination of the W distribution for the first time. A fit of the form $\sigma^{\gamma^* p} \propto W^\delta$ for the e^+p data yields $\delta = 0.75 \pm 0.15(\text{stat.})\,^{+0.08}_{-0.06}(\text{syst.})$, which is comparable to the result determined for J/ψ electroproduction [144]. Thus, the cross section rises steeply with W, indicative of a hard underlying process, where the rise reflects the increase of parton distributions with decreasing x. High statistics of the e^+p data enabled also the measurement of the W dependence of $\sigma^{\gamma^* p}$ in several bins of Q^2 for the first time. The results are compatible with no dependence of δ on Q^2 although also with the increase with Q^2 observed in exclusive production of light vector mesons [142, 149]. The main results of this thesis have been published [153].

The measured cross sections have been compared to calculations based on generalised parton distributions (GPD) and on various realisations of the colour-dipole model. Generally, good agreement with the data is observed.

This measurement demonstrates the potential of DVCS data to constrain the structure of the proton and quark-gluon dynamics at low x. It is possible that more precise data on DVCS may eventually allow to discriminate between various input scenarios using either next-to-leading order QCD or the semi-classical approaches based on various realisations of the colour-dipole model. This can be achieved thanks to increase of integrated luminosity after the HERA upgrade. In addition, a measurement of the azimuthal-angle and beam-charge asymmetries in an unpolarised ep scattering would provide access to the interference term as well as to the real part of the QCD amplitude. An analogous measurement of the beam-spin asymmetry in a polarised ep scattering would allow to extract the imaginary part of the DVCS amplitude. Subsequently an information on the GPD could be obtained. Nevertheless, an explicit measurement of the t dependence for DVCS is desirable in order to overcome the uncertainty associated with the b slope, which reflects in the overall normalisation of $\sigma^{\gamma^* p}$ and which has never been measured for DVCS.

This can be achieved by use of the Leading Proton Spectrometer (LPS), which allows a precise measurement of the proton final-state and thus offers a possibility to measure the b slope for DVCS for the first time. The first attempt of measuring of the t dependence by means of the LPS was already made within this thesis, but very small statistics due to low efficiency of the LPS did not allow for reasonable results. The extension of the kinematic range of this analysis to $2 \lesssim Q^2 \lesssim 100\,\mathrm{GeV}^2$ and $30 \lesssim W \lesssim 250\,\mathrm{GeV}$ in conjunction with use of the LPS seems to be also very promising [170].

Acknowledgements. I am thankful to Prof. Danuta Kisielewska, who gave me the opportunity to work on my PhD within the ZEUS Collaboration in DESY. I am also grateful to her for the encouragement and guidance during my studies. To my supervisor, Prof. Leszek Turczynowicz-Suszycki, goes my gratitude for not only providing me with advice and support throughout my PhD but also giving me the freedom to pursue the analysis of my choice. I am also grateful to him for patient correcting the drafts of this thesis.

I am greatly indebted to the DESY Directorate for supporting my stay in Hamburg. Furthermore, I feel a deep sense of gratitude to Prof. Andrzej Eskreys for his support during my work in the LUMI group. A support of Polish State Committee for Scientific Research (KBN), grant no. 2 P03B122 25, is also gratefully acknowledged.

I would like to express my gratitude to Leszek Adamczyk. His experience has allowed me to familiarise with the issue of data analysis.

I am especially grateful to Pat Saull for showing me the beauty of the DVCS analysis and for the invaluable help with it. I really appreciate everything he has done for me.

I am deeply indebted to Halina Abramowicz for interesting discussions and useful advices as well as for helping me to write the DVCS paper.

I owe a debt of gratitude to the members of the ZEUS working group on Diffractive and Vector Mesons Physics and especially to its coordinators, Yuji Yamazaki, Giuseppe Iacobucci, Kerstin Borras and Alessia Bruni, who have stimulated the progress of this analysis.

Moreover, I would like to express my thanks to my colleagues and friends from Kraków, in no particular order, Ela Nowak, Dorota Szuba, Agnieszka Kowal, Janusz Szuba, Kasia Klimek, Marek Kowal, Agnieszka Obłąkowska-Mucha, Tomasz Szumlak, Mariusz Przybycień. Their friendship and kindness have been very important to me for the recent years. Many of them have also contributed to this analysis. Thank you!

Finally, I would like to thank my husband, Tomasz, for having an endless amount of love, patience and understanding. Without him I would have never finished.

References

1. E. Wieczorek, V.A. Matveev, D. Robaschik, Theor. Math. Phys. **19**, 315 (1974)
2. J. Bartels, M. Loewe, Z. Phys. C **12**, 263 (1982)
3. X. Ji, Phys. Rev. D **55**, 7114 (1997)
4. A.V. Radyushkin, Phys. Rev. D **58**, 114008 (1998)
5. J.C. Collins, A. Freund, Phys. Rev. D **59**, 74009 (1999)
6. L.L. Frankfurt, A. Freund, M. Strikman, Phys. Rev. D **58**, 114001 (1998); erratum Phys. Rev. D **59**119901 (1999)
7. X. Ji, Phys. Rev. Lett. **78**, 610 (1997)
8. K. Golec-Biernat, A. Martin, Phys. Rev. D **59**, 014029 (1999)
9. A. Belitsky, A. Freund, D. Muller, Nucl. Phys. B **574**, 347 (2000)
10. L. Frankfurt, A. Freund, M. Strikman, Phys. Lett. B **460**, 417 (1999)
11. A.V. Belitsky, D. Muller, A. Kirchner, Nucl. Phys. B **629**, 323 (2002)
12. A. Freund, M. McDermott, Phys. Rev. D **65**, 091901 (2002)
13. P.R.B. Saull, in: Proceedings of the International Europhysics Conference on High-Energy Physics (EPS-HEP 99), Tampere, Finland, 15–21 July 1999 (hep-ex/0003030), pp. 420–422
14. H1 Coll., C. Adloff et al., Phys. Lett. B **517**, 47 (2001)
15. R. Stamen, Measurement of Deeply Virtual Compton Scattering at HERA, Ph.D. Thesis, FB Physik, Univ. Dortmund and Université Libre de Bruxelles, Report DESY-THESIS-2001-057 (2001)
16. HERMES Coll., A. Airapetian et al., Phys. Rev. Lett. **87**, 182001 (2001)
17. CLAS Coll., S. Stepanyan et al., Phys. Rev. Lett. **87**, 182002 (2001)
18. J.H. Ely, Measurement of the Single Spin Azimuthal Asymmetry in the Predominantly Exclusive Electroproduction of Photons from the Proton, Ph.D. Thesis, University of Colorado (2002)
19. Available on http://www-zeus.desy.de/ZEUS_ONLY/analysis/orange/index.html
20. L.N. Hand, Phys. Rev. **129**, 1834 (1963)
21. E.D. Bloom et al., Phys. Rev. Lett. **23**, 930 (1969)
22. M. Breidenbach et al., Phys. Rev. Lett. **23**, 935 (1969)
23. H1 Coll., S. Aid et al., Nucl. Phys. B **470**, 3 (1996)
24. ZEUS Coll., M. Derrick et al., Z. Phys. C **72**, 399 (1996)
25. ZEUS Coll., available on http://www-zeus.desy.de/public_results/
26. J.D. Bjorken, Phys. Rev. **163**, 1767 (1967)
27. R.P. Feynman, Phys. Rev. Lett. **23**, 1415 (1969)
28. M. Gell-Mann, Phys. Lett. **8**, 214 (1964)
29. G. Zweig, CERN-TH-412
30. T. Eichten et al., Phys. Lett. B **46**, 274 (1973)
31. J.C. Collins, D.E. Soper, G. Sterman, Nucl. Phys. B **261**, 104 (1985)
32. G. Alberi, G. Goggi, Phys. Rep. **74**, 1 (1981)
33. K. Goulianos, Phys. Rep. **101**, 169 (1983)
34. ZEUS Coll., M. Derrick et al., Phys. Lett. B **315**, 481 (1993)
35. P.D.B. Collins, An Introduction to Regge Theory and High Energy Physics (Cambridge University Press, 1977)
36. G.F. Chew, S.C. Frautschi, Phys. Rev. Lett. **8**, 41 (1962)
37. V.N. Gribov, Sov. Phys. JETP **14**, 478 (1962)
38. I.Y. Pomeranchuk, Sov. Phys. JETP **7**, 499 (1985)
39. H1 Coll., C. Adloff et al., Z. Phys. C **74**, 221 (1997)
40. H1 Coll., T. Ahmed et al., Nucl. Phys. B **429**, 477 (1994)
41. A. Donnachie, P.V. Landshoff, Phys. Lett. B **296**, 227 (1992)
42. H1 Coll., Elastic Electroproduction of ρ Mesons at High Q^2 at HERA, Abstract 092, in: Proceedings of the International Europhysics Conference on High Energy Physics, EPS03, Aachen, Germany, 17–23 July, 2003

43. A.V. Radyushkin, Phys. Lett. B **380**, 417 (1996)
44. A.V. Radyushkin, Phys. Rev. D **56**, 5524 (1997)
45. M. Guidal, Nucl. Phys. A **699**, 200 (2002)
46. M. Diehl, Phys. Rept. **388**, 41 (2003)
47. A. Freund, Phys. Lett. B **472**, 412 (2000)
48. M. Diehl et al., Phys. Lett. B **411**, 193 (1997)
49. A. Freund, M. McDermott, M. Strikman, Phys. Rev. D **67**, 036001 (2003)
50. A. Freund, M. McDermott, Eur. Phys. J. C **23**, 651 (2002)
51. A. Freund, M. McDermott, Phys. Rev. D **65**, 091901 (2002)
52. N.N. Nikolaev, B.G. Zakharov, Z. Phys. C **49**, 607 (1991)
53. N.N. Nikolaev, B.G. Zakharov, Z. Phys. C **53**, 331 (1992)
54. A.H. Mueller, Nucl. Phys. B **415**, 373 (1994)
55. A.H. Mueller, B. Patel, Nucl. Phys. B **425**, 471 (1994)
56. K. Golec-Biernat, M. Wüsthoff, Phys. Rev. D **59**, 014017 (1999)
57. K. Golec-Biernat, M. Wüsthoff, Phys. Rev. D **60**, 114023 (1999)
58. J.R. Forshaw, G. Kerley, G. Shaw, Phys. Rev. D **60**, 074012 (1999)
59. E. Gotsman, E. Levin, U. Maor, Phys. Lett. B **425**, 369 (1998)
60. M. McDermott et al., Eur. Phys. J. C **16**, 641 (2000)
61. A. Donnachie, H.G. Dosch, Phys. Lett. B **502**, 74 (2001)
62. J.R. Forshaw, G. Kerley, G. Shaw, Nucl. Phys. A **675**, 80c (2000)
63. M. McDermott, R. Sandapen, G. Shaw, Eur. Phys. J. C **22**, 655 (2002)
64. L. Favart, M. Machado, Eur. Phys. J. C **29**, 365 (2003)
65. L. Favart, M. Machado, QCD evolution and skewedness effects in color dipole description of DVCS, Preprint hep-ph/0402018 (2004)
66. HERA: A Proposal for a Large Electron Proton Colliding Beam Facility at DESY, DESY-HERA-81/10, Hamburg (1981)
67. ZEUS Coll., U. Holm (ed.), The ZEUS Detector, Status Report (unpublished), DESY (1993), available on http://www-zeus.desy.de/bluebook/bluebook.html
68. N. Harnew et al., Nucl. Instrum. Methods A **279**, 290 (1989)
69. B. Foster et al., Nucl. Phys. Proc. Suppl. B **32**, 181 (1993)
70. B. Foster et al., Nucl. Instrum. Methods A **338**, 254 (1994)
71. A. Bamberger et al., Nucl. Instrum. Methods A **401**, 63 (1997)
72. M. Derrick et al., Nucl. Instrum. Methods A **309**, 77 (1991)
73. A. Andresen et al., Nucl. Instrum. Methods A **309**, 101 (1991)
74. A. Caldwell et al., Nucl. Instrum. Methods A **321**, 356 (1992)
75. A. Bernstein et al., Nucl. Instrum. Methods A **336**, 23 (1993)
76. ZEUS Coll., FPC group, A. Bamberger et al., Nucl. Instrum. Methods A **450**, 235 (2000)
77. A. Bamberger et al., Nucl. Instrum. Methods A **382**, 419 (1996)
78. S. Magill, S. Chekanov, in: Proceedings of the IX International Conference on Calorimetry in High Energy Physics, Annecy, France (2000), edited by B. Aubert et al., p. 625
79. A. Dwurazny et al., Nucl. Instrum. Methods A **277**, 176 (1989)
80. M. Bobrowski et al., Nucl. Instrum. Methods A **323**, 309 (1992)
81. B. Bednarek et al., Nucl. Instrum. Methods A **348**, 228 (1994)
82. ZEUS Coll., J. Breitweg et al., Z. Phys. C **75**, 421 (1997)
83. ZEUS Coll., M. Derrick et al., Z. Phys. C **73**, 253 (1997)
84. ZEUS Coll., FNC group, S. Bhadra et al., Nucl. Instrum. Methods A **394**, 121 (1997)
85. B. Surrow, Measurement of the Proton Structure Function F_2 at Low Q^2 and Very Low x with the ZEUS Beam Pipe Calorimeter at HERA, Ph.D. Thesis, Univ. of Hamburg, Report DESY-THESIS-1998-004 (1998)
86. J. Andruszków et al., Preprint DESY-92-066, DESY (1992)
87. ZEUS Coll., M. Derrick et al., Z. Phys. C **63**, 391 (1994)
88. J. Andruszków et al., Acta Phys. Pol. B **32**, 2025 (2001)
89. R. Hall-Wilton et al., The CTD Tracking Resolution (unpublished), ZEUS-99-024, internal ZEUS-note (1999)
90. E. Bernardi et al., Nucl. Instrum. Methods A **262**, 229 (1987)
91. F. Goebel, Measurement of the Diffractive Contribution to the DIS Cross Section Using the ZEUS Forward Plug Calorimeter, Ph.D. thesis, Univ. of Hamburg, Hamburg, Germany, Report DESY-THESIS-2002-002 (2001)
92. H. Bethe, W. Heitler, Proc. Roy. Soc. Lond. A **146**, 83 (1934)
93. M. van der Horst, Nucl. Phys., 149 (1990)
94. K. Piotrzkowski, M. Zachara, Determination of the ZEUS Luminosity in 1994 (unpublished), ZEUS-95-138 (1995)
95. E. Tscheslog, ZEUS Reconstruction Program, Organisation and Control, ZEUS Note 91-037 (1991)
96. G.F. Hartner et al., VCTRAK (3.07/04): Off-line Output Information, ZEUS Note 97-064 (1997)
97. P. de Jong, Status of the Uranium Calorimeter Reconstruction Software, ZEUS Note 92-019 (1992)
98. M. de Kamps, Changes, extensions of the calorimeter reconstruction programme, ZEUS Note 94-014 (1994)
99. N. Tuning, Proton Structure Functions at HERA, Ph.D. Thesis, Amsterdam University (2001)
100. J. Ng, W. Verkerke, An Overview of SRTD Analysis, ZEUS Note 95-037 (1995)
101. J.I. Fleck, K. Ohrenberg, Electron Identification in the HES and a new way to determine the efficiency of electron finders, ZEUS Note 95-009 (1995)
102. A. Meyer, Electron Energy Correction with the Presampler, Part I, ZEUS Note 99-066 (1999)
103. A. Meyer, Electron Energy Correction with the Presampler, Part II, ZEUS Note 00-036 (2000)
104. A. Caldwell, W. Liu, B. Straub, BCAL Electron Studies Part II: Energy Scale Calibration, ZEUS Note 98-018 (1998)
105. R. Sinkus, Measurement of the Proton Structure Function F_2 from the 1994 HERA Data using a Neural Network for the Identification of the Scattered Lepton, Thesis, Hamburg University (1994)
106. H. Abramowicz, A. Caldwell, R. Sinkus, Nucl. Instrum. Methods A **365**, 508 (1995)
107. R. Sinkus, T. Voss, Nucl. Instrum. Methods A **391**, 360 (1997)
108. T. Doeker, A. Frey, M. Nakao, Electron Position Reconstruction – Update of the ELECPO routines, ZEUS Note 94-123 (1994)

109. Ch. Amelung, Electron Position Reconstruction in ZEUS: Further Update of the ELECPO Package (Based on 1995 Data), ZEUS Note 96-093 (1996)
110. Ch. Amelung, Electron Position Reconstruction in ZEUS: Another Update of the ELECPO Package (Based on 1995/96 Data), ZEUS Note 97-053 (1997)
111. C. Catterall, F. Pelucchi, Comparison of CTD and Calorimeter Measurement of the DIS Positron Angle in High Q^2 Events, ZEUS Note 97-056 (1997)
112. S. Bentvelsen, J. Engelen, P. Kooijman, in: Proceedings of the Workshop on Physics at HERA, Vol. 1, edited by W. Buchmüller, G. Ingelman, Hamburg, Germany, DESY (1992), p. 23
113. K.C. Höger, in: Proceedings of the Workshop on Physics at HERA, Vol. 1, edited by W. Buchmüller, G. Ingelman, Hamburg, Germany, DESY (1992), p. 43
114. F. Jacquet, A. Blondel, in: Proceedings of the Study for an *ep* Facility for Europe, Hamburg, Germany (1979), edited by U. Amaldi, p. 391; also in preprint DESY 79/48
115. U. Bassler, G. Bernardi, Nucl. Instrum. Methods A **361**, 197 (1995)
116. TLT Group, available on http://www-zeus.desy.de/components/trigger/ZEUS_ONLY/2001/ tlt
117. A. Savin, Study of Calorimeter Noise in the 1996 Data, ZEUS Note 98-007 (1998)
118. T. Haas, Generation Monte Carlo events with MOZART, ZEUS Note 92-021 (1992)
119. R. Brun et al., GEANT3, Technical Report CERN-DD/EE/84-1,CERN (1987)
120. Els de Wolf (editor) et al., ZGANA, ZEUS trigger simulation library
121. P.R.B. Saull, A Monte Carlo Generator for Deeply Virtual Compton Scattering at HERA, 1999, available on http://www-zeus.desy.de/physics/diff/pub/ MC
122. H. Abramowicz, A. Levy, Preprint DESY-97-251 (hep-ph/9712415), DESY (1997)
123. H. Spiesberger, An Event Generator for *ep* Interactions at HERA Including Radiative Processes (Version 4.6), 1996, available on http://www.desy.de/~hspiesb/heracles.html
124. T. Abe, Comput. Phys. Commun. **136**, 126 (2001)
125. F.W. Brasse et al., Nucl. Phys. B **110**, 413 (1976)
126. H. Burkhardt, B. Pietrzyk, Phys. Lett. B **356**, 398 (1995)
127. T. Sjöstrand, Comput. Phys. Commun. **82**, 74 (1994)
128. A. Mücke et al., Comput. Phys. Commun. **124**, 290 (2000)
129. T. Carli et al., in: Proceedings of the Workshop on Physics at HERA, Vol. 3, Hamburg, Germany, DESY (1992), edited by W. Buchmüller, G. Ingelman, p. 1468
130. K. Muchorowski, Ph.D. Thesis, Warsaw University, 1998 (unpublished)
131. H. Jung, Comput. Phys. Commun. **86**, 147 (1995)
132. H. Spiesberger, HERACLES, DJANGOH: Event Generation for *ep* Interactions at HERA Including Radiative Processes, 1998, available on http://www.desy.de/~hspiesb/djangoh.html
133. L. Lönnblad, Comput. Phys. Commun. **71**, 15 (1992)
134. B. Anderson et al., Phys. Rev. D **97**, 31 (1993)
135. T. Sjöstrand, Comput. Phys. Commun. **82**, 74 (1994)
136. G. Ingelman et al., Comput. Phys. Commun. **101**, 108 (1997)
137. M. Wing, Summary from energy-scale WG (unpublished), talk given during the ZEUS Collaboration Meeting (2002)
138. H1 Coll., Investigation of Pomeron- and Odderon Induced Photoproduction of Mesons Decaying to Pure Multiphoton Final States at HERA, contributed paper (abstract 997) to ICHEP2002, Amsterdam (2002)
139. S.I. Alekhin et al., CERN-HERA 87-01 (1987)
140. R.L. Anderson et al., Phys. Rev. D **7**, 1937 (1971)
141. A. Levy, Estimate of some two-body reaction cross sections as background to the DVCS process (unpublished), ZEUS-99-039 (1999)
142. ZEUS Coll., J. Breitweg et al., Eur. Phys. J. C **6**, 603 (1999)
143. ZEUS Coll., J. Breitweg et al., Eur. Phys. J. C **14**, 213 (2000)
144. ZEUS Coll., S. Chekanov et al., Eur. Phys. J. C **24**, 345 (2002)
145. ZEUS Coll., M. Derrick et al., Phys. Lett. B **377**, 259 (1996)
146. ZEUS Coll., M. Derrick et al., Phys. Lett. B **380**, 220 (1996)
147. ZEUS Coll., M. Derrick et al., Z. Phys. C **73**, 73 (1996)
148. A. Quadt, Measurement and QCD Analysis of the Proton Structure Function F_2 from the 1994 HERA Data Using the ZEUS Detector, Ph.D. Thesis, University of Oxford, Report RAL-TH-97-004 (1997)
149. H1 Coll., C. Adloff et al., Eur. Phys. J. C **13**, 371 (2000)
150. H1 Coll., C. Adloff et al., Phys. Lett. B **483**, 360 (2000)
151. L. Favart, Studies of DVCS and photoproduction of photons at high t with the H1 detector (2003)
152. ZEUS Coll., Measurement of the deeply virtual Compton scattering cross section at HERA, Abstract 825, in: Proceedings of the XXXIst International Conference on High Energy Physics, Amsterdam, The Netherlands, 24–31 July, 2002
153. S. Chekanov et al., Phys. Lett. B **573**, 46 (2003)
154. L.L. Frankfurt, M.I. Strikman, Phys. Rep. **160**, 235 (1988)
155. L. Frankfurt, M. Strikman, Nucl. Phys. B **316**, 340 (1989)
156. R.S. Thorne et al., in: Proceedings of the 9th International Workshop on Deep Inelastic Scattering (DIS 2001), Bologna, Italy, 27 Apr–1 May 2001, edited by G. Bruni, G. Iacobucci, R. Nania, hep-ph/0106075, pp. 405–408
157. A.D. Martin et al., Nucl. Phys. Proc. Suppl. **79**, 105 (1999)
158. H.L. Lai et al., Phys. Rev. D **51**, 4763 (1995)
159. J. Botts et al., Phys. Lett. B **304**, 159 (1995)
160. CTEQ Coll., H.L. Lai et al., Eur. Phys. J. C **12**, 375 (2000)
161. ZEUS Coll., Exclusive and proton-dissociative electroproduction of ρ^0 mesons at HERA, Abstract 818, in: Proceedings of the XXXIst International Conference on High Energy Physics, Amsterdam, The Netherlands, 24–31 July, 2002
162. H1 Coll., Elastic electroproduction of ρ mesons at high Q^2 at HERA, Abstract 989, in: Proceedings of the XXXIst International Conference on High Energy Physics, Amsterdam, The Netherlands, 24–31 July, 2002
163. J. Bartels K. Golec-Biernat, H. Kowalski, Phys. Rev. D **66**, 014001 (2002)
164. J. Bartels, K. Golec-Biernat, H. Kowalski, Acta Phys. Polon. B **33**, 2853 (2002)
165. Yu.L. Dokshitzer, Sov. Phys. JETP **46**, 641 (1977)
166. V.N. Gribov, L.N. Lipatov, Sov. J. Nucl. Phys. **15**, 438 (1972)
167. G. Altarelli, G. Parisi, Nucl. Phys. B **126**, 298 (1977)
168. A.G. Shuvaev et al., PR D **60**, 014015 (1999)
169. F.J. Gilman et al., Phys. Lett. B **31**, 387 (1970)
170. S. Fazio, private communication